Computational Modelling of Fluid Load Support in Articular Cartilage

Shuqiang An

Submitted in accordance with the requirements for the degree of

Doctor of Philosophy

The University of Leeds

School of Mechanical Engineering

September 2013

The candidate confirms that the work submitted is his own, except where work which has formed part of jointly-authored publications has been included. The contribution of the candidate and the other authors to this work has been explicitly indicated below. The candidate confirms that appropriate credit has been given within the thesis where reference has been made to the work of others.

Jointly Authored Publications

1) An, Shuqiang; Jones Alison; Damion Robin; Fisher John and Jin Zhongmin. Realistic Fibril Distribution Basing on DT-MRI Data Enhances Pressurization of Interstitial Fluid in 2D Fibril-Reinforced Cartilage Model. Podium presentation. Paper No. 0396, Session 66. Annual Meeting of the Orthopaedic Research Society, 2013, San Antonio, Texas.

This was based on Chapter 2, Chapter 3 and Chapter 4, and was carried out by the author of this thesis in its entirety.

Acknowledgements

First and foremost, I would like to thank my supervisors, Professor John Fisher, Professor Zhongmin Jin and Dr. Alison Jones. Professor Fisher, my primary supervisor in the latest two years, has been overviewed my research project and provided me the most constructive and valuable advices during my research study. Prof. Jin was my primary supervisor in the first two years of study and much more than that, a great mentor and a warm-hearted friend. Jin contributed excellent ideas to this work, from the determination of the research subjects to the development of the models, from the presentation of the results to the final correction of this thesis. I am also very grateful to Dr. Jones for the detailed techniques and valuable discussion.

This study would not have been possible without the support of Dr. Robin Damion, school of Physics, who provided the experimental data implemented to the models in this thesis. I would also like to thank Graham, Ted and Margret for their computational support.

It is a great pleasure to work in iMBE, where people help each other. In this group, I received great help from the senior colleagues, Dr. Feng Liu, Dr. Qingen Meng, Dr. Mohd Juzaila Abd Latif, Dr. Sainath and Dr. Adam in whatever way possible, especially when I began my PhD.

Finally, I would like to address my thanks to my family. My wife, Jing, companies and takes care of me all the way throughout the life and study in

the UK. Also, great appreciation would like to be given to my daughter, Ran, who shared all of her joys and tears with me in these years.

This work was funded by the Engineering and Physical Sciences Research Council.

List of Abbreviations

BW – Body Weight

CAX4P – Four-node bilinear displacement and pore pressure

C3D20 – Twenty-node linear brick

C3D20RP – Twenty-node quadratic brick and pore pressure, reduced integration

DT-MRI – Diffusion Tensor Magnetic Resonance Imaging

FE – Finite Element

Abstract

Natural articular cartilage is known to be an excellent bearing material with very low friction coefficient and wear rate. Theoretical and experimental studies have demonstrated that the interstitial fluid of cartilage is pressurized considerably under loading to support the applied load, leading to the low friction coefficient. In this process, collagen fibrils play a vital role to resist the lateral expansion of cartilage and enhance the pressurization. The proportion of the total load supported by fluid pressurization in cartilage, called the fluid load support, is therefore an important parameter in biotribology and determined as the main aspect of this thesis.

Fibril-reinforced cartilage models were set up to account for the high pressurization of interstitial fluid. However, the orientation of collagen fibrils were idealized or simplified; and the models implementing realistic fibril orientation derived from DT-MRI data did not include viscous effects in both the solid matrix and the fibril.

This study overcome the limitation of previous models and the major finding were:

- The peak value of fluid load support in both 2D and 3D fibril-reinforced models implementing DT-MRI data was increased to greater than 90% from around 60% in the isotropic poroelastic model, due to the reinforcement by collagen fibril.

- The implementation of the realistic fibril orientation in the 3D fibril-reinforced model increased the value of peak pore pressure (by 15%) compared to the uniformly reinforced model while the peak contact pressure was 4.3% lower, making the peak value of fluid load support increase from 80.4% to 96.7%.
- The rationality to define the principal eigenvector as orientation of the corresponding primary collagen fibril in the fibril-reinforced models was verified by the related results.
- The feasibility and reliability of the methodologies to implement DT-MRI data to the fibril-reinforced models were both confirmed in the modelling process.

Table of Contents

List of Tables

List of Figures

Preface

In Loving Memory of My Mother

Chapter 1 Introduction and Literature Review

1.1 Introduction

This chapter reviews the literature relevant to the biomechanics and computational modeling of articular cartilage in the synovial joints. The material properties of articular cartilage are key factors in determining the lubrication of the joints. Therefore, the related literature on cartilage composition and structure including the biphasic lubrication is introduced first, after a brief review on the biomechanics of the two main synovial joints - knee and hip. The literature on the computational modelling of cartilage is reviewed in detail, particularly the fibril reinforced finite element models. As the collagen fibril orientations used in the models of this thesis were derived from the Diffusion Tensor Magnetic Resonance Imaging (DT-MRI) experiments, the related methodologies are also introduced as the background.

The review begins with a brief introduction to the biomechanics of knee and hip. The structure of these two largest synovial joints in the human body are introduced, followed a summary of the motion and loading of the joints.

The second part focuses on the articular cartilage. The detailed composition and structure of cartilage are reviewed. Then the concepts and viewpoints of the theory of biphasic lubrication within synovial joints are introduced.

The following section examines the literature relating to the computational modelling of cartilage. The developments of computational modelling techniques are discussed. The current methods to set up the fibril reinforced finite element models are categorized and reviewed individually.

In order to give a better understanding on the background of the thesis, the final section presents a review on the diffusion tensor MRI.

At the end of this chapter, the rationale and objectives of the project studied in this thesis are presented.

1.2 Synovial Joints and Biomechanics

The joints of the human body can be classified into three groups: fibrous, cartilaginous and synovial. Fibrous joints are those in which the bony surfaces have very little relative motion, a good example being the bones in the skull. Cartilaginous joints are those in which the bony surfaces have a little more relative motion such as the joint between two adjacent vertebrae. The third type are synovial (or diarthrodial) joints, for example the knee joint and hip joint, which are the joints focused on in this thesis.

1.2.1 Hip joint and knee joint

The hip joint can be considered as a ball-and-socket joint (Figure 1.1). This arrangement enables the hip to have a large amount of motion needed for daily activities like walking, squatting, and stair-climbing. The bones of the hip are the femur and the pelvis. The top end of the femur is shaped like a ball called the femoral head. The femoral head fits into a spherical socket on the side of the pelvis. This socket is called the acetabulum. The femoral head is attached to the rest of the femur (Figure 1.1).

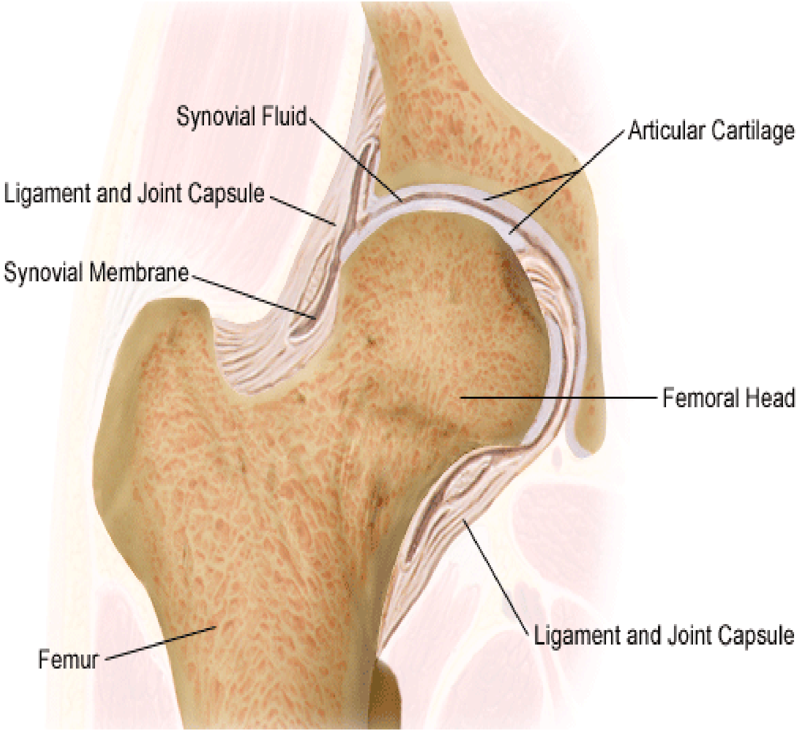

Figure 1.1 Hip Joint (Orthopaedics,2007)

Articular cartilage is a white and shiny material that covers the ends of the bones of hip joint (the femoral head and acetabulum in the pelvis). The function of articular cartilage is to distribute the stress and provide an articulation resistant to damage with low friction and wear.

The knee joint, the largest and most complex joint in the body, is the junction of three bones: the femur, the tibia, and the patella. In the knee joint, cartilage covers the inferior ends of the femur, the superior end of the tibia, and the back of the patella (Figure1.2). More details of articular cartilage will be discussed in the following section.

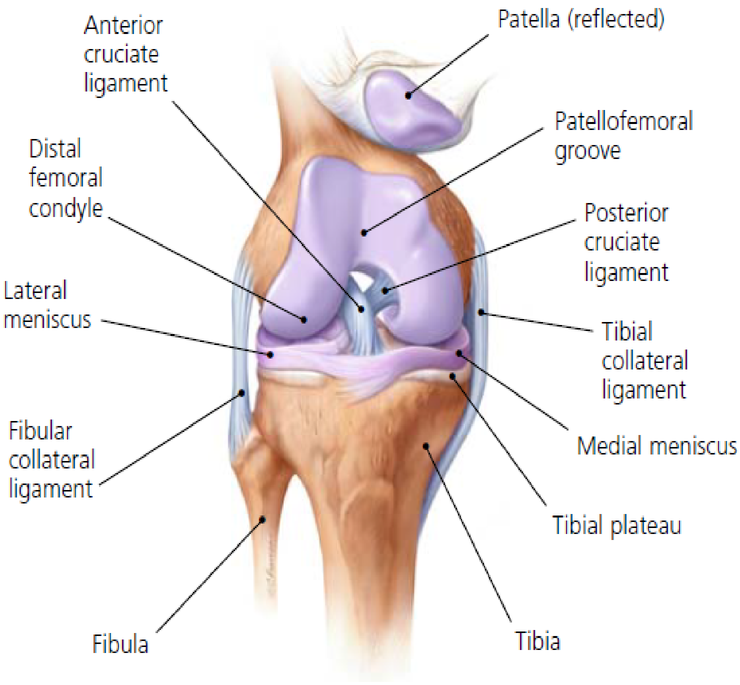

Figure 1.2 Knee joint (Tandeter et al., 1999).

1.2.2 Motion and load

1.2.2.1 Motion of hip joint and knee joint

As a ball-in-socket joint, the bony structures and ligaments of the natural hip limit anterior/posterior and medial/lateral translation as well as subluxation (dislocation); however, it does not generally limit the range of motion of the hip during normal daily activities. The allowable range of motion of a hip is shown in Table 1.1 for a selection of daily activities (Stewart et al., 2006).

Table 1.1 The ranges of motion in the hip during daily activities (Stewart and Hall, 2006).

	Allowable	**Walking**	**Tie Shoe**	**Stairs**
Flexion/extension	140°/30°	30°/15°	129°	40°
Internal/external rotation	90°/90°	4°/9°	18° abd.	n/a
Abduction/adduction	90°/30°	7°/5°	13° ext.	n/a

abd. = adduction;   ext. = extension

Unlike the ball-in-socket geometry of the hip, the femoral and tibial surfaces of the knee are not a close fit to one another. The variation in geometry allows a wide range of motion to occur which enables various daily activities. The allowable ranges of motion in the knee are shown in Table 1.2 for a selection of daily activities (Stewart and Hall, 2006).

Table 1.2 The ranges of motion in the knee during daily activities (Stewart and Hall, 2006).

	Allowable	**Walking**	**Sitting**	**Stairs**
Flexion/extension	150°/−5°	70°/0°	100°-120°	70°-90°
Internal/external rotation	±6°/±30°	±10°	n/a	n/a
Abduction/adduction	0-10°	0°	n/a	n/a

In the less conforming knee, the articulation is also supported by menisci which distribute stress and stabilize the joint as illustrated in Figure 1.2.

1.2.2.2 Joint loading in hip joint and knee joint

Typical loads measured within the body during various activities for the hip and knee are shown in Table 1.3. The walking cycle is characterised by two peaks of load at heel-strike and at toe-off which generally range from 3 to 4 times body weight (BW; Table 1.3; Paul, 1966). Between the two loading peaks the mass of the body (head and torso) does not exhibit any significant translation in the vertical direction, so the reaction force during this period is relatively small.

At toe-off the hip is extended 15° (Table 1.1). The quadriceps muscle acts to stabilise the knee whilst the gastrocnemius muscle produces plantar flexion at the ankle. These muscle forces combine to accelerate the body forward producing the second peak of load in the reaction force curve (Stewart and Hall, 2006).

Table 1.3 Joint loading in the hip and knee (Stewart and Hall, 2006).

Activity	Reference	Hip load	Knee load
Walking	Freeman and Pinskerova		3.4 BW
	Paul	3–4 BW	3 BW
	Bergmann *et al.* (*in vivo* normal)	2–3 BW	
	Bergmann *et al.* (*in vivo* defective)	3–4 BW	
Stair ascent/ descent	Freeman and Pinskerova		4.8/4.3 BW
	Costigan *et al.*		3–6 BW
	Paul		4.4/4.9 BW
	Bergmann *et al.* (*in vivo* normal)	2–3.5 BW	
	Bergmann *et al.* (*in vivo* defective)	3.5–5 BW	
Rising from a chair	Ellis *et al.*		3.2 BW
	Bergmann *et al.* (*in vivo* normal)	1.75–2.25 BW	
Rising from a squat	Dahlkvist *et al.*		4.7–5.6 BW
	Paul		4.2 BW

(BW = Body Weight)

1.3 Articular Cartilage

1.3.1 Composition and structure of articular cartilage

Articular cartilage can be considered as a solid matrix saturated with water and mobile ions. The solid matrix consists of chondrocytes embedded in extracellular matrix. The two major components of the extracellular matrix are collagen fibres composed of collagen fibrils and proteoglycans (PGs) which are large, complex biomolecules composed of a central protein core with negatively charged glycoaminoglycan (GAG) side chains looking like bottle-brushes (Figure 1.3; Maroudas, 1975).

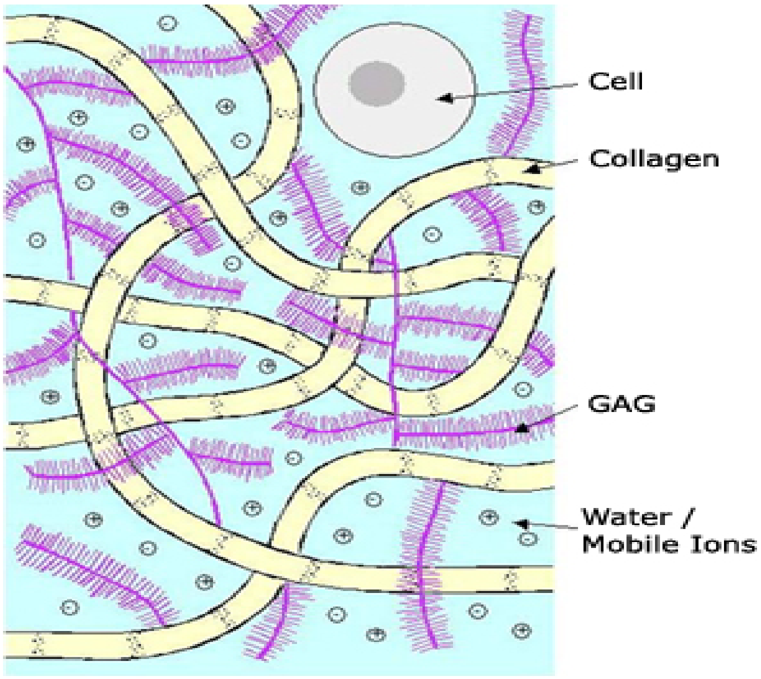

Figure 1.3 Schematic depiction of cartilage composition (source: www.bidmc.org/ Research/Departments/Radiology/ Laboratories/ Cartilage).

1.3.1.1 Structure of articular cartilage

Articular cartilage can be divided into four different layers, or zones. Moving from exposed surface to interface with subchondral bone, these layers are the superficial or the superficial transitional zone (STZ); the middle zone; the deep zone and the calcified cartilage zone (Figure 1.4).

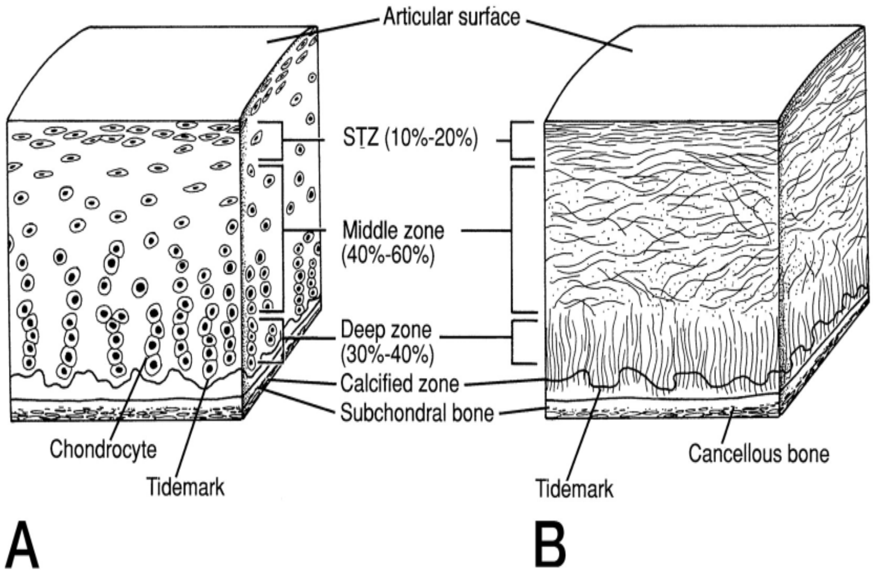

Figure 1.4 Schematic depiction of articular cartilage's structure (Buckwalter et al., 1994)

Superficial zone

The superficial surface zone is the thinnest and forms the gliding surface of the joint. Collagen and water content are highest in this zone, (water content is approximately 85%; Maroudas 1979). The chondrocytes appear flattened and are relatively inactive. Cell volume is smaller, cell density is higher (Figure 1.4 A) and aggrecan content is lower in the superficial zone compared to the deeper zones. Collagen fibres are densely packed, have a small diameter, and are arranged parallel to the articular surface (Figure 1.4

B; Wong *et al.,* 1996). Collagen and PGs appear to be strongly interconnected in this zone, which may help the superficial zone to resist shear stresses produced by motion (Mow *et al.,* 2002).

Middle zone

The middle zone occupies several times the volume of the superficial zone. The collagen fibres are more randomly arranged and have a larger diameter than in the superficial zone (Figure 1.4 B, Hasler *et al.,* 1999). The chondrocytes appear rounded and are larger and more active than in the superficial zone (Figure 1.4 A). PG content is high in this zone and aggrecan aggregates are larger than in the superficial zone (Buckwalter *et al.,* 1991).

Deep zone

The collagen fibres have their largest diameters and are arranged perpendicular to the subchondral bone in the deep zone (Figure 1.4 B; Hunziker *et al.,* 1997). This zone has the lowest water content (approximately 60%) and a high PG content (Maroudas, 1975). The chondrocytes tend to be aligned in radial columns (Figure 1.4 A) and the synthetic activity of the chondrocytes is highest (Wong *et al.,* 1996 and 1997).

Calcified cartilage zone

The calcified cartilage zone acts as a transition layer between bone and cartilage. It is separated from the deep zone by an interface plane called the tidemark (Figure 1.4, Hasler *et al.,* 1999). The cartilage is calcified with crystals of calcium salts and has low PG content. The collagen fibres from the deep zone cross the tidemark and insert the calcified zone providing a strong anchoring system for the tissue on the subchondral bone (Figure 1.4 B; Hunziker *et al.,* 1997). The thickness of the calcified zone is approximately 5%, with a range of 3–8%, of the total cartilage thickness (Oegema *et al.,* 1997). This zone is calcified to the same extent as bone although less stiff than bone, it is 10-100 times stiffer than cartilage (Mente *et al.,* 1994).

1.3.1.2 Composition of articular cartilage

Proteoglycans

Proteoglycans (PGs) form approximately 30–35% of the dry tissue weight (Buckwalter *et al.,* 1991). As large supramolecular complexes, PG is formed by GAGs and proteins in the extracellular matrix which are associated through covalent and non-covalent interactions. GAGs attach to a central chain made of hyaluronic acid (Figure 1.5). The side chains of the PGs can electrostatically bind to the collagen fibrils to form a cross-linked rigid matrix (Figure 1.5). So the extracellular matrix of cartilage can be seen as a composite structure of collagen type II fibrils with intertwining PG aggregates (Junqueira*,* 1983).

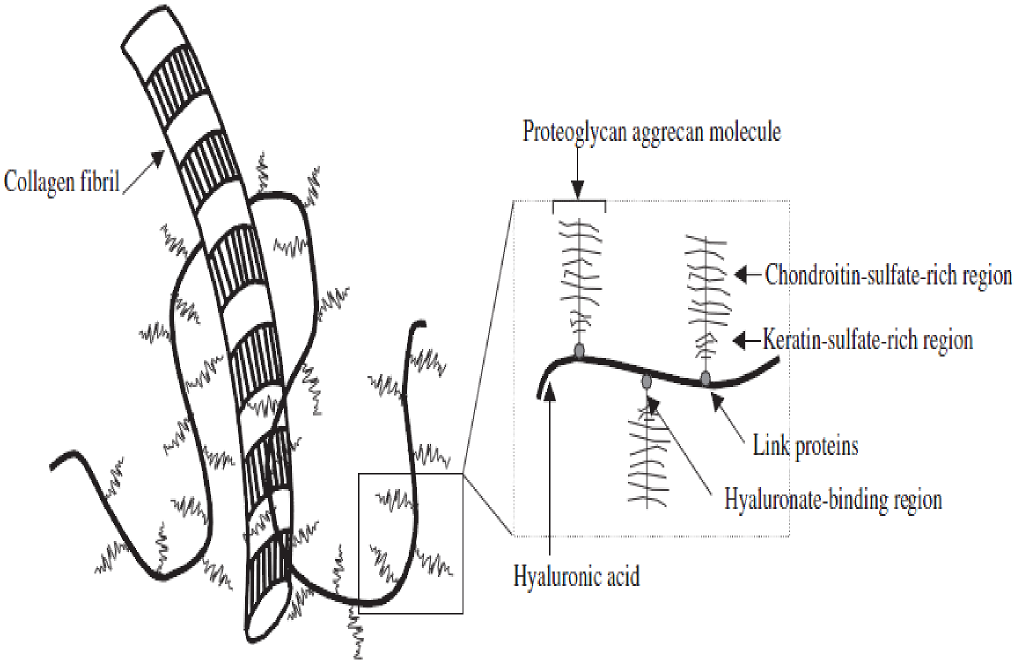

Figure 1.5 Schematic depiction of PG structure (Larry W, 2003)

Collagen

Collagen occupies approximately 50–75% of dry tissue weight of articular cartilage ((Buckwalter *et al.,* 1991; Mow *et al.* 2002), primarily being type II collagen (80–85%) with smaller amounts of collagen types V, VI, IX, X, and XI (Cremer *et al.,* 1998; Hasler *et al.,* 1999). Collagen molecules assemble to form small fibrils and larger fibres with dimensions varying through the depth of the cartilage layer (Eyre, 1991; Clarke, 1971 and 1991).

The direction of collagen fibers on the cartilage surface can be determined by the split-line pattern using a dissecting needle dipped in India ink to insert into the cartilage (Figure 1.6 (a); Steven et al., 2002 and Brian et al., 2004). The preferential orientation of collagen fibers could be identified by the resulting split between the collagen fibers at each needle insertion point (Figure 1.6 (b); Steven et al., 2002 and Brian et al., 2004).

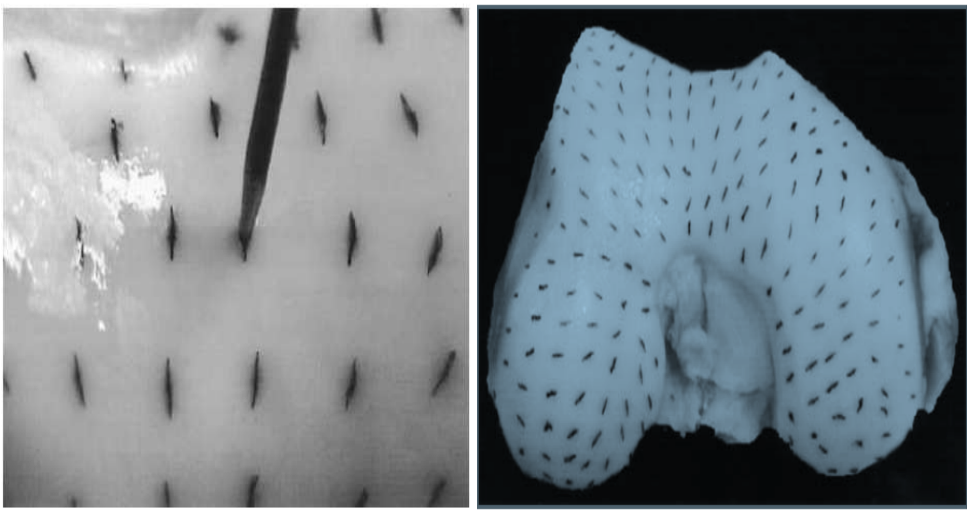

(a) (b)

Figure 1.6 (a) Cartilage surface showing the creation of the split lines with a dissecting needle that has been dipped in India ink; (b) Photograph showing the split-line pattern of a distal femoral specimen (Steven et al., 2002).

Collagen fibres are arranged in a columnar manner under the surface zone (Figure 1.7a; Kaab et al., 1998). Collagen columns are perpendicular to the surface in the middle and deep zones, with some fibres running obliquely (Figure 1.7b; Kaab et al., 1998).

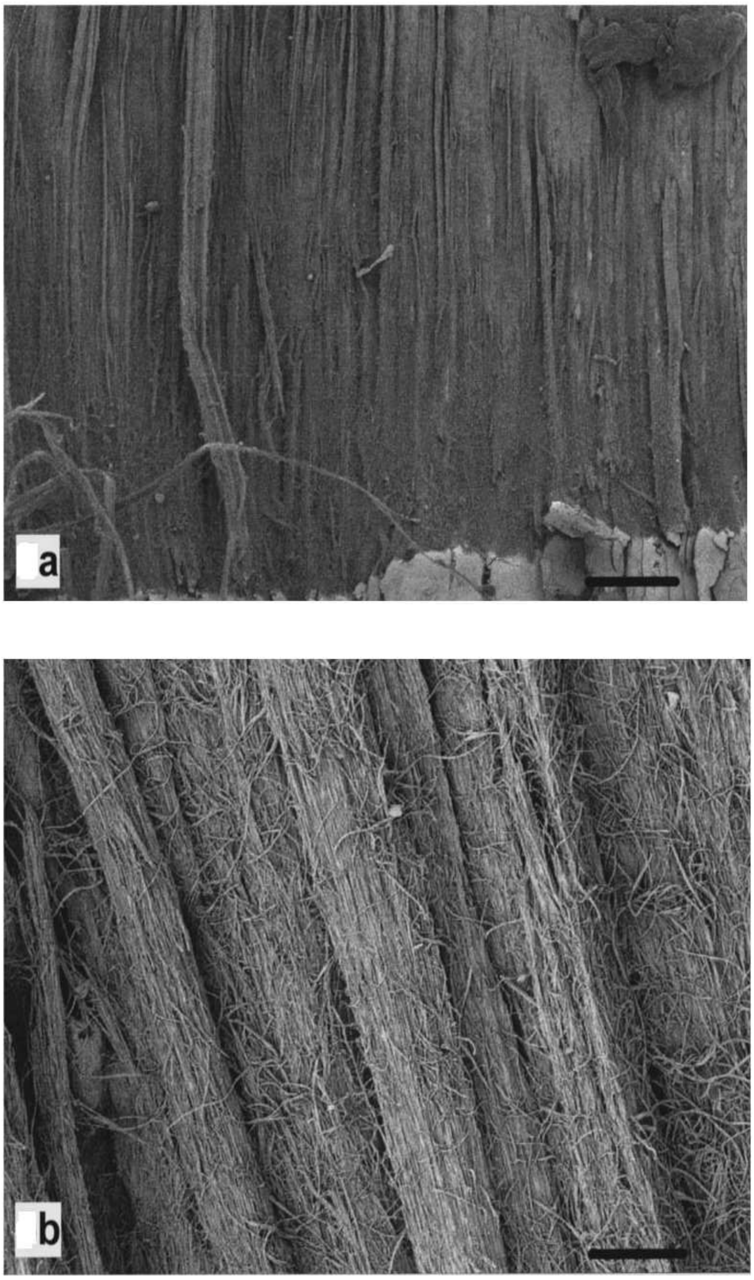

Figure 1.7 Bovine cartilage: (a) Collagen columns run perpendicular to the surface. (b) A column consists of parallel collagen, perpendicular to the surface in the deep zone (Kaab et al., 1998).

Collagen fibers do not offer significant resistance to compression along their axial direction, but do provide stiffness in tension (Akizuki *et al.,* 1986; Roth *et al.,* 1980). The collagen network resists the swelling of the articular cartilage: the PG molecules normally occupy a large space when not compacted by a collagen network. The compaction of the PGs affects swelling pressure as well as fluid motion under compression. Hence, the collagen network provides resistance against swelling and tensile strains (Mow, 1991).

The stiffness of the collagen network is highly influenced by the amount of cross-links which can be divided in two different categories of interaction: One involves physical entwinement not allowing for network disconnection unless actual fibril breakage occurs (Silyn-Roberts *et al.,* 1990), and the other does not involve entwinement.

Located at the exterior of the fibrils, type IX collagen appears to play an important role in stabilising the 3D organization of the collagen network (Eyre, 1987). It thus contributes to the ability of collagen to resist the swelling pressure caused by PGs and the tensile stresses developed within the tissue when loaded (Maroudas, 1976; Mow, 1992).

Covalently linked with collagen type II and buried within the fibrils, collagen type XI is believed to regulate the size of fibrils (Cremer *et al.,* 1998).

Chondrocytes

Chondrocytes are enclosed within small cavities (called lacunae) occupying 10-20% of the volume of articular cartilage; they are relatively flattened with elliptical cross-sections in the superficial zone but become more rounded in the middle zone (A and B in Figure 1.8; Thomas et al., 2005). In the deep zone, chondrocytes tend to be grouped in vertical stacks and the individual cell shapes display high variability (Figure 1.8 C; Thomas et al., 2005).

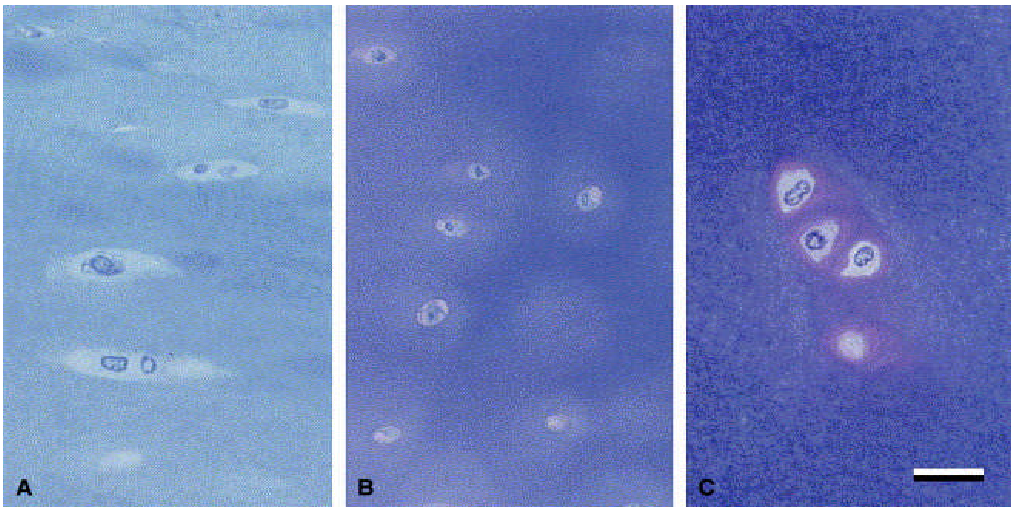

Figure 1.8 Light micrographs of normal adult human articular cartilage originating from (a) the superficial zone, (b) the middle zone, and (c) the lower deep zone (Thomas et al., 2005).

Interstitial fluid

Of the three major components in articular cartilage, the most prevalent (68-85% weight) is the interstitial fluid which consists of water and small electrolytes, primarily Na^+ and Cl^-. Most of the interstitial fluid is free to flow within the porous solid matrix (Ateshian 2009). Further details of the interstitial fluid will be discussed in Section 1.4.

1.3.2 Biphasic lubrication of articular cartilage

Researchers have been interested in the lubrication of articular cartilage from the early part of the eighteenth century (Hunter, 1743). The low friction and wear of AC layers is attributed to mixed modes of lubrication: (a) fluid film lubrication by synovial fluid (Dowson *et al.*,1969); (b) boundary lubrication by various molecules in synovial fluid and cartilage (Charnley, 1960; Jay *et al*., 2001; Radin *et al.*, 1972; Schmidt *et al*., 2007; Swann *et al.* 1972; Walker *et al.,* 1968); (c) biphasic lubrication by pressurisation of the interstitial fluid of cartilage (McCutchen, 1959; McCutchen, 1962; Forster *et al.*, 1996; Krishnan *et al.*, 2004b). The conception of fluid load support W_p/W (Forster and Fisher, 1999) - the fraction of the total load (W) supported by fluid pressurisation (Wp), plays a critical role in the lubrication mechanism of articular cartilage (Ateshian *et al.*, 1995; Macirowski *et al.*, 1994; McCutchen, 1959; Oloyede *et al.*, 1993 and 1996).

While other models (Gu *et al.*, 1998; Huyghe *et al.*, 1997 and 2002) exist, most of the recent tribological studies on articular cartilage have centred on biphasic, boundary and mixed lubrication regimes. This section will focus on biphasic lubrication mechanism as it is more pertinent to the current study.

1.3.2.1 Interstitial fluid pressurisation

Articular cartilage is highly porous (porosity in the range of 75% - 80%) but with a very small effective pore size in the range of 2.0 - 6.5 nm (Dowson, 1990). This leads to a very low permeability value in the range of 10^{-16} - $10^{-15}m^4/(Ns)$. When the tissue is compressed, the flow of interstitial fluid is thus accompanied by large drag forces and generates pore pressure to support the applied load (Katta *et al.*, 2008). This proposed mechanism was described as “self-pressurised hydrostatic bearing” by McCutchen (1959). Several experimental measurements of interstitial fluid pressurisation in articular cartilage have been reported in confined and unconfined compression (Oloyede *et al.,* 1991; Park *et al.,* 2003; Soltz *et al.,* 1998 and 2000a).

Confined compressive tests have been used extensively to study the creep and stress-relaxation behaviours of articular cartilage. In a typical stress relaxation test, a cylindrical cartilage plug is loaded (constant displacement) with a rigid porous plate (or indenter) in a confined chamber. Importantly, the confining chamber prevents radial expansion and lateral fluid flow out of the specimen. Under such a test configuration, fluid exudation and exchange with the solution reservoir can only happen through the porous plate across the surface of the cartilage sample (Figure 1.9; Mow *et al.*, 1989).

Figure 1.9 shows the stress and fluid redistribution in cartilage tissue while under a displacement load (Mow *et al.*, 1989). During the ramped displacement, stress levels increase in cartilage tissue due to fluid pressurization. When compressive strain is held constant, fluid pressurization decreases and stress relaxation takes place in the tissue due to fluid redistribution, and dissipation of hydrostatic pressure developed during compression.

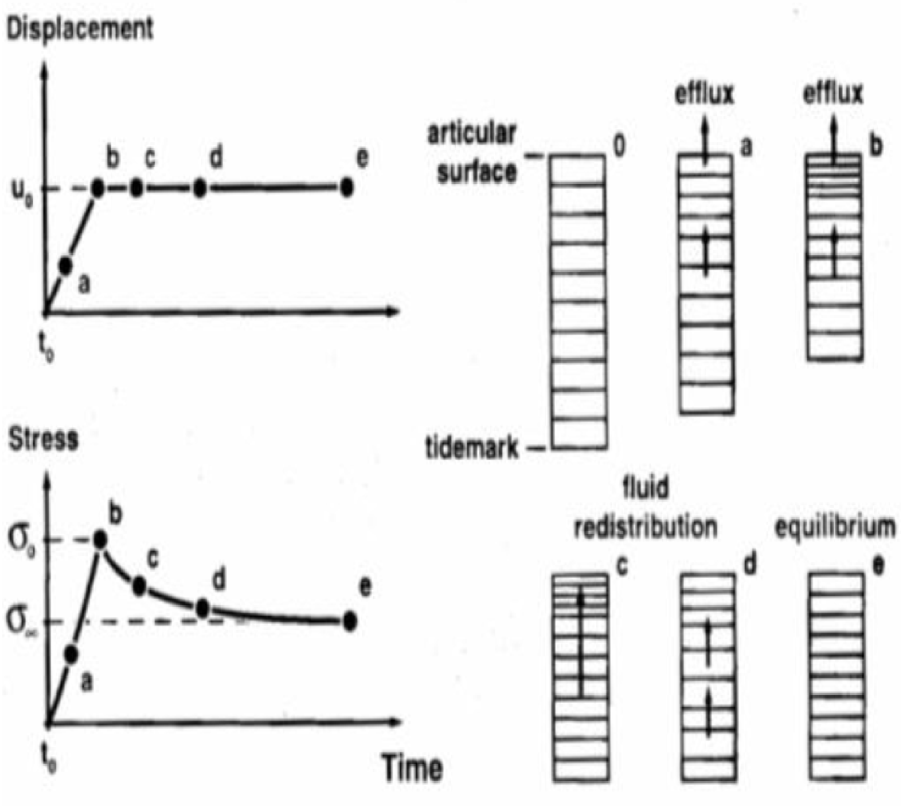

Figure 1.9 The stress-relaxation response shows a characteristic stress increase during the compressive phase and then the stress decreases during the relaxation phase until equilibrium is reached (point e). Fluid flow and solid matrix deformation during the compressive process give rise to the stress-relaxation phenomena (Mow *et al.*, 1989).

In a confined compressive creep test of Soltz *et al.* (1998), the interstitial fluid pressure was observed to rise rapidly to a value equal to the applied compressive stress once a constant load applied. Then the pressure slowly subsided back to zero at a rate comparable to that of the creep deformation (Figure 1.10).

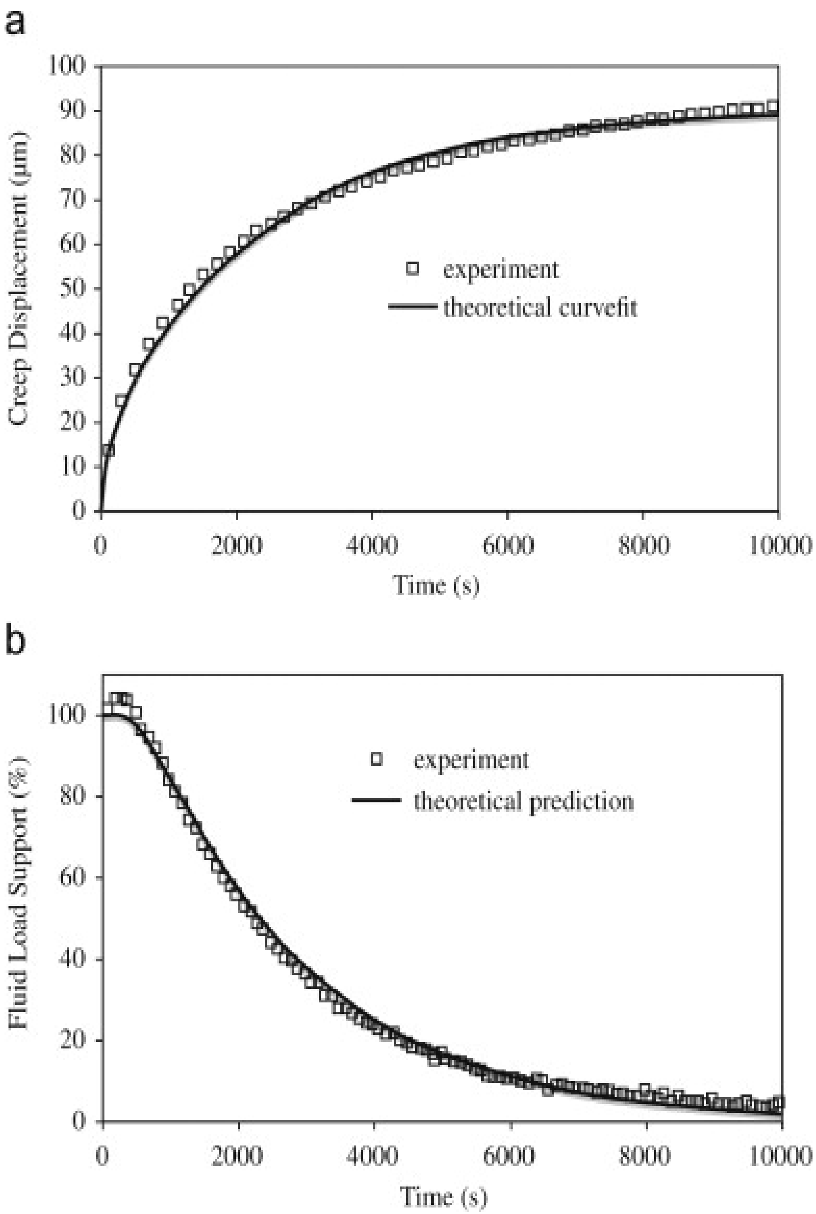

Figure 1.10 Confined compression creep response of bovine articular cartilage (square symbols denote experimental data and the solid curve represents a curve-fit of the experimental response using the biphasic theory): (a) creep deformation versus time; (b) Ratio of interstitial fluid pressure to applied stress, at the cartilage face abutting the bottom of the confining chamber (Soltz *et al.*, 1998).

Since the fluid pressure is equal to the applied stress upon initial load application (Figure 1.10b) whereas the creep deformation is zero (Figure 1.10a), it is possible to conclude that all applied load is initially supported by the pressurised interstitial fluid and none by solid matrix. Interstitial fluid cannot escape from cartilage instantaneously, the cartilage specimen must maintain its volume immediately following the application of a step load; but the specimen is surrounded by rigid walls, so an isochoric (volume-conserving) deformation cannot occur initially--the only manner by which the tissue can resist the applied load is via interstitial fluid pressurization. As time progresses, the pressurised interstitial fluid flows out of the tissue through the porous indenter, leading to a progressive reduction in fluid pressure and an increase in solid matrix deformation. Thus, over time, the load becomes progressively more supported by the solid matrix (Soltz *et al.*, 1998).

1.3.2.2 Cartilage lubrication by interstitial fluid load support

The rate and direction in which the interstitial fluid can flow in articular cartilage is ultimately determined by the microstructure of the porous network, and how it deforms under loading and shearing stresses. The mechanical properties, deformation response, and friction of cartilage under compression are therefore also determined by these same factors (Quinn *et al.*, 2000).

In the late 1950s, McCutchen and co-workers initially proposed an explanation for the mechanism of lubrication in articular cartilage using the concept of “self-pressurised hydrostatic bearing”. When two cartilage layers in the joint are pressed together, the interstitial fluid is pressurised. The pressurised fluid supports most of the applied load, while only a small fraction is supported by the solid matrix. The pressurization can remain until the interstitial fluid exudes into the joint space or other unloaded regions (Katta *et al*., 2008). According to this load sharing mechanism, frictional forces between the opposing articular layers would be only significant when the portion of the applied load transfers across the solid matrices of cartilage (Lewis *et al.*, 1959; McCutchen, 1959, 1962 and 1983).

In an experiment of cartilage disk articulating against glass configuration, Krishnan *et al.* (2004) illustrated a linear negative relationship between the interstitial fluid load support and the coefficient of friction of articular cartilage (Figure 1.11).

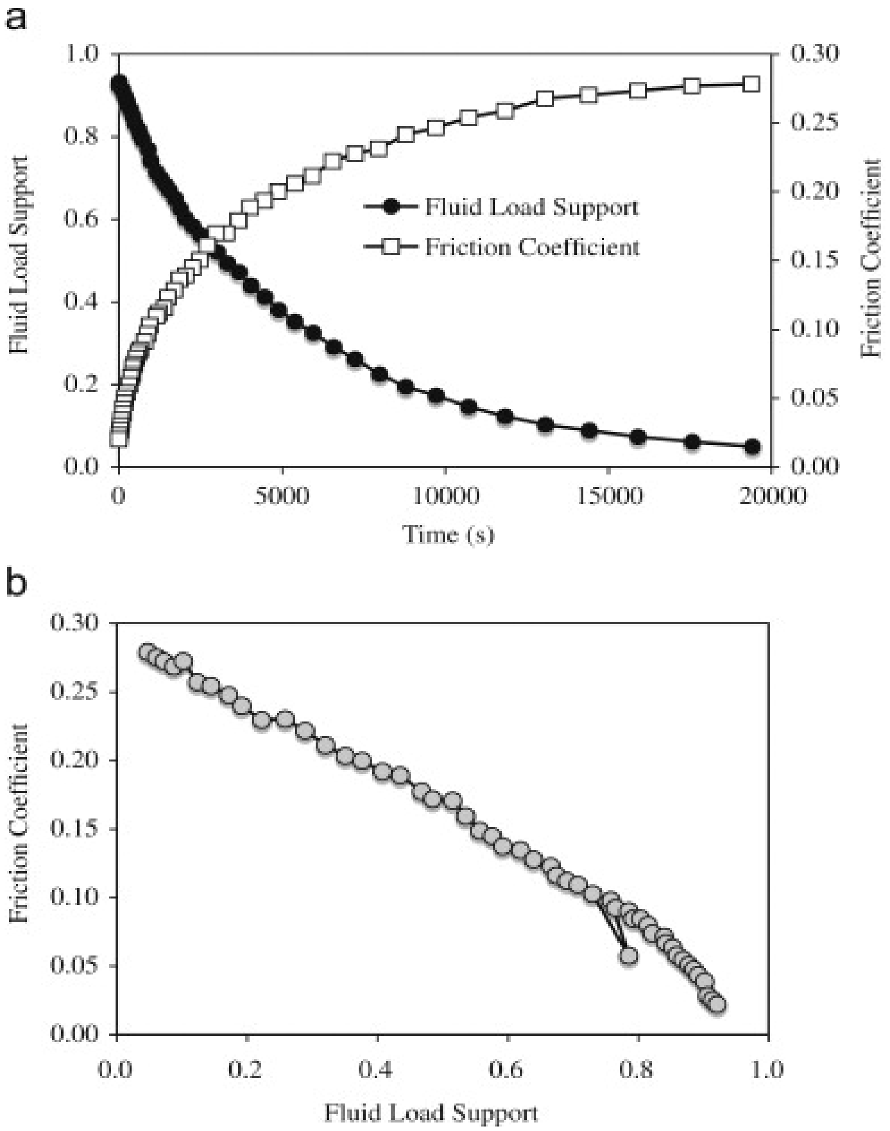

Figure 1.11 (a)Time-dependent response of the friction coefficient μ_{eff} and interstitial fluid load support W_p/W (b) A linear variation plot of μ_{eff} versus W_p/W (Krishnan *et al.*, 2004).

The phenomenon in Figure 1.11 was first called ‘biphasic lubrication’ by Forster and Fisher (1996). Measuring the coefficient of friction in an in-vitro pin-on-plate setup using cartilage against metal and cartilage-against-cartilage configurations for different loading times, Forster and Fisher (1999) proposed that the friction force at the articular surface was proportional to the load carried by the solid phase.

In order to describe the relationship between the effective friction coefficient μ_{eff} and the interstitial fluid load support W_p/W (Forster and Fisher, 1999) of articular cartilage, Ateshian (2003) gave a formula:

$$\mu_{eff} = \mu_{eq}\left[1-(1-\varphi)W_p/W\right] \qquad 1.1$$

where μ_{eq} is the equilibrium coefficient of friction, φ is the fraction of the (apparent) contact area where the solid matrix of one of the bearing surfaces in contact with the solid matrix of the opposing bearing surface ($0 \leq \varphi \leq 1$). Using the formula, Ateshian demonstrated the role of the interstitial fluid load support in dynamic loading which simulates the joints' rolling or sliding contact during normal activities of daily living (Ateshian, 2009).

1.4 Computational Modelling of Articular Cartilage

Experimental studies could provide fundamental information on cartilage biomechanics. However, they are unable to measure a number of biomechanical parameters within the tissue particularly the pore pressure and fluid flow. So it is necessary to use simulation-based numerical methods, such as finite element analysis to investigate these variables and interpret the biomechanical and biophysical basis of the experimental results. With the availability of validated commercial finite element codes (Wu *et al.*, 1998), the application of such computational models to predict articular cartilage behaviour including tribology and fluid load support has become more achievable (Ateshian, 2009).

As the understanding of the structure and behaviour of articular cartilage has improved, so have the material models used in finite element models of cartilage. As the earliest, single-phase constitutive models only considered the solid phase of the tissue leading to limited capabilities to describe the time-dependent response which is mainly due to the interstitial fluid flow in compressed cartilage (Kazemi.et al., 2013).

Accounting for the effects of fluid pressurization, both solid and fluid phases were considered in the second generation of constitutive models - the poroelastic or biphasic models. According to the biphasic theory of Mow *et al.* (1980), articular cartilage was assumed to consist of an incompressible porous solid matrix, hydrated with an incompressible fluid. The solid matrix consists of chondrocytes embedded in an extracellular matrix of which the major components are collagen molecules and proteoglycans. Loading on the cartilage and the subsequent tissue deformation causes pressurization and flow of interstitial fluid. The time dependent mechanical responses of cartilage (e.g., creep and stress relaxation) was seen as the dissipative effects of this fluid flow in the biphasic models. The poroelastic model assumed linear elasticity of the solid matrix, constant permeability and infinitesimal deformation of the tissue (Biot, 1941). The linear poroelastic equations are derived from the equations of linear elasticity for the solid material. But when the cartilage was under high strain-rate compression, neither poroelastic nor biphasic models had enough capabilities in describing the short-term, time dependent response (Kazemi et al., 2013).

Furthermore, the difficultly solved governing equations confines most analytical work to a simple geometry of cartilage layers. Quiñonez et al. (2010) developed the solution of this problem using Laplace transforms, in the form of an asymptotic series.

The fibril-reinforced models may be considered as the third generation of the constitutive models for cartilage which can account for high fluid pressurization in the tissue (Li *et al.*, 1999 and Soulhat et al., 1999). In the fibril-reinforced models, articular cartilage was considered as an isotropic porous matrix saturated in water, reinforced by a fibrillar network. The porous matrix was nonfibrillar, representing the solid matrix excluding the collagen fibrils. The nonfibrillar matrix was modeled as a continuous linearly elastic material with *Young*'s modulus and *Poisson*'s ratio. The collagen fibrils were simulated separately with nonlinearly elastic or viscoelastic properties in different models. The stress of the fibril-reinforced material was given by the sum of the porous matrix and the fibrillar network.

Compared to the second generation of constitutive models without fibril reinforcement, a fibril-reinforced model could reasonably predict the stresses in the cartilage under fast compressions (Li *et al.*, 2003) while the fibrillar nonlinearity was stressed.

From the view of simulating the tissue structure, the constitutive models of cartilage were classified as two types: the macroscopic models without consideration of the underlying tissue structure and the microstructural models mimicking the fibrillar network and the nonfibrillar matrix separately (Taylor *et al.*, 2006).

The macroscopic models characterized cartilage only on the basis of its bulk mechanical response and masked the different load-supporting manner of each individual component of the tissue. Both the single-phase and the poroelastic (or biphasic) models were designated as macroscopic models since they lump all of the solid tissue components together (Taylor *et al.*, 2006). Differentiating contributions of the collagen fibrillar network and the nonfibrillar matrix of cartilage, the fibril-reinforced poroelastic models were treated as microstructural models. Such models naturally incorporated the anisotropic mechanical property as a result of the specific arrangement of collagen fibrils (Taylor *et al.*, 2006).

1.4.1 The biphasic background

According to the biphasic theory of Mow et al. (1980), articular cartilage is assumed to consist of an incompressible porous solid matrix, hydrated with an incompressible fluid. As introduced in Section 1.3, loading on the cartilage and the subsequent tissue deformation causes pressurization and flow of interstitial fluid. The time dependent mechanical responses of cartilage (e.g., creep and stress relaxation) is seen as the dissipative effects of this fluid flow.

Assuming the fluid phase is inviscid, Simon (1992) proved the equivalence between the linear biphasic model (Mow et al. 1980) and the poroelastic model of Biot (Biot, 1941). So poroelasticity is an effective means to represent the material property of articular cartilage. In order to describe the mechanical behaviour of cartilage, at least an isotropic linear poroelastic model should be used in the computational modelling. This model assumes linear elasticity of the solid matrix, constant permeability and infinitesimal deformation of the tissue. The linear poroelastic equations are derived from the equations of linear elasticity for the solid material.

1.4.2 The macrostructural FE models of articular cartilage

1.4.2.1 The isotropic poroelastic model

The isotropic poroelastic model has been used to simulate the loading experiments of articular cartilage such as confined compression (Ateshian *et al.*, 1997; Bursac *et al.*, 1999), unconfined compression (Bursac *et al.*, 1999; Armstrong *et al.*, 1984), indentation (Mak *et al.*, 1987; Mow *et al.*, 1989; Suh *et al.*, 1994), and impact (Atkinson *et al.*, 1995; Garcia *et al.*, 1998).

The isotropic poroelastic model describes the time-dependent deformation of articular cartilage coming from the interstitial fluid flow. However, important features like tension-compression nonlinearity of cartilage caused by the large disparity in the very high tensile modulus compared with the low compressive modulus has not been included. This means that the isotropic poroelastic model cannot give the satisfied simulation of the unconfined compression tests of articular cartilage, although it does simulate the experimental results of confined compression well.

1.4.2.2 The transversely isotropic poroelastic model

In the simulation of unconfined compression, good agreement between theoretical predictions and experimental measurements of the cartilage deformation was found to be achieved only after incorporating tension–compression nonlinearity in the modelling of cartilage solid matrix (Cohen et al., 1998; Soulhat et al., 1999) i.e. using transversely isotropic poroelastic model. Similar results happened to the interstitial fluid pressurisation: the peak interstitial fluid load support was measured to be as high as 99% in some cartilage specimens, whereas the simple isotropic model could only predict a peak value of 33% when using the isotropic poroelastic model where tensile and compressive properties are assumed identical. When accounting for tension-compression nonlinearity, the modified model could predict a fluid load support approaching 100% as the ratio of the tensile to compressive moduli increases in excess of unity (Park et al., 2003; Soltz et al., 2000b).

This finding shows the interstitial fluid pressurisation is greatly aided by the nonlinearity between the very high tensile modulus and the low compressive modulus of cartilage tissue. Although articular cartilage is primarily loaded in compression under physiological articular contact, it is now understood that the axial compression of the tissue is resisted by the high tensile modulus which prevents significant expansion in the directions transverse to the loading axis. In effect, the high tensile stiffness acts as the rigid side-wall of a confining chamber to resist lateral expansion; thus, even in unconfined compression, the interstitial fluid must pressurise noticeably to support most of the applied compressive stress. This observation considerably clarifies the functional role of collagen in articular cartilage, whose structure is best suited to resist tension, even though articular cartilage is normally subjected to compression. Since collagen is parallel to the articular surface in the superficial zone, this ultrastructural organisation appears to be optimised to provide the greatest amount of interstitial fluid load support at the articular surface (Ateshian, 2009). This was confirmed experimentally in a comparison of interstitial fluid load support at the articular surface versus the deep zone by Park et al. (2003): the fluid load support was 94±4% at the articular surface, but only 71±8% at the deep zone of immature bovine in articular cartilage.

Cohen et al. (1998) employed transverse isotropy to approximate the tension-compression nonlinearity for unconfined compression of in articular cartilage plugs (Table 1.4) where the tissue is in tension in the transverse plane (within which the modulus is high), and in compression in the axial direction (along which the modulus is significantly lower). This model considers cartilage depth-wise homogeneous and indirectly simulates the different properties in tension and compression, although it does provide better curve-fits of the experimental data than the linear biphasic poroelastic model in cartilage modelling (Cohen et al., 1998).

Table 1.4 Transversely isotropic biphasic properties of bovine distal ulnar growth plate and chondroepiphysis obtained from confined and unconfined compression tests (means ± std. dev.): **(a)** elastic moduli; **(b)** permeability coefficients (Cohen *et al.* 1998)

(a)	**E_3[MPa] compression**	**E_1[MPa] tension**	v_{21}	v_{31}
Growth plate	0.47 ±0.11	4.55 ±1.21	0.30± 0.20	0.0
Chondroepiphysis	1.07 ± 0.27	10.63 ± 2.72	0.30± 0.26	0.0
(b)	k_3 axial $[\times 10^{-15} m^4/(Ns)]$	k_1 radial $[\times 10^{-15} m^4/(Ns)]$	n/a	n/a
Growth plate	3.4 ± 1.6	5.0 ± 1.8	n/a	n/a
Chondroepiphysis	2.1 ± 1.0	4.6 ± 2.1	n/a	n/a

When Bursac et al. (1999) tested the same cartilage samples in confined compression, measuring the radial normal stress on the confining chamber's side wall; they found stress magnitudes two to three times smaller than predicted by the transversely isotropic model. This pointed out the limitation of simulating tension-compression nonlinearity with transverse isotropy.

1.4.3 The microstructural FE models of articular cartilage

1.4.3.1 The fibril-reinforced poroelastic model

In order to overcome the limitation of transversely isotropic poroelastic model on simulating tension-compression nonlinearity of articular cartilage, the fibril-reinforced models are used. In these models, the fibril network (collagen network) contributes to the mechanical stiffness of the material, in addition to the isotropic matrix. The total solid stress σ_t of the fibril-reinforced material is given by the sum of the matrix stress σ_m and fibril stress σ_f i.e. $\sigma_t = \sigma_m + \sigma_f$. By defining the nonlinearly viscoelastic, direction and location dependent mechanical properties of collagen fibrils, the anisotropy caused by the collagen network and flow-independent viscoelasticity of articular cartilage can also be included (Li *et al*., 2009).

Similar to the isotropic models, the nonlinearly viscoelastic equations of the mechanical properties of collagen fibrils in the fibril-reinforced models are also derived from the equations for the solid material. These equations, such as Fung's quasi-linear viscoelasticity (Fung, 1993, Section 7.6, Page 277-279), extend elastic formulations by incorporating the reduced relaxation functions $G(t)$ - a normalized function of time (Fung 1993, Page 280). The relaxation functions can effectively convert constant elastic moduli (e.g., λ and μ) into functions of time t. Isotropic symmetry is assumed normally so that the tensile stress in a cylindrical specimen under an infinitesimal stretch (small deformation), at time t with the superposition principle applies (Fung

1993, Page 278-279), may be presented in the form of a convolution integral (Fung 1993, Page 279):

$$T(t) = T^{(e)}(0+)G(t) + \int_0^t G(t-\tau)\frac{\partial T^{(e)}[\lambda(\tau)]}{\partial \tau}\,d\tau \qquad 1.2$$

where the ‘elastic response’ $T^{(e)}(\lambda)$ is a function of λ (Fung 1993, Page 278) and λ named the ‘stretch ratio’ for one-dimensional specimen loaded in tension (Fung 1993, Page 29); the ‘reduced relaxation function’ $G(t)$ is typically analyzed into exponential function of time (Fung 1993, Page 280) which can be written as (Fung 1993, Page 283):

$$G(t) = \left[1 + \int_0^\infty S(\tau)e^{-t/\tau}\,d\tau\right]\left[1 + \int_0^\infty S(\tau)\,d\tau\right]^{-1} \qquad 1.3$$

‘The continuous spectrum model described above can be replaced by a discrete spectrum model based on a hypothetical combination of Kelvin's standard viscoelastic discrete models (Puso et al., 1998). In this case, the reduced relaxation function can be written as a series of combinations of the discrete relaxation functions such as:

$$G(t) = G_\infty + \sum_{i=0}^{N_d} G_i\, e^{-t/\nu_i} \qquad 1.4$$

Here, $G_\infty = G(\infty)$; G_i is the discrete moduli; ν_i is the discrete relaxation time.' - equivalence between the two previous equations requires $G_\infty = 1$ (Suh *et al*., 1998).

These equations are used to derive the contribution of the fibrillar cartilage part to the Jacobian matrix $[D]$ which is demanded in the commercial FE package ABAQUS (Dassault Systemes, Suresnes Cedex, France). $[D] = \partial\Delta\sigma/\partial\Delta\varepsilon$, where $\partial\Delta\sigma$ are the stress increments and $\partial\Delta\varepsilon$ are the strain increments at a specific iteration of simulation (Abaqus User Subroutines Reference Manual 1.1.36 ‘‘UMAT”).

1.4.3.2 Comparison of various fibril-reinforced models

Four kinds of fibril-reinforced models i.e. spring model (Soulhat *et al.*, 1999; Li *et al.*, 1999-2003), continuum model (Li *et al.*, 2004 and 2009; Wilson *et al.*, 2004; 2005a; 2006 and 2007)**,** nonlinear shell membrane element model (Shirazi *et al.*, 2005 and 2007) and rebar-based model (Gupta *et.al.*, 2009) can be found in the literature simulating confined compression (CC), unconfined compression (UCC), indentation and swelling test (Table 1.5).

Table 1.5 Fibril-reinforced FE models of articular cartilage.

	Authors	**Configurations**	**Modelling details**
Spring-based models	Li *et al.*,1999	UCC	Nonlinear formulation; homogeneous.
	Li *et al.*,2000	UCC	Depth-dependent material properties.
	Li *et al.*,2001	UCC versus Release	Unequal load increments.
	Li *et al.*,2002	UCC	Healthy and pathological situation.
	Li *et al.*,2003	UCC (Strain rate and amplitude varying)	High strain rates.
	Korhonen *et al.*, 2003	UCC	Mechanical behaviour of normal, PG depleted and collagen degraded AC.
Continuum element models	Li *et al.*, 2004	UCC (large deformation)	Fibril reinforcement versus tissue volume change; load sharing between solid matrix and fluid pressurization; comparison of spring model and continuum model.
	Li *et al.*,2009	UCC; CC; indentation	3D fibril orientation; split-line pattern.
	Wilson *et al.*, 2004;	Indentation; UCC; CC	Depth-dependent collagen orientation and the compression-tension nonlinearity
	Wilson *et al.*, 2005a	UCC; CC; indentation and 1D-swelling tests	Depth-dependent collagen orientation and the compression-tension nonlinearity; osmotic swelling and chemical expansion.
	Wilson *et al.*, 2006	UCC; CC; indentation; 1D-swelling tests.	New laws for viscoelastic behaviour and permeability of the collagen network.
	Wilson *et al.*, 2007	UCC and CC; indentation and 1D-swelling tests	Intra- and extra-fibrillar water content; influence of the solid fraction on the compressive properties.
	Julkunen *et al.*, 2007 and 2008	UCC	Realistic collagen orientation (using PLM and MRI respectively).
	Julkunen *et al.*, 2010	UCC;CC; indentation (strain rate varying).	Fractional factorial design.
Membrane element models	Shirazi *et al.*, 2005	Indentation; UCC and CC	Individual adjustment of collagen volume fraction and mechanical properties.
	Shirazi *et al.*, 2008	Indentation	Horizontal and vertical membrane elements.
Rebar-based model	Gupta *et al.*, 2009	Nano indentation	Frictionless, finite sliding contact; evolving indenter surface fluid flow boundary condition.

The spring-based models

In spring-based models, fibrils are represented by springs between the nodes of the elements and can only be represented in the direction of the elements. The most sophisticated spring-based fibril-reinforced models are those of Li *et al.* (1999-2003). In their earlier models, the cartilage is modelled as an isotropic solid matrix containing fluid-saturated pores entrapped by a fibrillar network (Figure1.12).

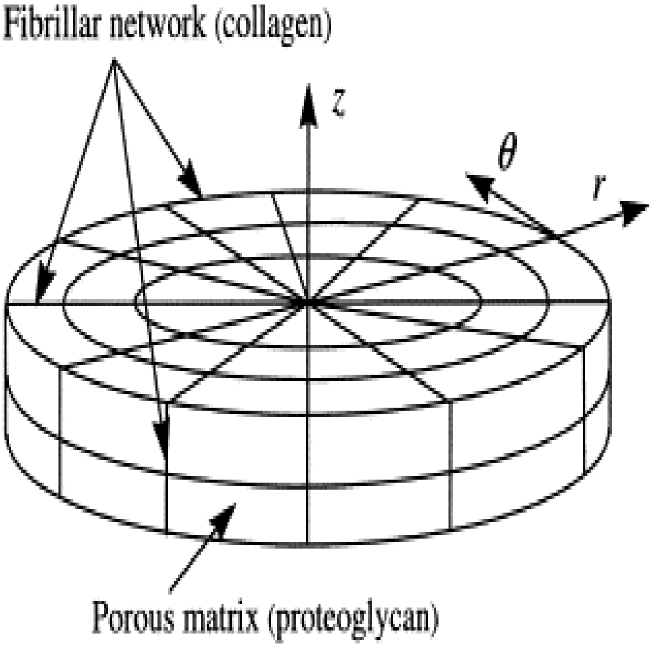

Figure1.12 Diagram of the model showing the isotropic matrix (containing pores) and the fibrils evenly distributed in the three orthogonal directions (Li *et al.*, 1999).

The isotropic matrix with pore fluid is considered as poroelastic, where both the solid and the fluid phases are assumed to be incompressible. These fibrils have no resistance to compression, i.e. the Young's modulus for compression is assumed to be zero. The effect of lateral deformation of every single fibril is also neglected. The only fibril stress considered is the tensile stress produced by stretching in the radial direction. This is a reasonable approximation given the slenderness of the collagen fibrils and their high stiffness in tension. Thus the fibrils employed in the model are one-dimensional (1D) nonlinear structural elements which do not support compression. An elastic theory applies to the fibril constituent while a poroelastic theory is employed for the biphasic component (Li *et al.*, 1999).

The displacements are interpolated at all nodes and are thus quadratic. The pore pressure is interpolated at the four corner nodes only and thus gives a bilinear variation within an element. On the other hand, the fibrils are represented by a system of special springs which resist tension only. Vertical springs are not necessarily presented when the contacts are non-adhesive, since they will undergo compression and thus develop no stress (pre-stresses are not considered due to lack of such data). The total stiffness of the horizontal fibrils within one continuum element domain is distributed between one longer and four shorter springs (Figure 1.13).

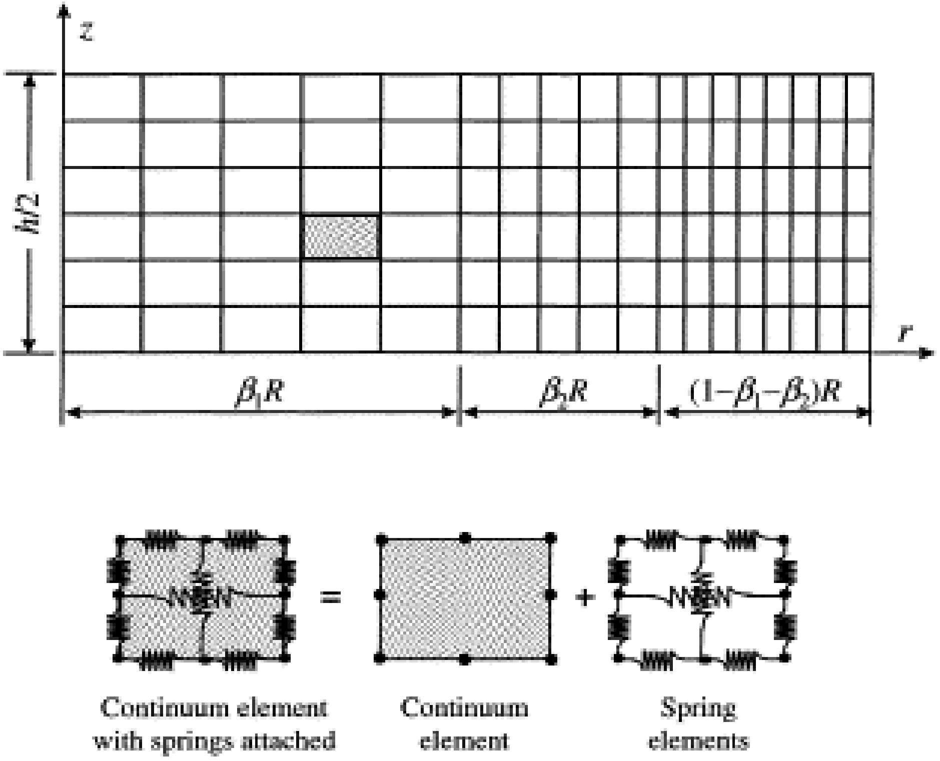

Figure 1.13 Mesh for the finite elements illustrating also the arrangement of spring elements in a porous continuum element. Displacements are interpolated by all nodes, but the pore pressure is interpolated by four corner nodes only (Li *et al.*, 1999).

It is assumed that the longer spring shares 2/3 of the total stiffness in order to guarantee a uniform stress state when a uniform strain is produced. The stiffness of the vertical springs can be determined in a similar way (Li *et al.*, 1999).

Using spring elements is an effective and economical method to represent the fibrillar matrix of articular cartilage in finite-element computational modelling. The spring-based fibril-reinforced biphasic models have been applied in unconfined compression, mainly for the characterization of the role of the collagen network in cartilage time-dependent response (Soulhat *et al.*, 1999 and Li *et al.*, 1999-2003). The most significant difference between the spring-based fibril-reinforced and the transversely isotropic model is that the fibrils in the first model resist only tension, while the second one has the same stiffness in compression and tension.

The continuum fibril-reinforced model

In the spring-based fibril-reinforced biphasic models, the standard porous element was adopted for the non-fibrillar matrix containing fluid; and the fibrillar matrix was discretised into two-node spring elements that were attached to the eight-node porous elements. This leads to the deformation incompatibility between the discretised matrices, and thus the validity of the discretisation. Therefore, a user-defined continuum element was introduced for the fibrillar matrix embedded in each porous element. Both the non-fibrillar and the fibrillar part of the solid matrix were included in one continuum element. The fibrillar continuum element shares the same nodes and geometry with the corresponding porous element. So this approach does not result in deformation incompatibility between the discretised matrices (Li *et al.*, 2004).

The continuum fibril-reinforced poroviscoelastic (FRPVE) models of Wilson *et al.* (2004 and 2005a) include depth-dependent collagen orientation and takes into account the compression-tension nonlinearity of AC. The primary collagen fibrils were assumed to be viscoelastic and were represented by a linear spring with stiffness E_0, parallel to a nonlinear spring with stiffness $E_1 = E_\varepsilon \times \varepsilon_f$ (E_ε is a positive material constant and ε_f is the fibril strain) in series with a linear dashpot with damping constant η. The FRPVE model was successfully used to describe confined compression, unconfined compression and indentation (Wilson *et al.*, 2004 and 2005a).

To account for the transient behaviour as well, the composition-based model (Wilson *et al.*, 2007) must be extended to include viscoelastic behaviour. It was combined with the FRPVE model and expanded with a new permeability law and a new law for the viscoelastic behaviour of collagen network. The new permeability law is based on the assumption that both the depth- and strain-dependencies of the permeability are governed by the same mechanism and are the direct result of the composition of the tissue. The combined model could simultaneously describe the behaviour of articular cartilage in confined compression, unconfined compression, indentation and two different 1D-swelling tests (Wilson *et al.*, 2006).

In order to set up the sample-specific FE models, Julkunen *et al.* (2007) derived specific collagen orientation patterns from quantitative microscopic analyses and depth-wise T2 profiles (Julkunen *et al.*, 2008), then implemented realistic collagen architecture into the depth-dependent FRPVE model (Wilson *et al.*, 2004 and 2005a). The implementation of collagen orientation into the FRPVE model enabled more realistic estimation of the spatial, depth-dependent stress and strain distribution in articular cartilage, as compared to models with homogeneous fibril distribution (Korhonen *et al.*, 2003 and Li *et al.*, 1999).

Recently, Li *et al.* (2009) and Pierce *et al.* (2010) successfully implemented the realistic orientation of collagen fibril into the fibril-reinforced continuum models. The fibril orientation was derived by the split-pattern and Diffusion Tensor (DT) Magnetic Resonance Imaging (MRI) method respectively.

Generally speaking, the discrete model with the fibrillar spring system appeared to be slightly stiffer than the model consisting of continuum elements only due to the deformation incompatibility between the discretised matrices, especially at larger strains (Li *et al.*, 2004).

The membrane shell element model

Neither the spring-based nor the continuum fibril-reinforced model explicitly accounts for the important physical properties of the tissue, such as nonlinear stress–strain curves of the fibril networks at different locations and directions. To modify these models, Shirazi *et al.* (2005 and 2007) used membrane shell elements to directly represent fibril network in both axisymmetric and 3D model studies**.**

In the nonlinear membrane element fibril-reinforced model, the solid isotropic porous matrix of the cartilage filled with water is represented, in a 3D mesh, by 8-node or 20-node elements with regular or reduced integrations. The pressure field is taken linear in different directions while the displacement fields are either linear or quadratic. The fibrils are introduced by four-node or eight-node shell membrane elements with, respectively, linear and quadratic displacement fields. The collagen fibrils in the plane of membranes are assumed to be homogeneously distributed in all directions.

Despite such distribution, a direction-dependent response prevails due to the strain-dependency in the fibrils material properties and anisotropy in the strain field. At each step of loading, principal strain directions in the plane of membranes are taken as the material principal axes. The stresses in these principal directions are subsequently evaluated based on the total principal strains (Figure1.14) and fibrils stress–strain curve (Haut *et al.*, 1972; Morgan 1960). Equal principal strains would generate an isotropic material modulus matrix while any non-positive principal strain results in a zero (or near-zero) diagonal component in the corresponding modulus and stress matrices. Finally, these tensors are transformed back to the local membrane directions and used in subsequent manipulations (Shirazi *et al.*, 2005).

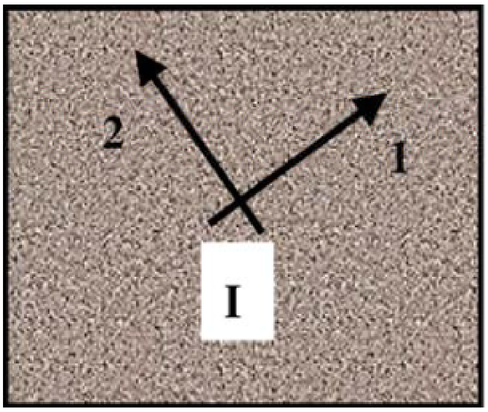

$$[E_T] = \begin{bmatrix} E_1 & 0 & 0 \\ 0 & E_2 & 0 \\ 0 & 0 & G_{12} \end{bmatrix}$$

$$G_{12} = \frac{E_1 + E_2}{4}$$

Figure 1.14 A typical shell membrane element with material principal axes that are oriented along the principal strain directions in the plane of the membrane at any given integration point I. The tangent modulus matrix in this system is also shown neglecting the cross coupling terms between incremental normal stresses and strains (i.e., $v = 0$). (Shirazi *et al.*, 2005).

For the axisymmetric models, the principal directions lie along the membrane element in the radial plane and along global circumferential direction. In the initial configuration, membrane elements can arbitrarily be oriented in any direction in the radial plane. The formulation of these membrane elements with nonlinear material properties was introduced in the ABAQUS via the subroutine. In the finite element mesh, the thickness of the entire membrane element for each solid matrix element is initially calculated based on the fibril volume fraction in that direction. This thickness is subsequently subdivided equally between two membrane elements when using solid elements with linear displacement fields, or with proportions of 2/3 for the middle element and 1/6 for the side elements when considering solid elements with quadratic displacement fields (Figure1.15 Shirazi *et al.*, 2005).

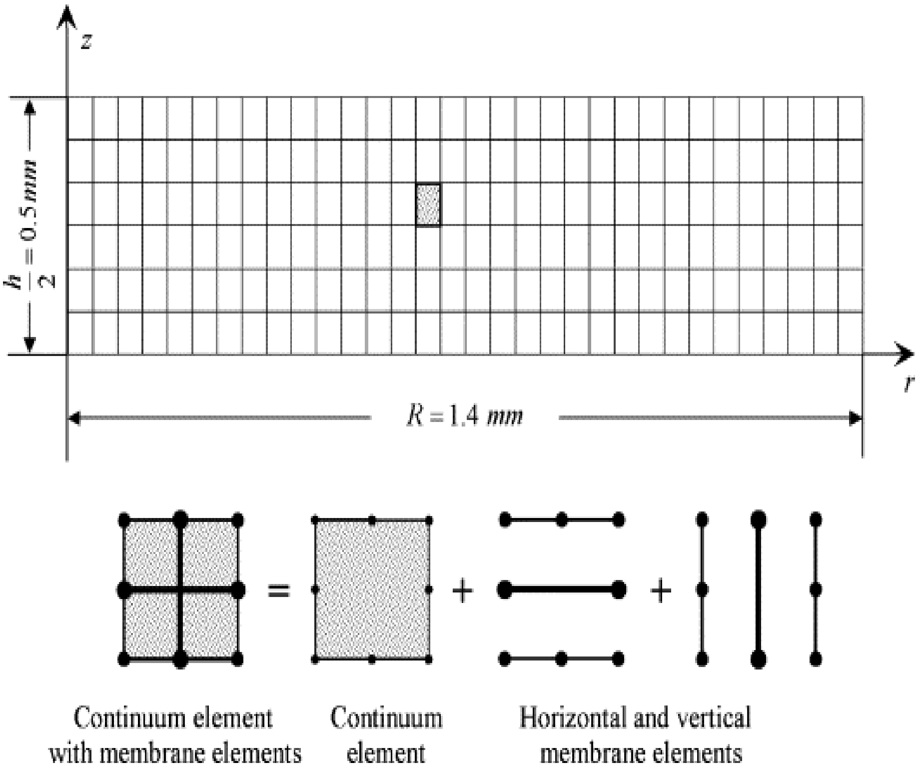

Figure 1.15 Finite element mesh of the model showing the arrangement of horizontal and vertical membrane elements in a typical axisymmetric porous continuum element (Shirazi *et al.*, 2005).

The rebar-based fibril-reinforced model

Prior fibril-reinforced models have represented fibres as 1D nonlinear spring elements (Soulhat *et al.*, 1999 and Li *et al.*,1999-2003), 2D membranes elements (Shirazi *et al.*, 2005 and 2007), and user defined embedded continuum elements (Wilson *et al.*, 2004 and Li *et al.*, 2009). Unlike all of those models, the fibrillar collagen component was introduced by Gupta *et al.* (2009) as 1D rebar elements embedded into the non-fibrillar proteoglycan matrix. Rebar elements have two geometric properties: orientation angle and cross-sectional area, both of which determine the volume fraction of fibres in the model. To model the tension-compression nonlinearity of the collagen fibres and the collapse of the fibres in compression, the individual rebar elements resisted only tensile stresses. The dimension of the cartilage surface elements was 1% of the indenter radius to ensure an accurate computation of the contact area.

1.4.3.3 Comparison of element types used in fibril-reinforced FE models

Deferent types of elements used in fibril-reinforced FE models implementing collagen fibril direction are compared and the results are displayed in Table 1.6.

Table 1.6 Comparison of different element types to implement collagen fibril direction in fibril-reinforced FE models:

Element Type	**Author**	**Model Details**				
		Definition of fibril direction	**Method to implement**	**Pros**	**Cons**	**Potentials**
1D Rebar	Gupta *et al.,* 2009	Oriented at 0^0, $\pm30^0$, $\pm60^0$ from r, z and θ axes.	Embedded element	The simplest model without subroutine.	Unrealistic fibril direction.	Define principal eigenvector as rebar element.
2D Continuum	Wilson *et al*., 2004	Arcade model*.	UMAT	3D architecture of fibrils;	Only be valid in central part of load bearing cartilage.	
3D Continuum	L. P. Li *et al*., 2009	Split-line pattern.	UMAT	Realistic orientation of collagen fibril in superficial layer.	Fibril direction in deep layers may not be same as split-line.	Split-line in deep layers; or eigenvector in whole cartilage.
3D Continuum (Brick)	Pierce *et al.,* 2010	Eigenvector of DT-MRI (corresponding to the first principal eigenvalue).	Convex strain-energy function Ψ.	Estimate fibril principal directions and dispersion directly from DT-MRI data.	The software package FEAP is not available.	Evaluate cartilage matrix integrity(in Abaqus).

* Benninghoff (1925)

1.4.3.4 Methods to define collagen fibril orientation

As mentioned in Table 1.6, various patterns were used to define collagen fibril orientation in different fibril-reinforced FE models. The detailed methods are introduced below:

Method of rebar element

In the 2D axisymmetric fibril-reinforced FE model of Gupta et al. (2009), rebar element was used to model the tension-compression nonlinearity of the randomly oriented collagen fibrils in young porcine costal cartilage. The individual rebar elements could only resist tensile stress. The random fibril distribution was mimicked through fifteen different fibril orientations: Fibrils were oriented at 0˚, ±30˚ and ±60˚ from the radial (r), axial (z) and circumferential (θ) axes - six directions in each coordinate plane and totally fifteen directions as each coordinate axis was used twice in different plane (Figure 1.16).

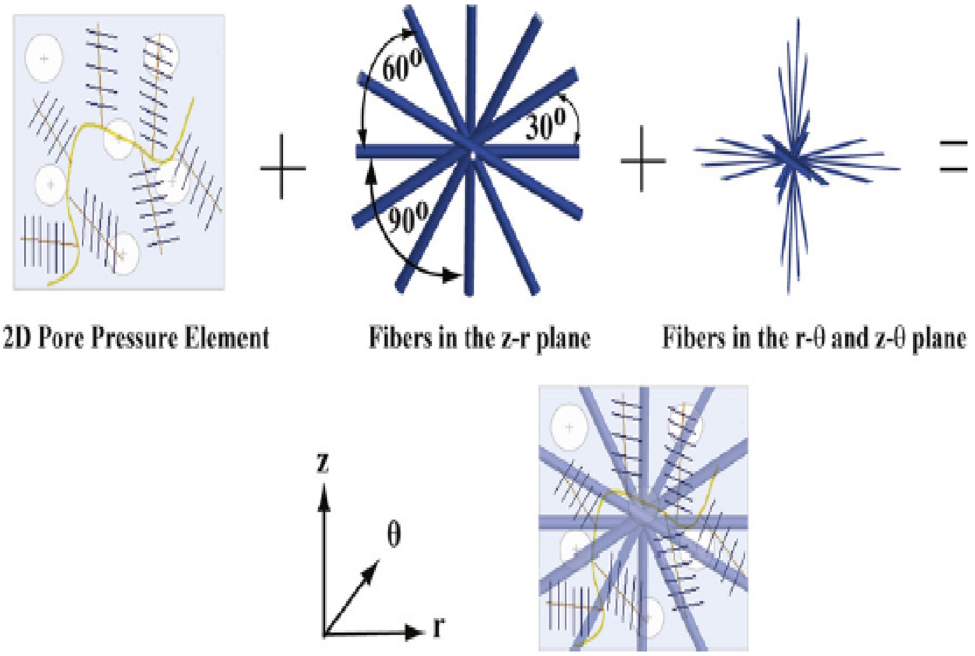

Figure 1.16 The porous, nonfibrillar matrix of cartilage is represented with 2D pore pressure elements and the randomly distributed collagen fibrils are modeled with 1D embedded rebar elements oriented in 15 different directions at 0˚, ±30˚ and ±60˚ from the r, z and θ axes (Gupta et al., 2009).

Method of arcade model

Wilson et al. (2004) implemented the orientation of both the primary and the secondary collagen fibril in their 2D axisymmetric fibril-reinforced poroviscoelastic model using continuum elements.

According to the arcade model of Benninghoff (1925), the 3D collagen network was captured as a combination of large primary collagen fibrils and smaller secondary fibrils.

The primary collagen fibril bundles extend perpendicularly from the subchondral bone, splitting up close to the articular surface into fibrils which curve to a horizontal course. Each vertical bundle was assumed to split up in four different fibril directions, curving in radial and circumferential directions (Figure 1.17).

In the deep zone, the average angle of the primary fibrils with respect to the r-axis as implemented in the FE model was 90˚. In the middle and superficial zone this angle decreased to become zero at the articular surface.

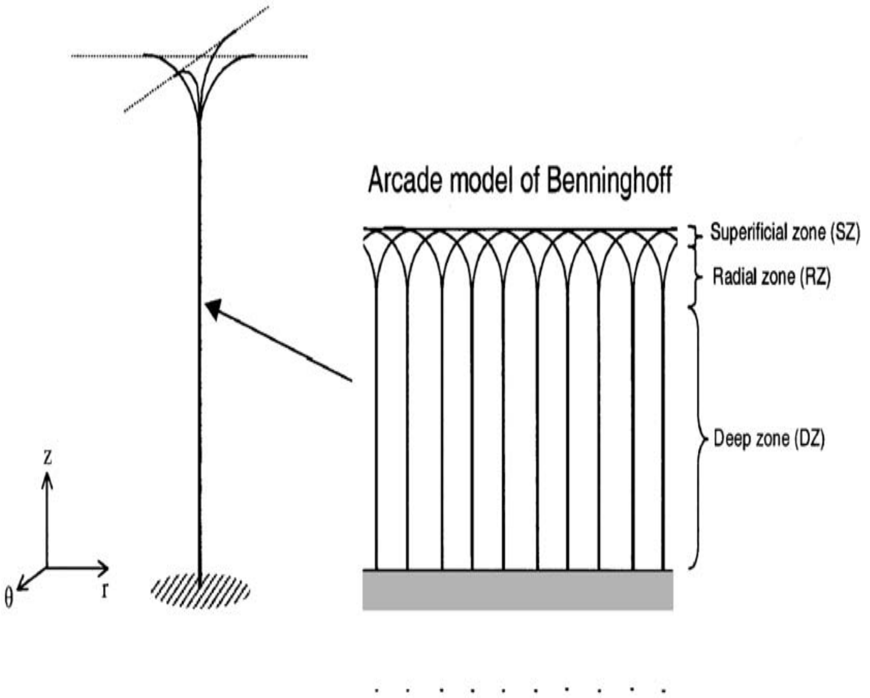

Figure 1.17 Orientation of the primary fibrils as a function of depth. Right: cartoon of the arcade model of Benninghoff (1925). Left: Orientation of four primary collagen fibrils as implemented in the model (Wilson et al., 2004).

The orientation of the secondary fibrils was assumed to be random (Benninghoff, 1925). The network of secondary fibrils was represented by a relatively homogeneous 3D network of fibrils, running in the r-, θ- and z-directions, in the bisector of the coordinate planes and in all directions with equal angles with respect to the r-, θ-and z-axis - totally 13 different orientations of the secondary fibrils at every integration point (Figure 1.18). Secondary fibrils are relatively short and provide an extra matrix stiffness in the corresponding direction.

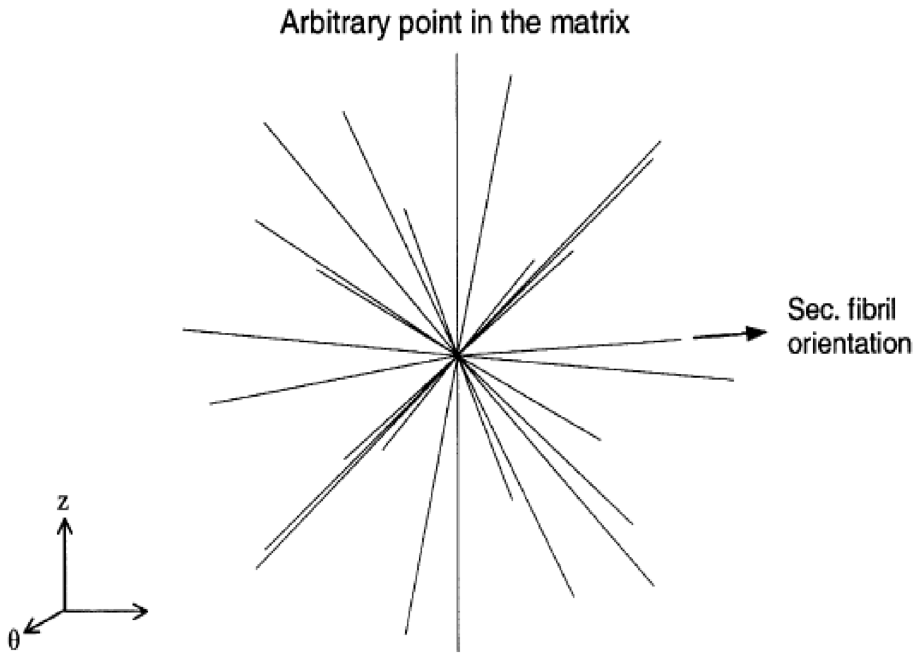

Figure 1.18 Schematic representation of the 13 different orientations of the secondary fibrils at any arbitrary point in the fibrillar matrix (Wilson et al., 2004).

Method of split-pattern

Although the two methods can implement collagen fibril orientation to the fibril reinforced models, the orientations used are idealised without detailed realistic information from experiments. The split-pattern method introduced in Section 1.3 has been used to derive the realistic fibril orientation (Figure 1.19) in Li et al. (2009).

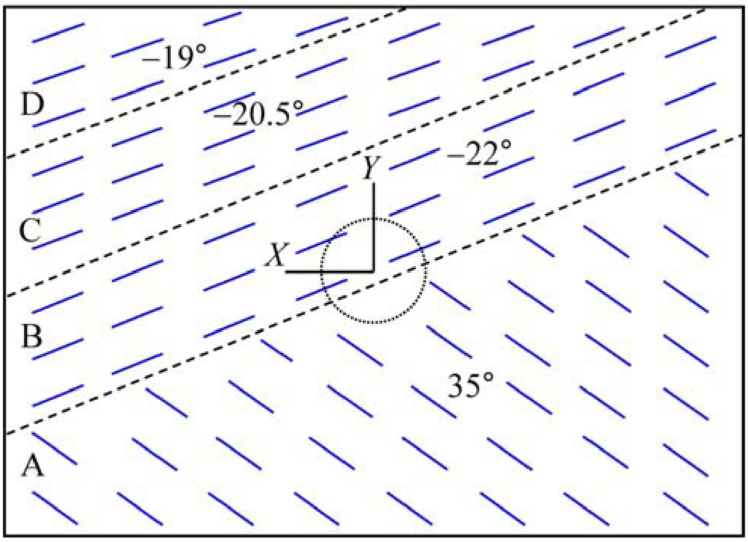

Figure 1.19 Primary collagen orientations of a piece of articular cartilage located on a distal femur. Four different fiber orientations were considered as shown with A, B, C and D zones. The size of the tissue considered is 14 × 10 × 2 mm with 2 mm in the depth (Li *et al.*, 2009).

The other method to derive realistic orientation of collagen fibril is the diffusion tensor (DT) MRI, which was also successfully employed in Pierce et al. (2010). The related information is reviewed the following section.

1.5 Diffusion Tensor Magnetic Resonance Imaging of Articular Cartilage

As stated in Table 1.6, both ‘split-line pattern’ and DT-MRI can be used to derive realistic direction of collagen fibril in AC. However, DT-MRI is the only non-invasive method to probe the underlying microstructure of AC. Although previous MRI study of arthritis was largely confined to the assessment of cartilage thickness, geometry and volume (Eckstein et al., 1995 and McGibbon et al., 2003), it does have the potential to investigating the nature of fluid dynamics in AC through its ability to distinguish between moving and stationary fluids (Callaghan et al., 1991).

1.5.1 Diffusion tensor magnetic resonance imaging (DT-MRI)

In the mid-1980s, the basic principles of DT-MRI were combined with MR imaging principles to encode molecular diffusion effects in the MR signal (Bihan et al., 1985; Merboldt et al., 1985 and Taylor et al., 1985). Molecular diffusion refers to the random translational motion of molecules resulting from the thermal energy carried by these molecules. During their random diffusion-driven displacements, molecules probe tissue structure at a microscopic scale well beyond the usual image resolution: during typical diffusion times of about 50 msec, water molecules move in articular cartilage bouncing, crossing, or interacting with many tissue components such as fibers or macromolecules (Denis et al., 2001). This made DT-MRI the only means to observe diffusion in vivo noninvasively accompanying access to both superficial and deep organs with high resolution.

Diffusion is expected to be anisotropic in the structurally aligned collagen fibrillar architecture of AC (Jeffery et al., 1991), the self-diffusion of the water molecules can therefore only be fully characterized in terms of a 3 x 3 diffusion tensor describing both the magnitude and direction of the diffusion in 3-dimensional space (Basser et al., 1994).

1.5.2 The primary collagen orientation of articular cartilage

Meder et al. (2006) and Filidoro et al. (2005) suggested that the principal eigenvectors (corresponding to the maximum eigenvalue) of the water diffusion tensor follow the collagen fibre directions: On the timescale of the DT-MRI measurements, water molecules diffuse over distances of a few microns (Meder et al., 2006), which is much larger than the diameter (~ 40 nm) of the collagen fibrils themselves (Langsjo et al., 1995). Consequently the diffusion of water in cartilage is restricted by the presence of the collagen fibre bundles. This restriction is greatest in a direction normal to the fibres, leading to a lower diffusivity in this direction and a correspondingly higher diffusivity parallel to the direction of the local fibre orientation.

The principal eigenvector can be represented by a “quiver” plot, where each quiver represents the projection of the principal diffusion eigenvector on to the image plane. For each pixel of the DT-MRI grid, the principal eigenvector was projected to one of the global planes. Then all of the projections in the same plane were attached on the bottom of the corresponding pixel to create the 2D quiver plot. The 2D quiver plot of the collagen fibril derived by Meder et al. (2006) is displayed in Figure 1.20.

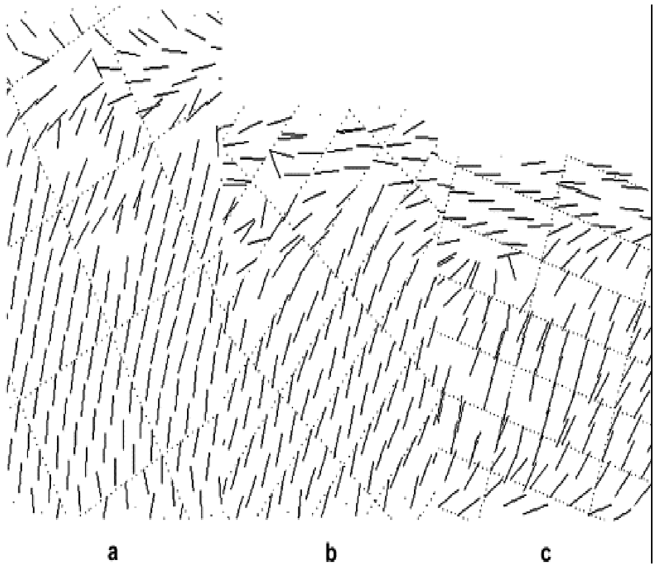

Figure 1.20 2D quiver plots of the collagen fibril, (a) before compression and after two subsequent compressions (b) by 18% and (c) by 29% of the original cartilage thickness, respectively (Meder et al. 2006).

The collagen fibril alignment angles of bovine articular cartilage obtained from diffusion-tensor imaging (DTI) were compared with those from polarized light microscopy (PLM) by Visser et al. (2008). For the five samples studied, the shapes of the depth profiles of the PLM and DTI alignment angles were qualitatively similar. This result supports the use of DTI for the quantitative measurement of collagen fibril alignment in cartilage.

Recently, Pierce *et al*. (2010) derived 3D quiver plots of cartilage collagen fibrils which seems more realistic (Figure 1.21) and implemented them to the related fibril reinforced model.

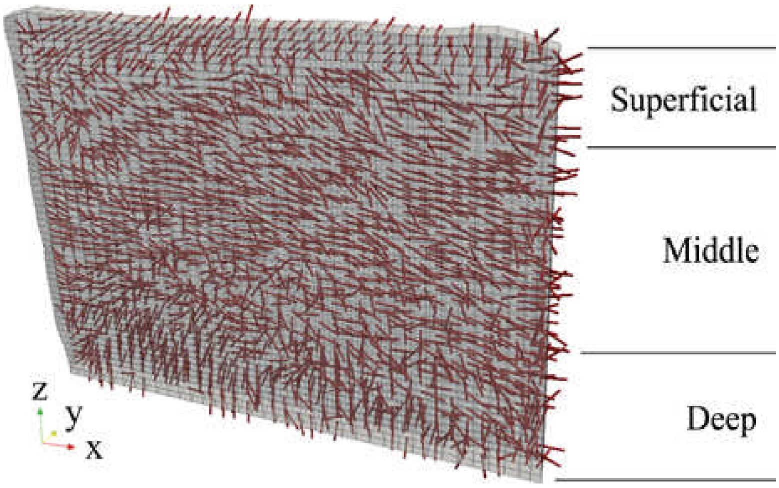

Figure 1.21 3D quiver plots of the cartilage collagen fibril (Pierce *et al*., 2010).

However, DT-MRI measurements in the deep zone of cartilage were difficult to realize due to the low water content and the signal presented was very low (Pierce et al., 2010). This may lead to the shortage of diffusion tensor measurements in the deepest part of the cartilage sample. Due to the image noise, the length of the MRI pixel grids may also be shorter than the sample.

1.6 Summary of the literature review

In order to gain better understanding of fundamental lubrication mechanism of articular cartilage, the related literature on cartilage biomechanics and lubrication were reviewed, followed by the review of the related computational models and the brief introduction on DT-MRI.

Implementing the realistic collagen fibril orientation derived from DT-MRI data, the fibril-reinforced model of Pierce et al. (2012) is the most realistic, comparing to the others with idealized (Gupta et al., 2009) or simplified fibril orientation (Li et al., 2009 and Rasanen et al., 2012). However, the model in Pierce et al. (2012) did not include viscous effects in both the solid matrix and the fibril. In order to set up the more realistic fibril-reinforced model, it is necessary to employ the material model of Li et al., 2009 and implement the collagen fibril orientation defined by DT-MRI data as Pierce et al. (2012) did.

1.7 Project Aims and Objectives

Rationale:

The effect of composition and structure of articular cartilage, particularly the realistic collagen fibril orientation, on fluid load support have not been investigated in details. This provides an ideal opportunity to develop the computational models incorporating FE analysis and DT-MRI data to present a better understanding of fundamental lubrication mechanism of articular cartilage.

Aims:

The aim of this project is to develop more realistic fibril-reinforced computational models that incorporate FE analysis and DT-MRI data, with the better interpretation of interstitial fluid pressure and load support in cartilage.

Objectives:

1) To set up an isotropic poroelastic FE model to predict fluid load support in cartilage.
2) To provide the more detailed analysis of the collagen fibril orientation defined by the principal eigenvector of diffusion tensor, in contrast to the literature, and verify the rationality of the definition.
3) To develop the method to implement DT-MRI data in the fibril-reinforced models.
4) To set up the 2D fibril-reinforced poroelastic models implementing DT-MRI data and “user material” option in ABAQUS to overcome the limitation of previous models; compare the results with (1).
5) To extend the 2D fibril-reinforced model to 3D one to predict fluid load support in articular cartilage.
6) To simulate the model with experimental results using the 3D model, and validate the feasibility and reliability of the methodologies to implement the DT-MRI data to the fibril-reinforced models.

Chapter 2 Analysis of Diffusion Tensor Magnetic Imaging Data

2.1 Introduction

In articular cartilage, water molecules diffuse over distances of a few microns which are much larger than the diameter (~ 40nm) of the collagen fibrils (Langsjo et al., 1995). Consequently the diffusion of water in cartilage is restricted by the presence of the collagen fibre bundles. This restriction is greatest in a direction normal to the fibres, leading to a lower diffusivity in this direction and a correspondingly higher diffusivity parallel to the direction of the local fibre orientation (Meder et al., 2006 and Filidoro et al., 2005).

High resolution DT-MRI provides the detailed information of water and water flow (Visser et al., 2008), as well as the composition and structure of articular cartilage. Once a DT is derived in terms of a 3 x 3 matrix for each pixel grid of MRI, its eigenvalues and the corresponding eigenvectors can be calculated by diagonalizing the matrix. The eigenvectors are independent of the scanner coordinates, representing the three principal directions of this DT and their magnitudes within the tissue. The principal eigenvector corresponding to the maximum eigenvalue of a DT follows the direction of the collagen fibril within the corresponding MRI pixel grid (Meder et al., 2006 and Filidoro et al., 2005).

In order to verify the rationality of the DT-MRI data to represent the collagen fibril orientation in articular cartilage, their relationship is introduced first in this chapter; and the methods to analyze the DT-MRI data, the results of the analysis and the discussion of the results are also described. The information on the direction of the fibres was then used in Chapter 3 to determine the material model.

The first section of the chapter introduces the definition of the orientation of the collagen fibril using DT-MRI results, together with the two kinds of method to analyze the DT-MRI data. The detailed analysis results of the DT-MRI data is presented in the second section. The last section discusses the DT-MRI results and verifies its consistency with the literature. The rationality to implement the DT-MRI data to the FE models representing the collagen fibril orientation is also verified in the mean time.

2.2 Method to Analyze the DT-MRI Data

2.2.1 Material

A high resolution 9.4T DT-MRI was performed by Dr Robin Damion (School of physics, University of Leeds), on the cross-section of a cylindrical articular cartilage specimen (through the symmetric axis) with 6.0 mm diameter and 1.36 mm thickness (Fermor et al., 2013; Figure 2.1). Specimens were collected from the patellofemoral grooves of an 18 month old bovine knee joints (stored frozen in Ringer’s solution and used within a month of collection).

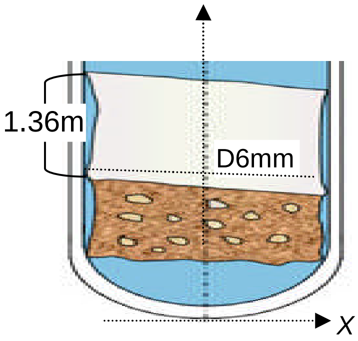

Figure 2.1 Schematic diagram of cartilage specimen scanned using MRI. The Y-axis was defined as into page perpendicular to the X and Z axes (Modified from Pierce *et al*., 2010).

2.2.2 The Diffusion Tensor MRI scanning and pixel definitions

The MRI image resulting from the scan of the articular cartilage was a two-dimensional image consisting of 17 rows and 74 columns. Both the vertical and the horizontal resolutions were 70µm. As part of the DT-MRI process, a diffusion tensor was derived for each pixel within the image. Please note the dimension of the pixel grid did not exactly match the geometry of the cartilage sample in Figure 2.1 due to the limitation of the DT-MRI (See Chapter 1, Section 1.5): the thickness and length of the pixel grid was 1.19 (17 × 0.07) mm and 5.18 (74 × 0.07) mm respectively i.e. no diffusion tensor was derived corresponding to the deepest and side part of cartilage.

The principal eigenvectors (unit vectors) of DT were calculated and presented as components along three global axes i.e. X_{ij} , Y_{ij} and Z_{ij} ($X_{ij}{}^2 + Y_{ij}{}^2 + Z_{ij}{}^2 = 1$) where i = 1⋯17 from top to bottom of the pixel grid and j = 1⋯74 from left to right respectively.

2.2.3 Method for analysing the principal eigenvectors

The DT-MRI data particularly the principal eigenvectors were analysed through two steps using different method: the direct observation of 2D quiver plot and the quantitative analysis by calculating the angle between the principal eigenvector and the *X-Y* plane parallel to the cartilage surface in each pixel of MRI.

2.2.3.1 The 2D quiver plots

The first step of analysing the principal eigenvectors was to look for the distribution of collagen fibril visually through direct observation of the 2D quiver plots of eigenvector components on the global coordinate planes (totally three plots). The 2D quiver plot was made of the projection of the principal eigenvectors: for each pixel of the DT-MRI grids, the principal eigenvector was projected to one of the global planes. Then all of the vector components in the same plane were attached on the bottom of the corresponding pixel to create the 2D quiver plot.

These plots allow qualitative analysis of the distribution of collagen fibril. For the convenience of interpretation, the quiver plot in the *X-Z* plane was selected. The length of the quiver, i.e. $\sqrt{X_{ij}^2 + Z_{ij}^2}$, has an important hint: its increase means the decrease of Y_{ij} and indicates the decrease of the angle between the quiver and the *X-Z* plane. So the long quiver (tends to be 1) in the *X-Z* plane means the corresponding principal eigenvectors nearly parallel to the *X-Z* plane; hence the direction of the long quiver can nearly represent the angle between the corresponding eigenvector and the cartilage surface which parallel to the *X-Y* plane. However, the short quivers can only partly show the angle between the principal eigenvectors and the cartilage surface. To solve this problem, the exact value of the angle between the principal eigenvector and the cartilage surface should be calculated for each pixel of MRI.

2.2.3.2 Analysis of the angles between the principal eigenvectors and the cartilage surface

The second step of analysing the principal eigenvectors was to study the distribution of the fibril by calculating the angles β_{ij} (0°≤ β_{ij}≤ 90°; i and j represents the row and column number of the corresponding pixel respectively) between the principal eigenvectors and the *X*-*Y* plane parallel to the cartilage surface. β_{ij} was defined as:

$$\beta_{ij} = \tan^{-1}\left| Z_{ij}/\sqrt{{X_{ij}}^2 + {Y_{ij}}^2} \right| \quad \ldots\ldots\ldots\ldots\ldots\ldots\ldots \text{(2.1)}$$

where X_{ij} , Y_{ij} and Z_{ij} are the components of the corresponding principal eigenvector on the three global axes respectively.

The angle β_{ij} is extremely important in modelling cartilage particularly in the surface zone, as it directly affects the horizontal component value of the fibril tensile stress on the corresponding site of cartilage. As introduced in Section 1.4.2.2, the horizontal tensile stress can prevent lateral expansion of cartilage and enhance the pressurization of interstitial fluid to support the applied load.

The fibril angles in the same row were gathered in one bar chart to observe the layered distribution of collage fibril in the tissue and compared with the quiver plot, totally 17 bar charts were produced.

Then the percentage occupied by every 10 degree of fibril angle in the same layer was calculated and displayed by the x-y scatter (each interregional represented by the upper limit). Then the scatters with similar trend were put together to find out the layered fibril angle distribution quantitatively.

2.3 Results

2.3.1 Two-dimensional quiver plots

A two-dimensional quiver plot in the X-Z plane of the principal eigenvectors of the whole cartilage sample cross-section is shown in Figure 2.2 (provided by Dr Robin Damion), with the row and column numbers displayed on the vertical and horizontal axis respectively.

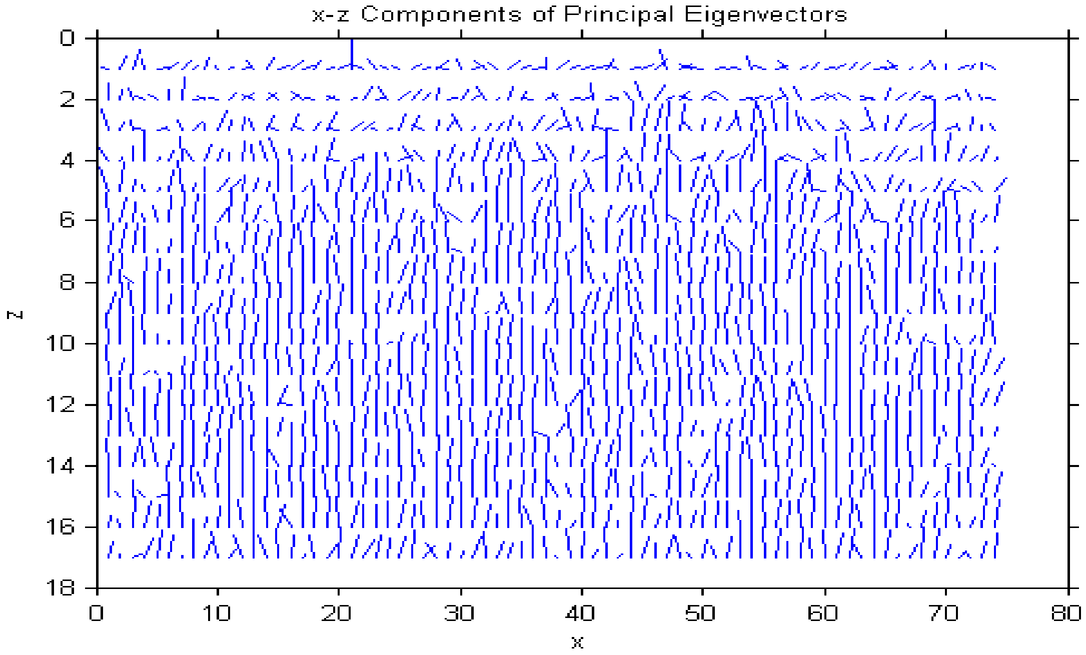

Figure 2.2 *X-Z* components of principal eigenvector of diffusion tensor. (*Z* axis shows the row number, and *X* axis shows the column number of the pixel grid; provided by Dr Robin Damion)

In Figure 2.2, most fibril components in the top 2 layers (0.14 mm thick) of the pixel grids which occupied 10.0% of cartilage sample thickness tended to be horizontal. In the next seven layers (the 3rd - 9th layer) occupying 36.0% of cartilage thickness, fibril components showed various gradients and no single gradient was found to be dominant, i.e. fibrils distributed randomly. In the remaining layers (the 10th-17th layer) occupying 41.2% of cartilage thickness, most fibril components were or tended to be vertical (except in the 17th layer). This will be discussed in Section 2.4.

2.3.2 Distribution of fibril angles to cartilage surface

2.3.2.1 Fibril angles in the top two layers

In the top two layers of pixel grids corresponding to the surface zone of cartilage, few fibrils had angles greater than 30° (Figure 2.3).

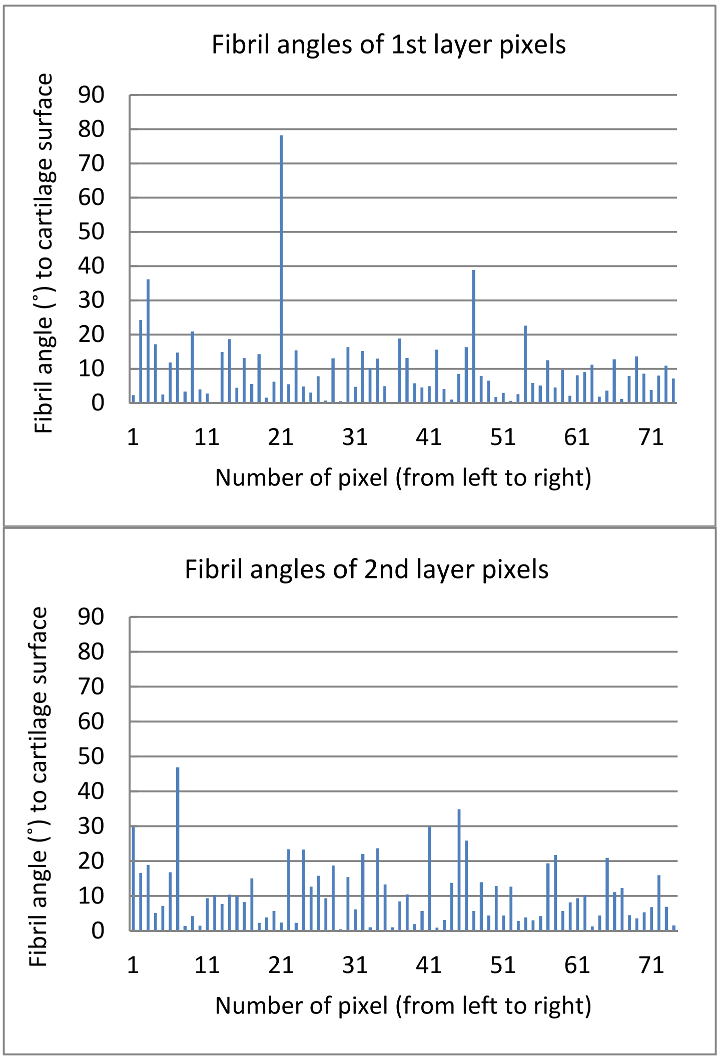

Figure 2.3 Bar chart of fibril angle of pixels in the top 2 layers of cartilage.

The more important result was that the majority of fibril angles were less than 20° (Figure 2.3). The percentage of the fibril angles were smaller than 10° was 62.2% in the first layer and 56.8% in the second layer. The percentage less than 20° was 91.9% in the first layer and 85.1% in the second layer respectively (Figure 2.4). Meanwhile, only a few fibril angles were greater than 30°. This means most collagen fibrils in the first two layers from the cartilage surface tended to be horizontal.

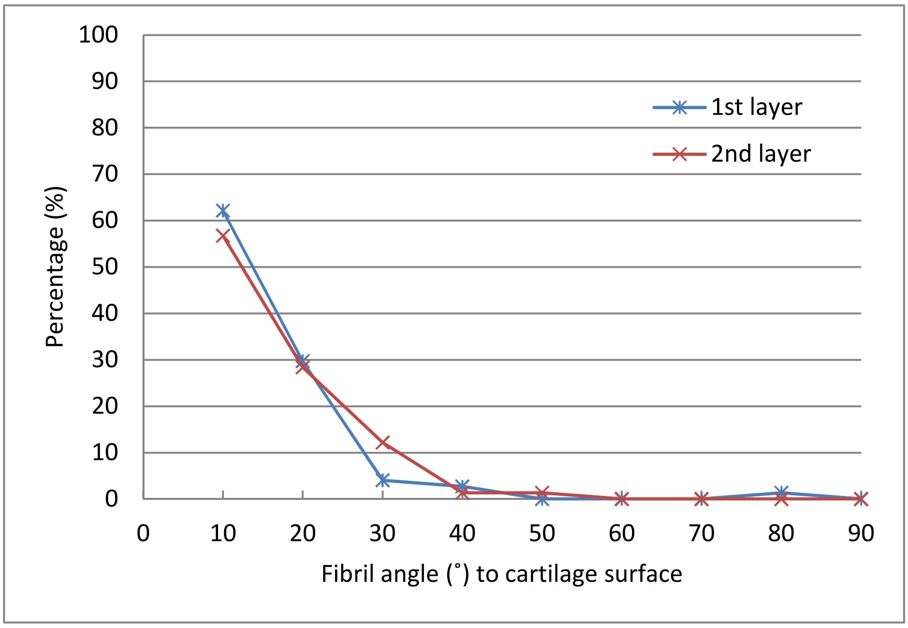

Figure 2.4 Fibril angle distribution of pixels in top 2 layers from cartilage surface.

2.3.2.2 Fibril angles in layers from the 3rd to 9th

Fibril angles in the 3rd and 4th layer

Most of the fibril angles in the 3rd and 4th layer of pixel grids were less than 30° (Figure 2.5), 74.3% and 68.9% respectively (Figure 2.6).

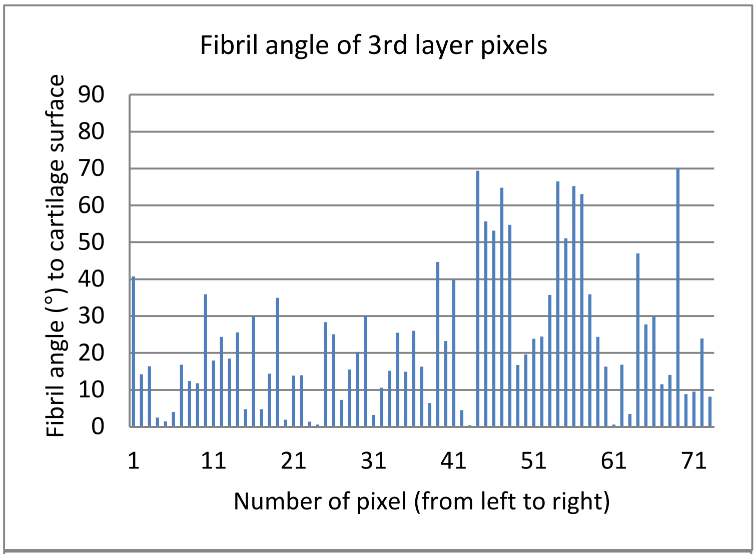

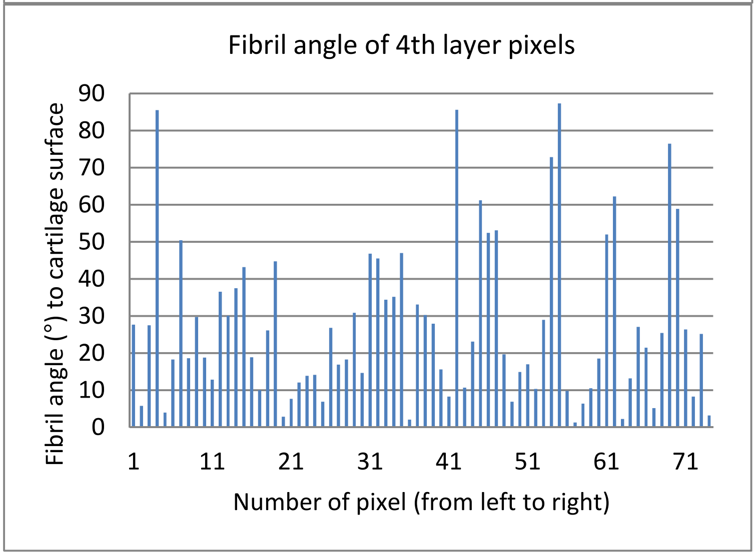

Figure 2.5 Bar chart of fibril angle of pixels in the 3rd and 4th layer of cartilage.

It seemed feasible to classify the two layers belonging to the surface zone of the cartilage. But only 24.3% of the fibril angles were smaller than 10° in the 3rd layer and 23.0% in the 4th layer (Figure 2.6). Meanwhile, a number of angles were greater than 40° (Figure 2.5 and 2.6). So it was more reasonable for the two layers to be included in the middle zone of the cartilage.

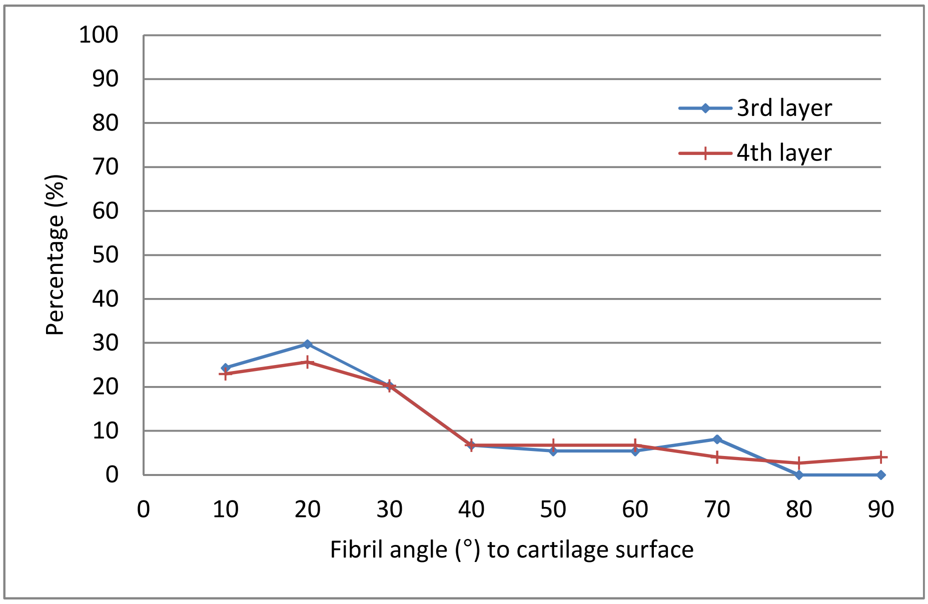

Figure 2.6 Fibril angle distribution of pixels in the 3rd and 4th layer from cartilage surface.

Fibril angles in the layers from the 5th to 9th

In the next five layers of pixel grids from the cartilage surface, the 5th to 9th layer, collagen fibrils did not have a dominant orientation i.e. they distributed randomly (Figure 2.7).

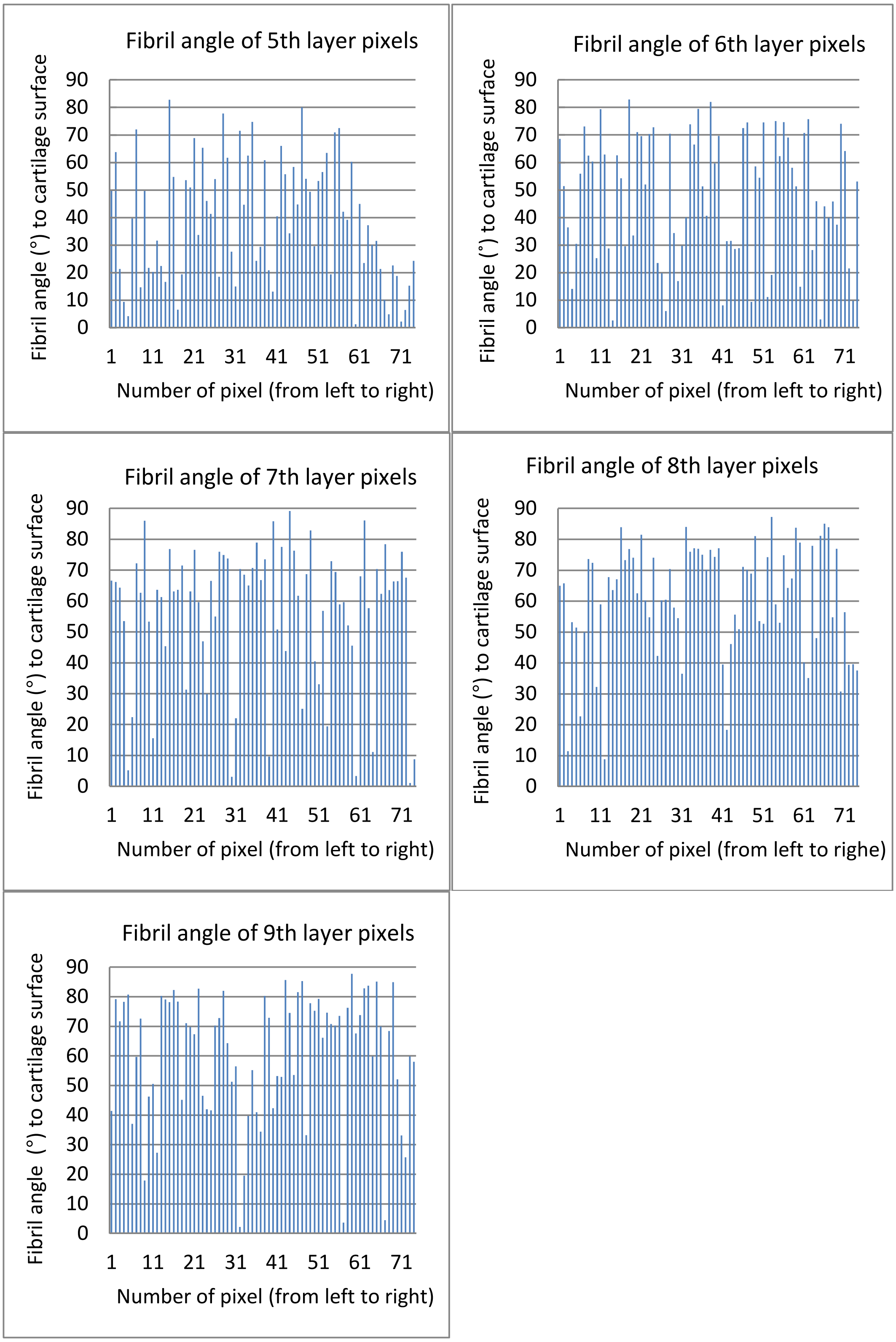

Figure 2.7 Bar chart of fibril angle of pixels in the 5th - 9th layer from cartilage surface.

In each of the layers from the 5th to the 9th, the percentage occupied by each interregional (10°) of fibril angle was less than 30%; and the total percentage occupied by fibril angles ≥ 60° (the sum of the values of the last three points of each individual curve) was less than 60% (Figure 2.8). This result confirmed the conclusion drawn from the angle bar charts in Figure 2.7 that the collagen fibrils distributed randomly. So all of the five layers should be included in the middle zone of the cartilage.

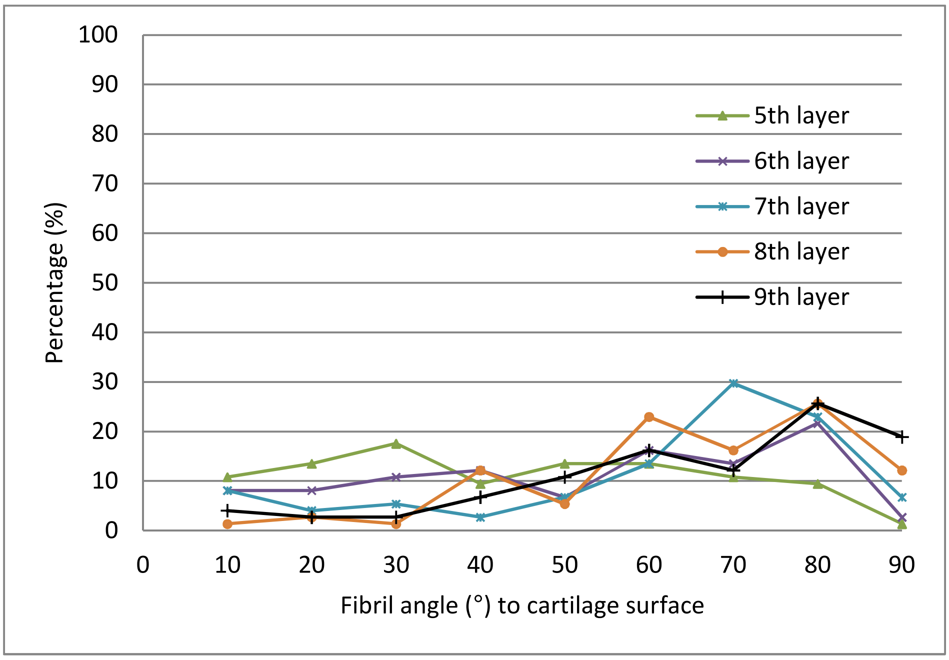

Figure 2.8 Fibril angle distribution of pixels in the 5th - 9th layer from cartilage surface.

2.3.2.3 Fibril angles in layers from the 10th to 17th

Fibril angles in the layers from the 10th to 15th

In the layers from the 10th to the 15th of pixel grids corresponding to part of the cartilage deep zone, lots of the percentage occupied by these fibril angles ≥ 70° in most layers was greater than 60% (except 58.1% in the 15th layer; Figure 2.9); and the amount of the fibrils with angle greater than 60° increased apparently in comparison to the higher layers (Figure 2.10). This result clearly showed most collagen fibrils in these layers tended to be vertical, although several angles were less than 40° even less than 10° (Figures 2.9 and 2.10).

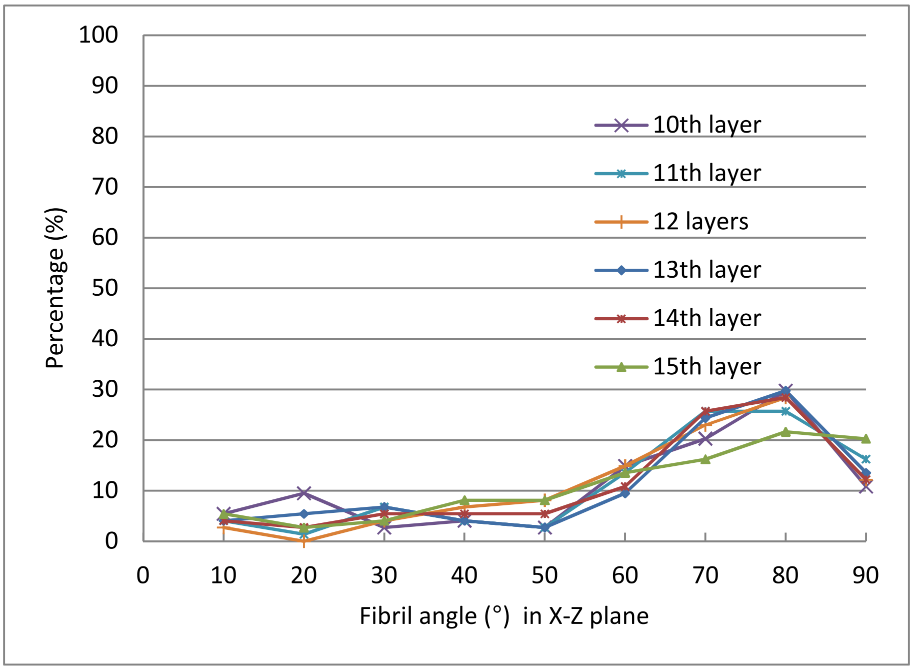

Figure 2.9 Fibril angle distribution of elements in 10^{th} - 15^{th} layer from cartilage surface.

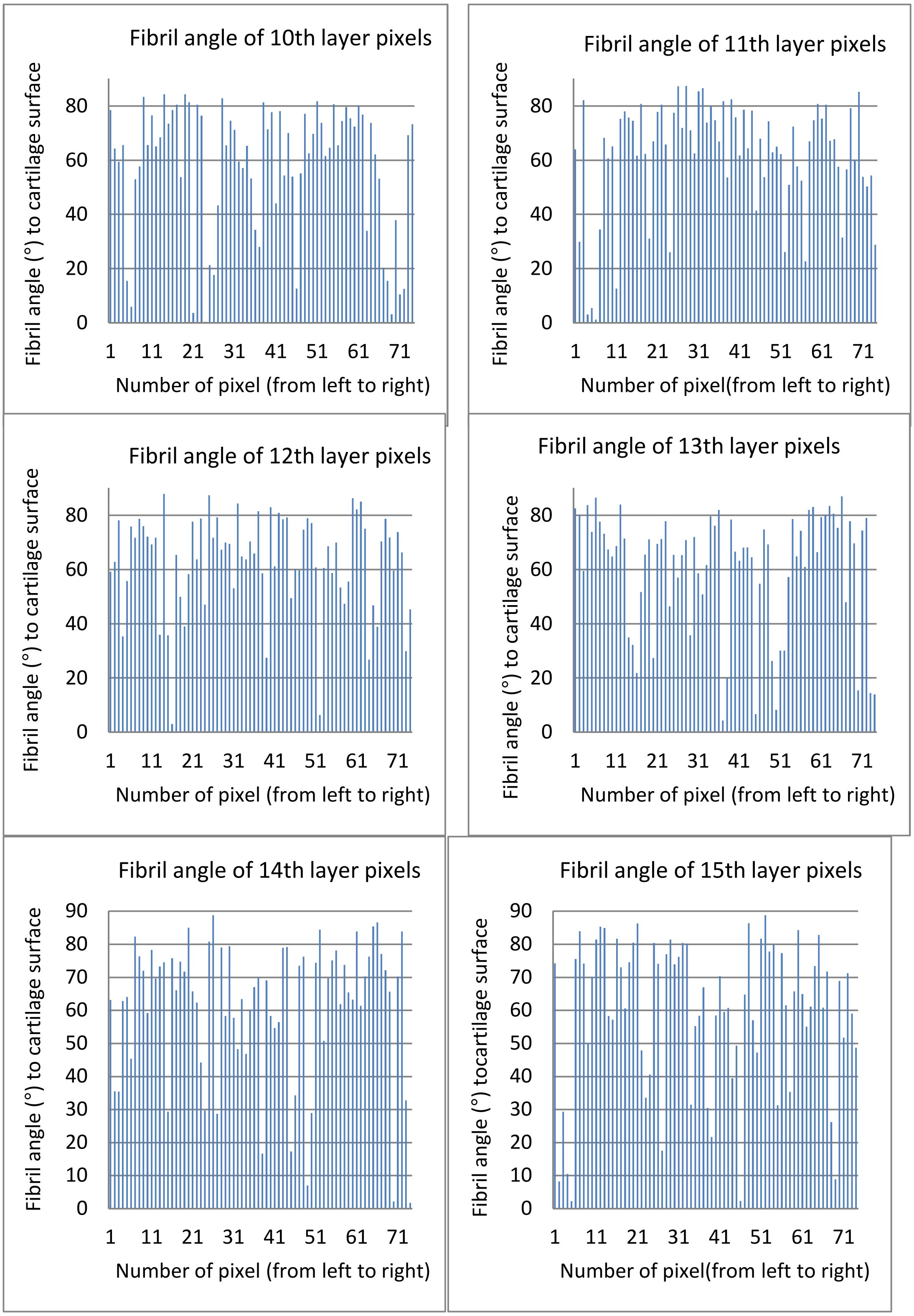

Figure 2.10 Bar chart of fibril angle of pixels in the 10th - 15th layer from cartilage surface.

Fibril angles in the 16th and 17th layer

As a part of the deep zone, the fibril distribution seemed to be random in the 16th and 17th layer particularly in the 17th layer (Figure 2.11 and 2.12). The reason led to the phenomenon is discussed in the following section.

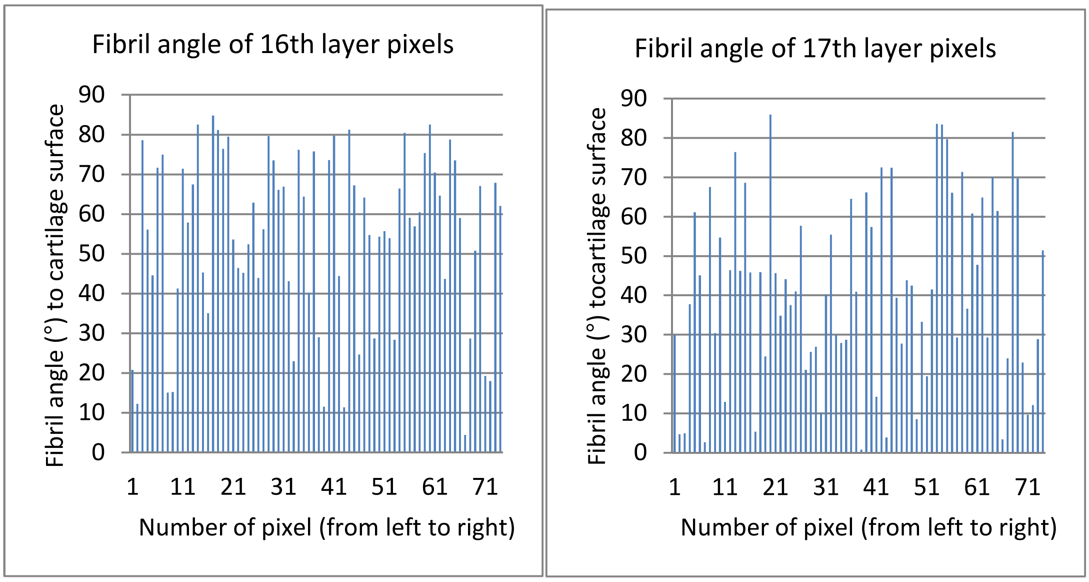

Figure 2.11 Bar chart of fibril angle of pixels in the 16th and 17th layer from cartilage surface.

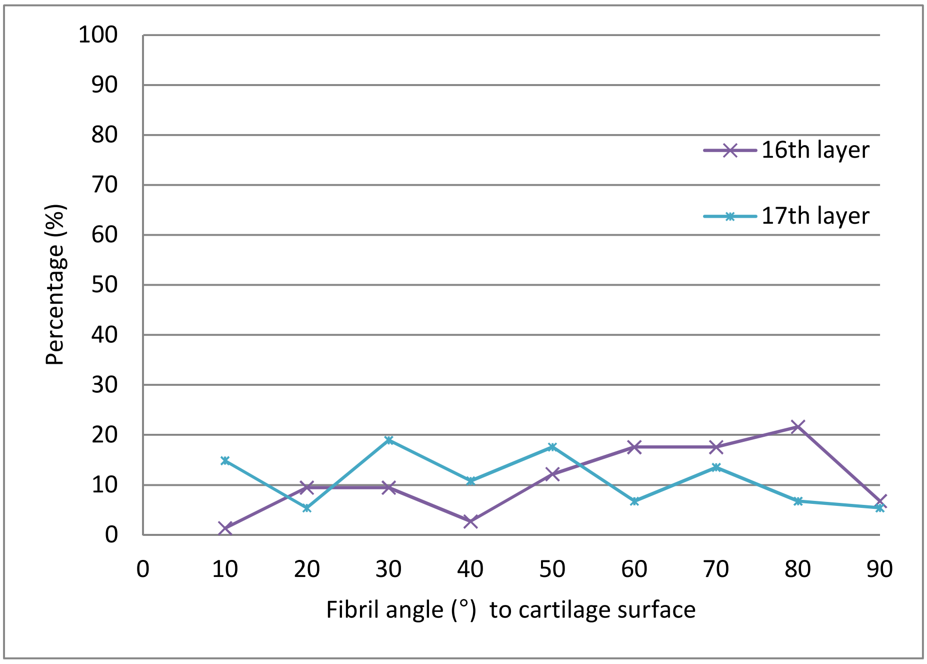

Figure 2.13 Fibril angle distribution of elements in 16^{th} and 17^{th} layer from cartilage surface.

2.4 Discussion

The orientation of collagen fibril was defined by the principal eigenvector of the DT and projected visually on the plane of cartilage cross-section (X-Z coordinates plane) as shown in Figure 2.2. The distribution of collagen fibril in articular cartilage was largely consistent with the literature particularly the results of Visser et al. (2008) which was also derived from DT-MRI data (Figure 1.20a).

In the top two layers, most of the angles between the principal eigenvectors and the planes parallel to the cartilage surface are less than 20° (Figure 2.4). This result and the angle distribution in the deep zone of cartilage (Figure 2.9-2.10) were in agreement with Meder et al. (2006), which found “the principal component of the diffusion tensor appears to be at around 75° to the normal near the articular surface, while in the deep zone it appears to be at approximately 20° to the normal.”. This confirms the direct observation of Figure 2.2 in Section 2.3.2. The most important finding is that: these results verified the rationality to implement the principal eigenvectors of DT in the computational models representing the fibril orientation.

In the deepest area of cartilage (the eight layers in Figures 2.9 - 2.13), there are a limited number of angles that were less than 40° (even than 10°) which seems not consistent with the predominant view in the literature considering all of the collagen fibrils perpendicular to the cartilage surface (Mow et al., 1992). But Kaab et al. (1998) also had the similar finding as introduced in Section 1.3: some fibrils run obliquely in the deep zone while the majority collage columns are perpendicular to the cartilage surface (Figure 1.7b).

However, DT-MRI measurements in the deep zone of cartilage were difficult to realize due to the low water content and the signal presented was very low (Pierce et al., 2010). This led to the shortage of diffusion tensor measurements in the deepest part of the cartilage sample in Figure 2.1, so the thickness of the MRI pixel grids in Figure 2.2 was 0.17mm less compared to the sample. The length of the MRI pixel grids was shorter because of the image noise.

Visser et al. (2008b) explained the phenomenon that several angles are greater than 50° in the top two layers: Fibres are disordered within a given DTI pixel of a length scale of 10 μm and a particular water molecule can access a range of fibre orientations on the timescale of a DTI measurement. This resulted in the measured DT behaving as weighted average quantities.

But this limitation does not affect the fibril angles defined by the DT in other pixels and the whole distribution of collage fibril in the specific layer.

As reviewed in Section 1.4 and 1.5, Pierce et al. (2010) had also derived the orientation of collagen fibrils in bovine groove cartilage from DT-MRI data and successfully implemented the fibril direction to their finite element model. Different from the 2D quiver plot in this chapter, the 3D quiver plot was used to display the fibril orientation.

From the theoretical mechanism to the clinical application and the practice of computational modeling, the feasibility and rationality of the DT-MRI have been fully proved. So the principal eigenvector will be defined as primary collagen orientation and implemented to the 2D and 3D fibril-reinforced FE models in the following chapters.

Chapter 3 Material Model and Method to Implement DT-MRI Data

3.1 Introduction

This chapter describes the material model of cartilage employed in the finite element analysis within this thesis, including how information from the DT-MRI data (described in Section 2.2) was used to create local material property variations which reflect the direct of reinforcing fibrils. As this work includes both 2D axisymmetric and 3D models, the specific implementation for each of those element types is described. This chapter is concerned primarily with the Young's modulus values assigned to the solid phase of the cartilage and does not discuss any fluid behavior. In all cases it was assumed that the cartilage solid phase is composed of a linear elastic matrix and distribution of viscoelastic fibrils. Each of which has an individual orientation. In order to include the effect of the fibrillar component it is necessary to include a fibril direction for each element and a function to calculate the viscoelastic property change as strain increases.

Section 3.2 gives the equations used to define the strain-dependent fibrillar Young's modulus. The time discretization scheme is shown, along with simplifications which can be made when the instantaneous fibrillar modulus was used. The material model derived here was implemented into a FORTRAN subroutine, for using with ABAQUS, by Li et al (2009) which was used in this thesis.

Sections 3.3 and 3.4 describe the implementation of the collagen fibril direction in the 2D and 3D finite element models respectively. Details are given of the commands used to import the primary fibril orientation information (described in Chapter 2) and convert it into a local coordinate system for each element in the model.

3.2 Material Model

In the fibril-reinforced FE models of this thesis, the material properties for each element were modified based on the primary fibril orientation in that area, using ‘‘user material” option i.e. ‘‘UMAT” in ABAQUS (Dassault Systemes, Suresnes Cedex, France) - the FORTRAN written subroutine (Li *et al.*, 2009) was kindly provided by Dr L. P. Li, Calgary University of Canada.

Articular cartilage can be considered as a porous matrix saturated in water, reinforced by the fibrillar network. The porous matrix was nonfibrillar, representing the solid matrix excluding the collagen fibers. The nonfibrillar matrix was modeled as a continuous linearly elastic material, with the Young’s modulus E_m, and Poisson’s ratio v_m. These basic properties were augmented with representation of the fibrillar network, which was modeled as nonlinearly viscoelastic, direction and location dependent properties. ‘Using $\vec{x}$ to represent a fiber direction at a location with Cartesian coordinates (*X, Y, Z*), the fibrillar modulus in the direction of $\vec{x}$ is a function of the tensile strain in the direction, $E_x^{\mathrm{f}}(\varepsilon_x)$, as well as a function of $\vec{x}$ and (*X, Y, Z*) (anisotropic and inhomogeneous). The fibrillar modulus was taken to be zero for compressive strains. … Shear stress between parallel fibers was neglected, but shearing was modeled in the nonfibrillar porous matrix.’ (Li *et al.* 2009).

3.2.1 The Jacobian matrix of fibril-reinforced FE model

Jacobian matrix, defined as: $[D] = \partial\Delta\sigma/\partial\Delta\varepsilon$ was required to implement material properties in the fibril-reinforced FE models, where $\partial\Delta\sigma$ are the stress increments and $\partial\Delta\varepsilon$ are the strain increments. This was achieved by using ‘‘UMAT” available in ABAQUS (Abaqus User Subroutines Reference Manual 1.1.36 “UMAT”). As only small deformation problems were solved, the Jacobian matrix for the fibril-reinforced model of AC was:

$$[\mathrm{D}] = \begin{bmatrix} D_{xx} & \lambda & \lambda & 0 & 0 & 0 \\ \lambda & D_{yy} & \lambda & 0 & 0 & 0 \\ \lambda & \lambda & D_{zz} & 0 & 0 & 0 \\ 0 & 0 & 0 & \mu & 0 & 0 \\ 0 & 0 & 0 & 0 & \mu & 0 \\ 0 & 0 & 0 & 0 & 0 & \mu \end{bmatrix} \tag{3.1}$$

where λ and μ are the Lamé constants of the nonfibrillar matrix.

According to the biphasic theory, the stress of the fibril-reinforced material is the sum of the matrix and fibril stresses. The nonfibrillar matrix was isotropic with linearly elastic property, hence

$$D_{xx} = \lambda + 2\mu + \partial\Delta\sigma_x^{\mathrm{f}}/\partial\Delta\varepsilon_x^{\mathrm{f}} \tag{3.2}$$

here $\partial\Delta\sigma_x^{\mathrm{f}}/\partial\Delta\varepsilon_x^{\mathrm{f}}$ represents the contribution of the fibrillar matrix to the Jacobian and will be derived in the following section.

3.2.2 The contribution of the fibrillar matrix to the Jacobian

In order to define $\partial\Delta\sigma_x^{\mathrm{f}}/\partial\Delta\varepsilon_x^{\mathrm{f}}$ -- the contribution of the fibrillar matrix to the Jacobian, $\sigma_x^{\mathrm{f}}(t)$ - the tensile stress of collagen fiber in articular cartilage should be calculated. According to Equation 1.2 in Section 1.4.3.1, $\sigma_x^{\mathrm{f}}(t)$ was determined by the hereditary integral:

$$\sigma_x^{\mathrm{f}}(t) = \sigma_x^{\mathrm{f}}(0) + \int_0^t G_x(t-\tau)E_x^{\mathrm{f}}(\varepsilon_x)\dot{\varepsilon}_x \, d\tau \qquad (3.3)$$

where $\dot{\varepsilon}_x = \varDelta\varepsilon_x/\varDelta t = [\varepsilon_x(t+\varDelta t) - \varepsilon_x(t)]/\varDelta t$ denoting the rate of strain changing with time. The relaxation function $G_x(t)$ of the fibrillar matrix was an alteration of Equation 1.3 (Li *et al.*, 2009):

$$G_x(t) = 1 + \sum_m g_m \exp(-t/\lambda_m) \qquad (3.4)$$

in which λ_m are characteristic times for the viscoelastic dissipation and g_m are dimensionless constants representing the discrete moduli (Suh *et al.*, 1998).

From Equation 3.3 and 3.4, the contribution of the fibrillar matrix to the Jacobian was derived as:

$$\partial\Delta\sigma_x^{\mathrm{f}}/\partial\Delta\varepsilon_x^{\mathrm{f}} \approx G_x(\Delta t)E_x^{\mathrm{f}}(\varepsilon_x) \tag{3.5}$$

The detailed derivation of Equation 3.5 can be found in Appendix B.

3.2.3 Simplification for the instantaneous fibrillar modulus

Li et al. (2009) modeled the fluid-flow dependent viscoelasticity of cartilage using the soil consolidation procedure in ABAQUS and the fluid-flow independent viscoelasticity by the collagen viscoelasticity described by equation (3.3) and (3.4).

In the previous studies of Li et al. (2005), it was found that the fluid flow dependent viscoelasticity “could be used to approximate the compressive load response of articular cartilage, provided that the instantaneous fibrillar modulus was used in the calculations.” In that case, equation (3.3) was reduced to represent elastic stress. For the problems in the present study, which are all restricted to small strains, the following simple equation was used for the contribution of the fibrillar matrix to the Jacobian:

$$G_x(0)E_x^{\mathrm{f}}(\varepsilon_x) = E_x^0 + E_x^{\varepsilon}\varepsilon_x \qquad (3.6)$$

where E_x^0 and E_x^{ε} are constants independent of strain but dependent on $\vec{x}$ and (*X, Y, Z*). They were for the instantaneous modulus of the fibrillar matrix, and thus were larger than those for the static equilibrium modulus. (Li *et al.*, 2009).

So for small deformation problems, the element D_{xx} in the Jacobian matrix of the fibril-reinforced model of cartilage was written as:

$$D_{xx} = \lambda + 2\mu + E_x^0 + E_x^{\varepsilon}\varepsilon_x \qquad (3.7)$$

The subscript *x* in Formula 3.2 - 3.7 can be replaced with *y* or *z* to obtain the corresponding equations in the $\vec{y}$ or $\vec{z}$ direction.

3.2.4 Implementation in commercial FE software

In the numerical procedure of the user-defined material subroutine - ‘‘UMAT” of Li et al. (2009), the equations derived above were implemented and ‘orthotropic properties were formulated with reference to the local Cartesian coordinates at the element level’. This ‘‘UMAT” can modify the collagen fibril modulus based on the fibrillar strain determined in the previous iterative step of ABAQUS.

So the first step to use ‘‘UMAT” in the fibril-reinforced models is to define the local Cartesian system for each element (or element set) using a separate process. As the process is different for the 2D axisymmetric and 3D models, the corresponding models are given in Sections 3.3 and 3.4 respectively.

3.3 Methods to Implement DT-MRI Data in the 2D Model

This section describes the method to define local coordinate system required for the 2D fibril-reinforced axisymmetric model and the process to implement the DT-MRI data. In addition, the steps to set up the 2D model are also introduced.

3.3.1 Geometry and mesh of the 2D model

In the 2D axisymmetric FE model, only the right half of the modified DT-MRI pixel grid of cartilage sample in Figure 2.1 was used as a structured mesh (17 rows and 37 columns) with the aspect ratio = 1(Figure 3.1).

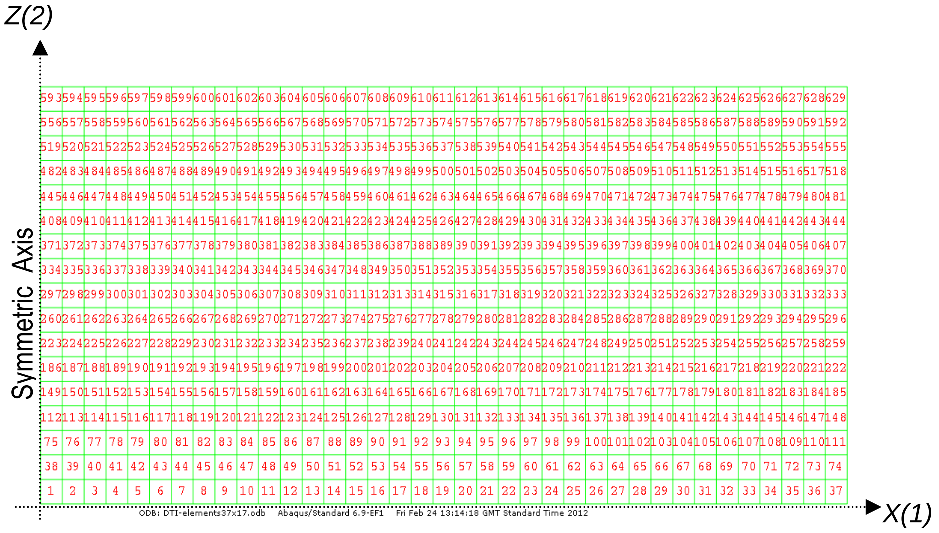

Figure 3.1 2D mesh corresponds to the pixel grid: (vertical axis: *Z(2)*; horizontal axis: *X* (1)).

3.3.2 Definition of the element level Cartesian coordinates in the 2D model

The local *x*, *y* and *z* directions were defined for each element using the ‘‘Orientation’’ option in Abaqus (Li *et al.*, 2009). The primary collagen orientation (i.e. the principal eigenvector corresponding to the maximum eigenvalue of the diffusion tensor; Section 2.2) was defined as the local *x*-axis: the three components (*Xij*, *Yij* and *Zij*; *i* =1···17, *j*=38···74) of every single principal eigenvector were implemented to the corresponding element to represent the fibril orientation in this element.

The 3-points method (right hand rule) in Abaqus Analysis user’s manual 2.2.5 (Figure 3.2) was used to define the local coordinates system: ‘a’ is the point lies on local *x*-axis and point ‘b’ is in the local *x*-*y* plane and near to local *y*-axis. The local origin ‘c’ is defaulted to be coincide with the origin of the global system and does not need to be input in ‘‘Orientation’’.

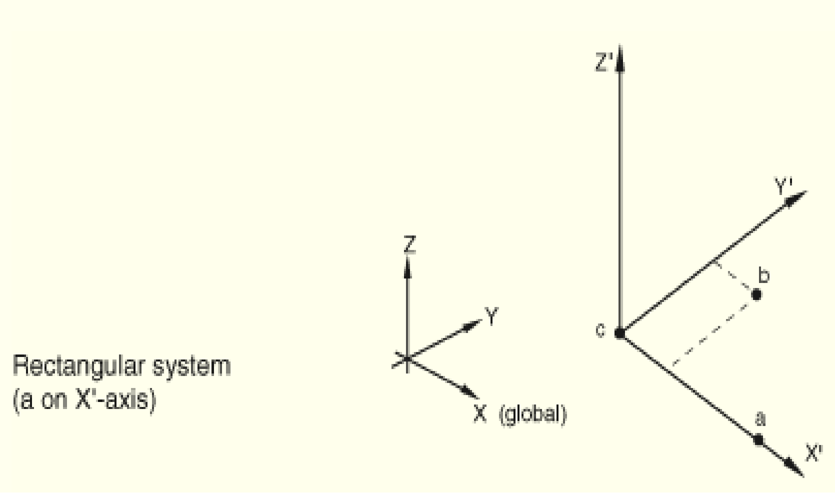

Figure 3.2 3-points method to define the local rectangular system (Abaqus Analysis user’s manual Figure 2.2.5-1).

When a user-defined orientation is used with two-dimensional solid axisymmetric elements, the direction must be redefined for the *X′(x)*- and *Z′(z)*-axis: the third direction (hoop direction) must remain unchanged (Abaqus Analysis user's manual 2.2.5). So only the *x*- direction needs to be defined, the *z*-direction will be confirmed automatically.

'Distribution' in ABAQUS was used to define local coordinate systems on an element-by-element basis:

1) To define a DISTRIBUTION TABLE of "COORD3D, COORD3D"; then define DISTRIBUTION for each element (or element set) referring to the distribution table. The distribution table for the coordinates specifies COORD3D twice to indicate that data for two three-dimensional-coordinate points must be specified for each element in the distribution.

2) To define ORIENTATION.

3) The ORIENTATION is then referred to by a general section definition.

As the hoop direction must remain unchanged, the three-dimensional coordinates (bX_k,bY_k,bZ_k) of the second point for every single element should be (0, 1, 0). Only the three components (*Xij*, *Yij* and *Zij*; *i* =1···17, *j* = 38···74) of every single principal eigenvector need to be implemented to the first point of the corresponding element.

The detailed code to use "DISTRIBUTION" in ORIENTATION is modified from Example 3 in Abaqus Analysis user's manual 2.7.1 and displayed in Figure 3.3:

```
*DISTRIBUTION TABLE, NAME=tab2
        COORD3D, COORD3D
*DISTRIBUTION, NAME=dist2, LOCATION=element, TABLE=tab2
                               , aX0,aY0,aZ0,bX0,bY0,bZ0
                element number, aX1,aY1,aZ1,bX1,bY1,bZ1
                element number, aX2,aY2,aZ2,bX2,bY2,bZ2


      …
*ORIENTATION, NAME=ORI, DEFINITION=COORDINATES
        dist2
*SOLID SECTION, ELSET=N_CART, material=CARTILAGE_MTL, ORIENTATION=ORI
```

Figure 3.3 “Distribution” to define the local rectangular system for each element in 2D models (Abaqus Analysis user’s manual 2.7.1).

Using the ‘‘UMAT’’ option in Abaqus, the strain dependent Young’s modulus derived in Section 3.2 was defined to the corresponding element of the 2D axisymmetric model (Figure 3.4). These strains are available in output file of Abaqus as the “elastic” strains (Figure 3.4; Abaqus User Subroutines Reference Manual 1.1.36 UMAT User subroutine to define a material's mechanical behavior).

After the implementation of ‘‘Orientation’’ and ‘‘UMAT’’, the 2D fibril-reinforced model was set up (Figure 3.4).

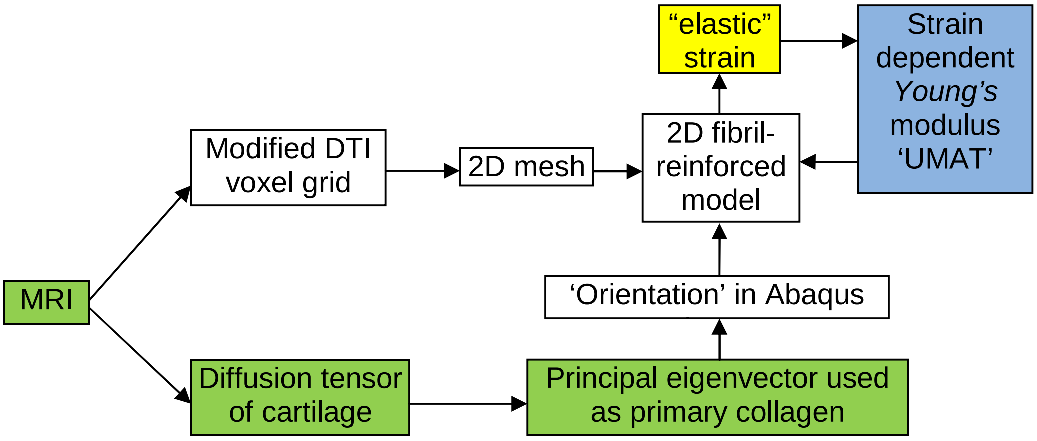

Figure 3.4 Flow chart of to implement DT-MRI data and "UMAT" in the 2D fibril-reinforced model.

3.4 Method to Implement DT-MRI Data in the 3D model

The method to define local coordinate system for the 3D model and the process to implement the DT-MRI data are described in this section. In contrast to the 2D model, all of the three coordinate axes of the local rectangular system in the 3D fibril-reinforced model were required to be defined.

3.4.1 Definition of the element level Cartesian coordinates in the 3D model

The 3-points method in Abaqus Analysis user's manual 2.2.5 (Figure3.2) was also used.

The origin **c**, point **a** lying on the local *x*-axis and point **b** lying on the local *y*-axis in Figure 3.5 were defined as below:.

1. Local origin **c**: coincide with global origin.

2. Point **a** on local *x*-axis - terminal point of the principal eigenvector $\vec{a}$: Similar to the way in the 2D model, $\vec{a}$ i.e. (*Xij*, *Yij* and *Zij*; *i* =1···17, *j*=1···74) is defined as the local *x*-axis (X' in Figure 3.2).

3. Point **b** on local *y*-axis - terminal point of vector $\vec{b}$ which is derived below (Figure 3.4):

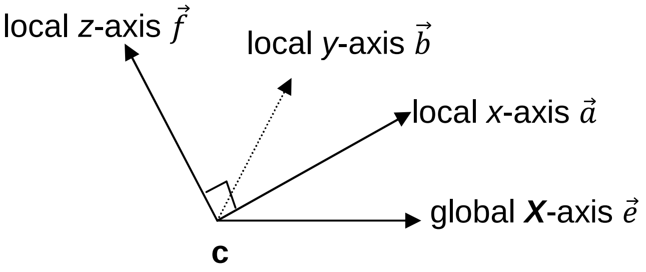

Figure 3.5 Definition of local *Y*-axis (vector $\vec{b}$).

Vector $\vec{e}$: the unit vector (1, 0, 0) from origin on global ***X***-axis.

Vector $\vec{f}$ is the unit vector from origin which is the cross product of vector $\vec{e}$ and vector $\vec{a}$, defining the direction of local *z*-axis (Figure 3.5):

$$\vec{f} = \vec{e} \times \vec{a} \quad \text{i.e. } (0, -Z_{ij}, Y_{ij}) \ \ldots\ldots\ldots\ldots\ldots\ldots \ (3.8)$$

Vector $\vec{b}$ is the unit vector from origin which is the cross product of vector $\vec{f}$ and vector $\vec{a}$, defining the direction of local *y*-axis (Figure 3.5):

$$\vec{b} = \vec{f} \times \vec{a} \quad \text{i.e. } (-Y_{ij}^2 - Z_{ij}^2, X_{ij}Y_{ij}, X_{ij}Z_{ij}) \ \ldots\ldots\ldots\ldots \ (3.9)$$

3.4.2 Definition of the element level Cartesian coordinates in the 3D model

To define the orientation of collagen fibril in each element set of the 3D model, the code to use ‘Distribution’ is:

```
*DISTRIBUTION TABLE, NAME=tab2
       COORD3D, COORD3D
*DISTRIBUTION, NAME=dist2, LOCATION=element, TABLE=tab2
                               , aX0,aY0,aZ0,bX0,bY0,bZ0
           element set number, aX1,aY1,aZ1,bX1,bY1,bZ1
           element set number, aX2,aY2,aZ2,bX2,bY2,bZ2


      …
*ORIENTATION, NAME=ORI, DEFINITION=COORDINATES
       dist2
*SOLID SECTION, ELSET=N_CART, material=CARTILAGE_MTL, ORIENTATION=ORI
```

Figure 3.6 ‘Distribution’ to define the local rectangular system for each element in 3D models (Abaqus Analysis user’s manual 2.7.1).

For the first coordinates point of the corresponding element set, the three components of every single principal eigenvector (Xij, Yij and Zij; i =1···17, j=1···74) were directly implemented. But for the second coordinates point, the three components were calculated in advance using Formula 3.9; then the result of calculation was implemented to the corresponding element set.

3.5 Summary

In order to set up the more realistic fibril reinforced poroelastic finite element models of articular cartilage incorporating the DT-MRI data, the material model employed in the analysis was developed first - the material subroutine “UMAT” in ABAQUS provided by Dr L. P. Li (University of Calgary) was used to define the strain-dependent Young’s modulus of collagen fibril. The detailed derivation of the equations used in the subroutine was provided in the related literature.

The specific method to implement of the DT-MRI data in the 2D axisymmetric and 3D model are described in Section 3.3 and Section 3.4 respectively. Meanwhile, the method to define the local y-axis in the 3D model has been developed independently. Details are given of the input file used to import the primary fibril orientation information.

These methods are adapted in the 2D and 3D fibril-reinforced models in Chapter 4 and Chapter 5 respectively.

Chapter 4 Effect of Modelling Fibril Orientation in Two-dimensional Axisymmetric Models

4.1 Introduction

Articular cartilage can be considered as a porous matrix saturated in water, reinforced by a fibrillar network. The porous matrix is nonfibrillar, representing the solid matrix excluding the collagen fibres as described in Section 3.2. From the view of simulating the tissue structure, the constitutive models of cartilage were classified as two types: the macroscopic models without consideration of the underlying tissue structure and the microstructural models mimicking the fibrillar network and the nonfibrillar matrix separately (Taylor et al., 2006).

Different modeling studies on the anisotropic material properties of articular cartilage: such as transversely isotropic models (Cohen et al., 1998 and Soulhat et al., 1999) and fibril-reinforced models (Soulhat et al., 1999; Li et al., 1999-2013; Wilson et al., 2004-2013; Shirazi et al., 2007 and Gupta et.al., 2009). However, no direct comparative studies have been made between the isotropic model and the fibril-reinforced model implementing realistic fibril orientation.

The aim of the work presented in this chapter is to investigate the capabilities of a 2D microstructural model (fibril-reinforced) in describing the fluid load support. The basic modeling methodology, which incorporates the material model described in Chapter 3, is introduced in the second section. The 2D axisymmetric cases, of various levels of complexity, are given for each case in terms of fluid load support, contact pressure, pore pressure and fluid velocity.

A series of 2D axisymmetric models with poroelastic material were set up systematically in the third section. First of all, a 2D isotropic poroelastic model was created and the mesh sensitivity analysis was carried out in the second section, in order to verify the rationality of the structured 2D mesh modified from the DT-MRI pixel grid (Section 3.3). Then the verified mesh was used in all of the 2D models in this section.

Then the results of the systematic models were compared and discussed in the following two sections.

4.2 Model and Method

The collagen fibril orientations derived from the DT-MRI data (Chapter 2) was implemented directly to the realistic fibril-reinforced model (Chapter 3). The top 2 layers' fibrils in Figure 2.2 were idealized to distribute horizontally to set up the semi-realistic model, with the fibril orientations in the remaining layers unchanged. Both of the above models employed strain dependent Young's modulus introduced in Section 3.2.2. The two uniform reinforced models incorporated constant and strain dependent Young's modulus respectively, with the local coordination system defined same as the global frame. The constant Young's modulus in the isotropic and uniformly reinforced models was adjusted, in order to let the vertical displacement in the two models match the realistic fibril-reinforced model at the end of the ramp loading.

4.2.1 Boundary conditions and load

The models in this chapter were set up to replicate unconfined compression of a cylindrical specimen of articular cartilage with 6.0mm diameter and 1.36mm thickness (excluding bone).The concentrated load of 0.2N was applied through a rigid plate with 6.4mm diameter over a ramp time of 2 seconds and then maintained for one hour (Figure 4.1).

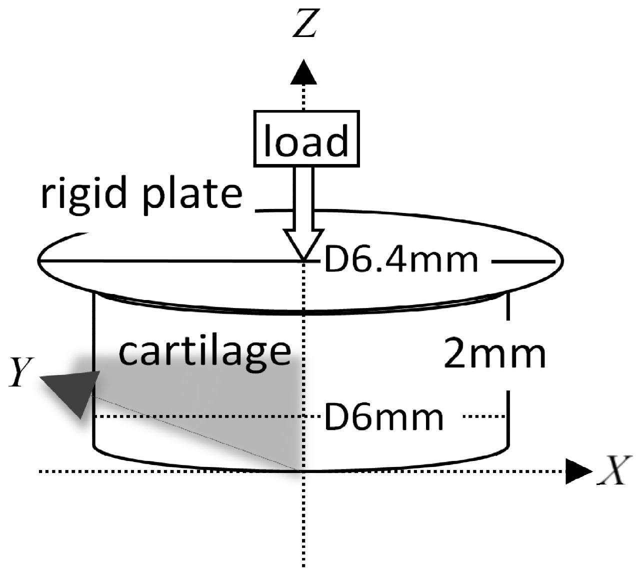

Figure 4.1 Schematic diagram of articular cartilage under unconfined compression.

Nodes along the cartilage base were constrained in both the horizontal and vertical directions, replicating a perfectly rigid substrate. The nodes on the vertical axis of symmetry were constrained in the horizontal direction. The pore pressure of the nodes at the open vertical edge was set to be zero. Flow was prevented from nodes on the bottom surface and at the axis of symmetry. The concentrated load was applied through the reference point of the rigid plate. The reference point was constrained in the horizontal direction to prevent translating; its rotation was also constrained. A contact condition, with a zero coefficient of friction, was created between the rigid plate and the top surface of cartilage.

4.2.2 Element type and mesh

A two dimensional axisymmetric finite element model was created to replicate the unconfined compression of cartilage (Figure 4.2). The mesh used in this model had 629 elements (Figure 3.1), which is identical to a half of the DT-MRI pixel grid: 17 rows and 37 columns with the aspect ratio = 1 (both horizontal and vertical resolutions are 70μm). The dimension of the cartilage geometry in this model did not exactly match the sample in Figure 4.1 due to the limitation of the DT-MRI pixel grid: no diffusion tensor was derived corresponding to the deepest part of cartilage (12.5% of the whole cartilage thickness) since the low water content (Pierce et al., 2010); neither in the side region of cartilage (13.7% of the cartilage radius) because of the image noise.

The first-order bilinear pore pressure CAX4P was used in all of the two dimensional models for the subsequent analyses in this chapter. First-order elements were adopted for the slave surface, in the two dimensional contact simulations, due to the possible problems created by the second-order elements in calculating the “consistent nodal loads for constant pressure” (ABAQUS Tutorials - Interactive Edition, 12.4.4). Furthermore, with the bilinear pore pressure element, the aim to investigate the fluid pressure and load support in cartilage could be readily investigated. However, hour-glassing problem was caused when the reduced-integration elements

CAX4RP were used in the reinforced models implementing fibril orientation and hence were not used.

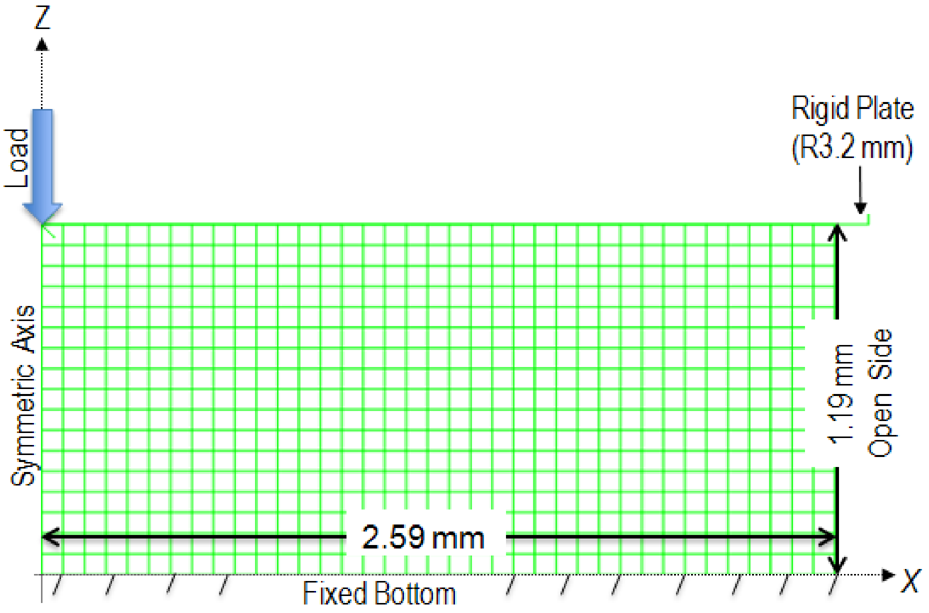

Figure 4.2 Schematic diagram of the 2D axisymmetric FE model simulating articular cartilage under unconfined compression (vertical axis: *Z*; horizontal axis: *X (r)*; into plane axis: *Y (θ)*).

4.2.3 Material model

Each of the model cases created were assigned a poroelastic material property, where both a solid and fluid phase were considered. In cases where fibre reinforcement was included a distribution of fibre orientations was created. The material model was modified in these local fibre directions. Where needed, fibril strain-dependence was introduced using a user-defined material subroutine. Details of this method are given in Chapter 3.

4.2.4 Mesh sensitivity analysis of the 2D isotropic model

In order to analyze the mesh sensitivity on the peak value of fluid load support, poroelastic material was employed in the 2D axisymmetric isotropic FE model:

For the solid elastic matrix, the material parameters were the Young's modulus E (Mononen et al., 2010) and the Poisson's ratio v (Li et al., 2009). The fluid flow within the matrix was described by the permeability k and the initial void ratio e_0 (pore volume over solid volume; Li et al., 1999 and 2009), which is required in the input file of ABAQUS. All material parameters were constant through the tissue depth (Table 4.1) i.e. the model was homogenous.

Table 4.1 Material parameters of isotropic model.

Material parameter	**Value**
Young's modulus, *E*	0.69 MPa
Poisson's ratio, *v*	0.36
Permeability, *k*	3.0×10^{-15} $m^4/N \cdot s$
Initial void ratio, e_0	4.0(80% interstitial fluid)

Mesh sensitivity analysis was carried out by reducing the element number by a factor of roughly 1/4 (1/2 × 1/2) and increasing it twice by 2 × 2 times. The coarser mesh had 144 (8 × 18) elements; the denser meshes had 2516 (34 × 74) and 10064 (68 × 148) elements respectively.

After 2 second of ramp deformation, the contact pressure distributions on cartilage surface did not show significant differences in most of the contact zone (Figure 4.3), except on the area near the open side (right edge in Figure 3.1) where the curve of 8 × 18 elements being slightly outside than those of other mesh densities. However, the curve of 17 × 37 elements used in the 2D isotropic model was much closer to both of the densest ones which nearly coincided to each other.

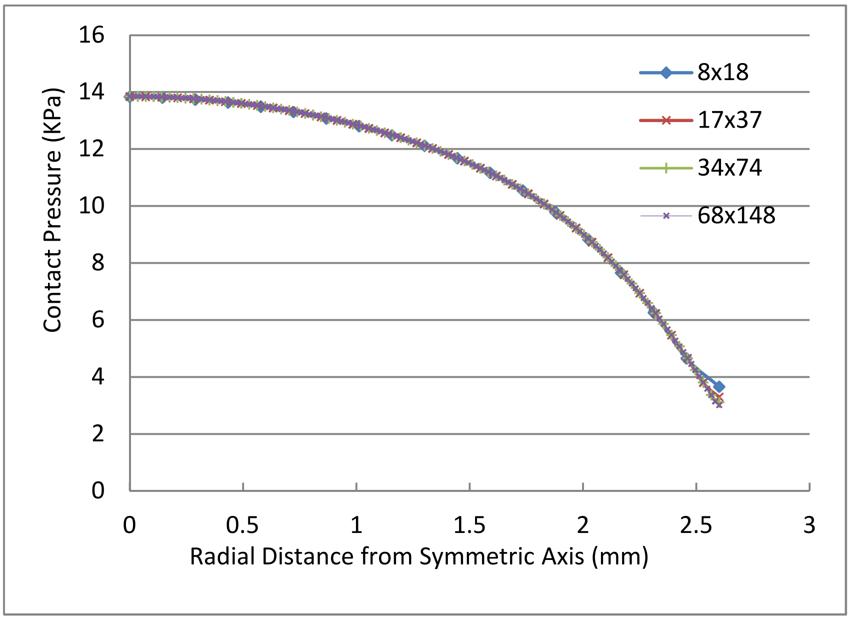

Figure 4.3 Distribution of contact pressure on cartilage surface at the end of ramp load (t = 2s).

As for the pore pressure, the curves of the two coarser meshes with 8 × 18 and of 17 × 37 elements both matched the two densest ones on the whole cartilage surface (Figure 4.4).

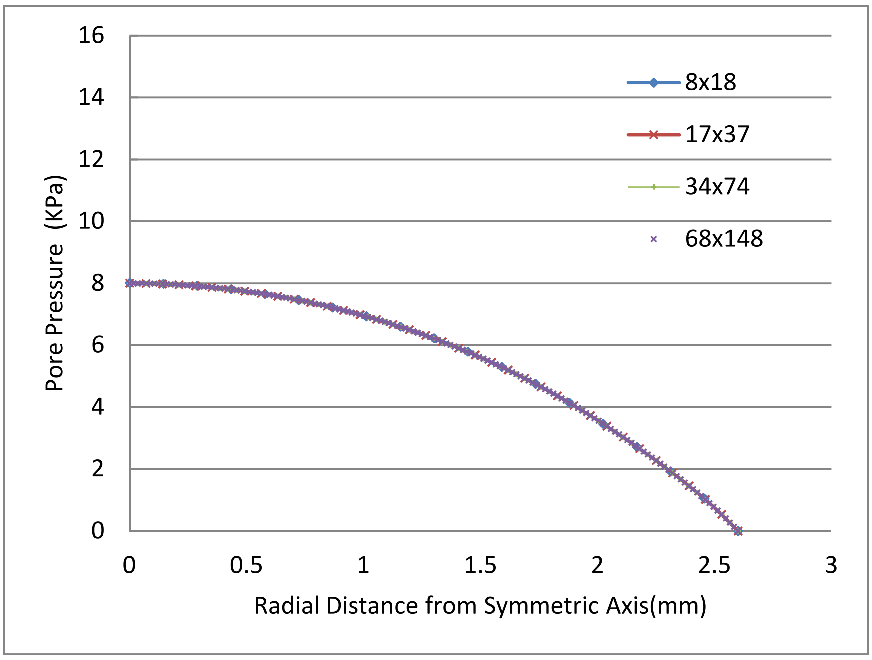

Figure 4.4 Distribution of pore pressure on cartilage surface at the end of ramp load (t = 2s).

Cartilage surface node on the symmetric axis was selected to observe the influence of mesh density on fluid load support in different models (Figure 4.5). The curve in Figure 4.3 clearly shows that the 2D isotropic model with the 629 (17 × 37) elements could achieve the similar value as the models using much denser mesh in predicting the fluid load support. The whole curve tended to be a horizontal line from the point corresponding to the mesh density (17 × 37) indicating the fluid load support was not sensitive to the continuing increase of mesh density. So it is reasonable to use this mesh (17 × 37) to predict fluid load support in the 2D axisymmetric models.

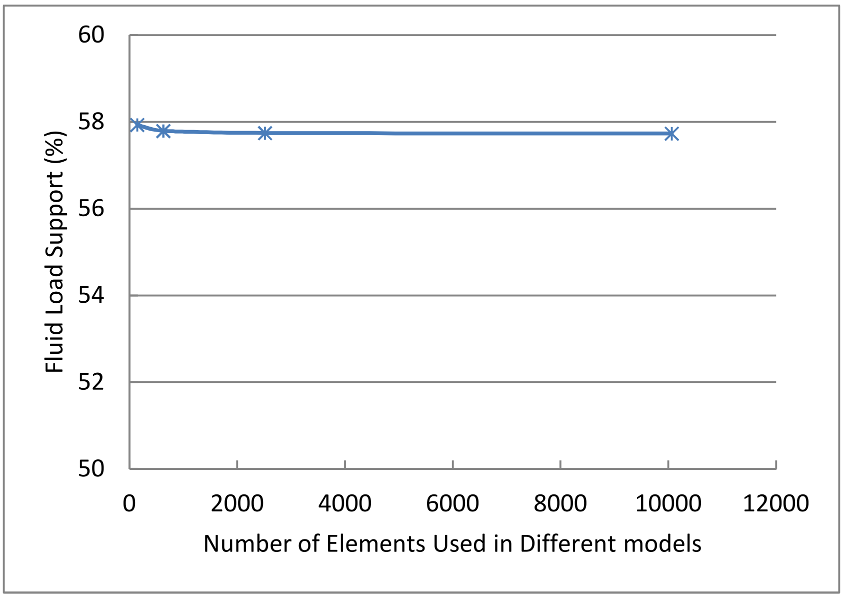

Figure 4.5 Fluid load support at cartilage surface node on the symmetry axis of different mesh density at the end of ramp load (t = 2s).

4.2.5 Parameter predictions of 2D models

Theoretically, the peak value of pore pressure should occur at the end of the ramp time. So most of the results used in the analysis are at the moment of t = 2s. The parameters of 2D models displayed below are measured in this chapter:

Contact pressure, pore pressure and fluid load support on cartilage surface

The total pressure on the contact area of cartilage surface may be different as the tissue particularly the collage fibril distribution is anisotropic. Wear and tear of cartilage may be related to the contact pressure, so it is crucial to investigate the contact pressure on the surface. Meanwhile, the pore pressure along the cartilage surface plays a vital role in the of tribology study within the human knee joint according the theory of biphasic lubrication. So it is important to record and compare the peak values of contact pressure and pore pressure on the surface of cartilage.

In the biphasic lubrication theory, fluid load support - the ration of contact pressure and pore pressure is more important than each individual variable. It represents the amount of applied load carried by the liquid phase in the cartilage. The most important thing is that it can interpret tribological mechanism of the load carrying between the solid and the liquid phase in the tissue and hence directly influence the friction coefficients on the cartilage surface.

The fluid velocity and contour of pore pressure

The fluid velocity (FLVEL) inside the cartilage represents the direction and magnitude of the fluid flow within the tissue, while the FLVEL on the open edge (open side) shows the speed of the interstitial fluid flowing out. The differences of pore pressure at the various parts of cartilage, illustrated by the contour, make the interstitial fluid flowing from the parts where pore pressure is higher to the other parts with lower pore pressure.

The radial and axial deformation of cartilage open edge

The pore pressure is a result of the interstitial fluid pressurization. In order to investigate the influence of collagen fibril implementation on the pressurization, the radial and axial deformation of cartilage open edge in different models were also recorded and compared to each other.

The radial stress on the cartilage surface

For the pathological investigation of the influence of collagen fibril implementation, the radial stress on the cartilage surface in all of the five 2D models was compared.

4.3 Modelling Cases

Three groups of 2D axisymmetric models were set up with different material settings: the realistic fibril orientation model and the simplified fibril orientation model (top 2 layers' fibril were designed to distribute horizontally) with strain dependent fibrillar Young's modulus (named DT-MRI and DT-MRI-top model respectively); the Uniform reinforced models with constant fibrillar Young's modulus (Uniform-Cons model) and the strain dependent fibrillar Young's modulus (Uniform-SD model); and the basic model with isotropic poroelastic material (Isotropic model) - totally five modelling cases. The geometry, mesh, boundary conditions and loading in Figure 4.2 were used in all of the five models. The material properties employed in these models, including the collagen fibril orientation (except in the Isotropic model), are described in Table 4.2.

Table 4.2 Material properties of different models (ε is the fibrillar strain in each iteration and initial void ratio 4.0 represented 80% interstitial fluid).

Modelling case / **Material parameter**	DT-MRI based group		Uniformly reinforced group		
	DT-MRI	DT-MRI-top	Uniform-SD	Uniform-Cons	Isotropic
Young's modulus of nonfibrillar matrix, E_m (MPa)	0.26	0.26	0.26	0.26	0.91
Poisson's ratio of nonfibrillar matrix, v_m	0.36	0.36	0.36	0.36	0.36
Young's modulus of fibril, Ef_x and Ef_y (MPa)	$3+1600\varepsilon$	$3+1600\varepsilon$	$3+1600\varepsilon$	2.15	n/a
Permeability, k (m^4/N·s)	3.0×10^{-15}	3.0×10^{-15}	3.0×10^{-15}	3.0×10^{-15}	3.0×10^{-15}
Initial void ratio, e_0	4.0	4.0	4.0	4.0	4.0
Orientation source for top 2 layers	DT-MRI	Manual uniform	Manual uniform	Manual uniform	n/a
Orientation source for lower 15 layers	DT-MRI	DT-MRI	Manual uniform	Manual uniform	n/a

The deformation of cartilage in different models under the same load would be dissimilar due to the completely different properties of material, although all other modelling factors were same. This made it difficult to compare the modelling results, since the cartilage deformation and fluid load support are closely related. In order to make the comparison reasonable, the value of Young's modulus in both the local x and y directions in Cons E model should be adjusted to match the vertical displacement of the cartilage surface in the DT-MRI model at the end of the ramp loading stage. The similar adjustment was done in the Isotropic model. To provide the information of the cartilage deformation to carry out this adjustment, the DT-MRI model was set up first.

4.3.1 Models of the DT-MRI based group

4.3.1.1 Mechanical property of material

In both of the DT-MRI and DT-MRI-top models, the nonfibrillar poroelastic matrix was isotropic with the *Young's* modulus E_m = 0.26 MPa, Poisson's ratio ν_m = 0.36, permeability k = 0.003 mm^4/Ns and the initial void ratio e_0 = 4.0 (Li *et al.*, 1999 and 2009). The *Young's* modulus of the fibrillar network was designed to be the same in the local *x* and *y* directions, $Ef_x = Ef_y = 3 + 1600\varepsilon$ MPa (Ef_x and Ef_y represents modulus in local *x* and *y* direction respectively), where ε is the fibrillar strain (Li *et al.*, 2009) as described in Chapter 3; while the *Young's* modulus in the local *z* directions Ef_z = 0 MPa. The values of the material parameters are displayed in Table 4.2.

The strain dependent *Young's* modulus of the fibrillar network (3 + 1600ε MPa) was implemented using the user-defined subroutine “UMAT” in ABAQUS provided by Dr L. P. Li, University of Calgary.

4.3.1.2 Implementation of fibril orientation

The user-defined "ORIENTATION" including "Distribution" introduced in Section 3.3 was used to incorporate the fibril orientation in each of the 2D solid axisymmetric elements: the principal eigenvector of a specific diffusion tensor was defined as the *x*-axis of the local Cartesian coordinates of the corresponding element.

ABAQUS requires the direction must be redefined for the local x- and z-axis while the local y-axis must remain identical with the global hoop direction (Abaqus Analysis user's manual 2.2.5). So only the direction of the local x-axis needed to be defined, the local *z*-axis would be confirmed automatically by right-hand rule in ABAQUS.

"ORIENTATION" in the DT-MRI model

The realistic fibril orientations derived from DT-MRI were incorporated in the DT-MRI model: the three components (Xij, Yij and Zij; i =1···17, j=38···74) of every single principal eigenvector were implemented to the corresponding element in Figure 3.2 to represent the fibril orientation in this element. As the element number in Figure 3.2 was increasing from bottom to top, the three components of principal eigenvector for the first element should be (X17,38, Y17,38 , Z17,38); part of the detailed code corresponding to Figure 3.3 is displayed below:

```
*DISTRIBUTION TABLE, NAME=tab2
        COORD3D, COORD3D
*DISTRIBUTION, NAME=dist2, LOCATION=element, TABLE=tab2
                              , aX_{0},aY_{0},aZ_{0},bX_{0},bY_{0},bZ_{0}
                             1, X_{17,38},Y_{17,38},Z_{17,38},0,1,0
                             2, X_{17,39},Y_{17,39},Z_{17,39},0,1,0
                            …
                            37, X_{17,74},Y_{17,74},Z_{17,74},0,1,0
                            38, X_{16,38},Y_{16,38},Z_{16,38},0,1,0
                            …
                            74, X_{16,74},Y_{16,74},Z_{16,74},0,1,0
                            …
                           629, X_{1,74},Y_{1,74},Z_{1,74},0,1,0
*ORIENTATION, NAME=ORI, DEFINITION=COORDINATES, SYSTEM=RECTANGULAR
        dist2

*SOLID SECTION, ELSET=N_CART, material=CARTILAGE_MTL, ORIENTATION=ORI
```

“ORIENTATION” in the DT-MRI-top model

In this model, fibrils in the top 2 layers in Figure 3.2 were designed to distribute horizontally. So the three components of every single principal eigenvector in the corresponding element (from the 556th to the 629th element) in the top 2 layers was (1,0,0), while the local Cartesian coordinates in others elements did not changed. The subroutine was changed as:

```
*DISTRIBUTION TABLE, NAME=tab2
       COORD3D, COORD3D
*DISTRIBUTION, NAME=dist2, LOCATION=element, TABLE=tab2
                            , aX_0,aY_0,aZ_0,bX_0,bY_0,bZ_0
                           1, X_{17,38},Y_{17,38},Z_{17,38},0,1,0
                           2, X_{17,39},Y_{17,39},Z_{17,39},0,1,0
                           …
                         555, X_{3,74},Y_{3,74},Z_{3,74},0,1,0
                         556, 1,0,0,0,1,0
                           …
                         629, 1,0,0,0,1,0
*ORIENTATION, NAME=ORI, DEFINITION=COORDINATES, SYSTEM=RECTANGULAR
       dist2
*SOLID SECTION, ELSET=N_CART, material=CARTILAGE_MTL, ORIENTATION=ORI
```

4.3.2 Models of the uniform reinforced group

Both of the Uniform-Cons model and the Uniform-SD model were the further simplification of the DT-MRI-top model: no specific orientation of collagen fibrils were implemented, the local Cartesian coordinate in each element was defined to be the same as the global system. The two uniform reinforced models were set up to investigate the influence of the strain dependent Young’s modulus of the fibrillar network by comparing to each other, and also the effect of fibril orientation implementation through the contrast with the DT-MRI model.

4.3.2.1 Mechanical property of material

Uniform reinforced model with constant Young’s modulus (Uniform-Cons)

In order to make the vertical deformation of the cartilage surface of the Uniform reinforced models match the DT-MRI model at the end of the ramp loading stage, the value of the Young's modulus Efx and Efy (represents modulus in local x and y direction respectively) in this model was adjusted while Efz = 0 (Figure 4.6).

In Figure 4.6, only the curve of the Uniform-Cons model with 2.15MPa Young's modulus could match the vertical deformation of the cartilage surface of the DT- MRI model at t = 2s. The other material parameters in this model (Table 4.3) were the same as the DT- MRI model. The user-defined subroutine "UMAT" was still used in this model, although the Young's modulus was constant.

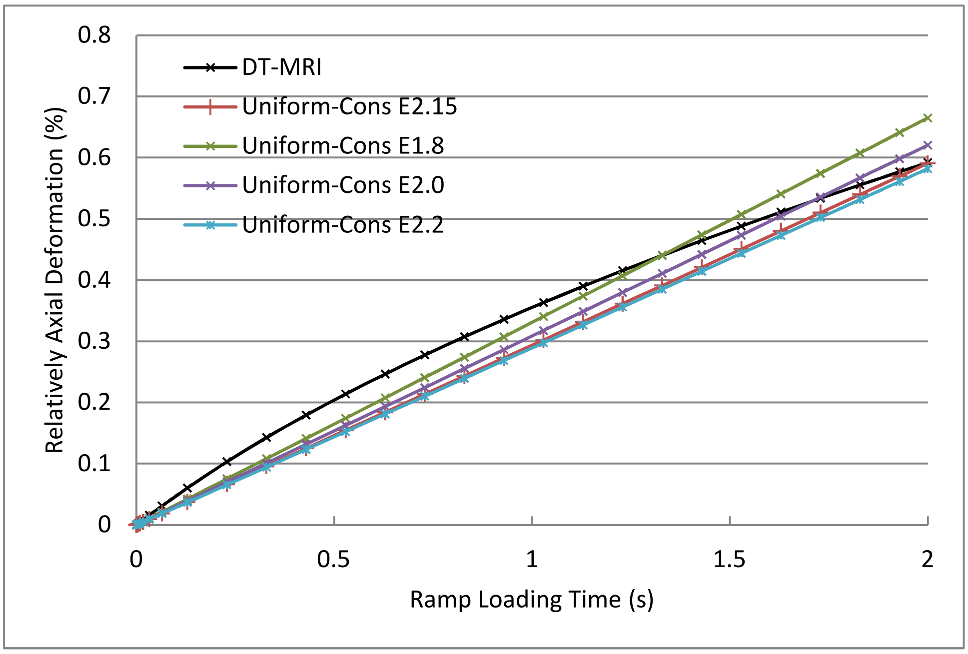

Figure 4.6 Adjustments of Young's modulus in the Cons E model to achieve the same maximum axial displacement as DT-MRI model at the end of ramp loading (t = 2s).

Uniform reinforced model with strain dependent Young's modulus (Uniform-SD)

The mechanical property parameters and their values of cartilage in this model were same as the DT-MRI model (Table 4.2) i.e. the Young’s modulus Efx and Efy was (3 + 1600ε MPa) respectively while Efz = 0. The user-defined subroutine “UMAT” was also used in this model to implement the strain dependent Young’s modulus of the fibrillar network.

4.3.2.2 Definition of the local coordinate system

For each element, the local Cartesian system was aligned with the global system. This effectively aligned the fibril orientation with the global X-axis in each case. Therefore, when the material model was modified based on this orientation, each element was given an equal, maximum reinforcement in the local x-direction. Instead of the user-defined “ORIENTATION” including “Distribution” in Section 3.3, the ‘Keyword’ method was used to define the local system by specifying the locations of points a, b, and c directly (Abaqus Analysis User's Manual 2.2.5). The data lines to define the orientation using DEFINITION=COORDINATES can be found in “ORIENTATION” of Abaqus Keywords Reference Manual. The detailed input file in these two models to define the local Cartesian coordinate was:

```
*Orientation, name=Ori-1, DEFINITION=COORDINATES, SYSTEM=RECTANGULAR
1.0, 0.0, 0.0, 0.0, 1.0, 0.0
```

4.3.3 The isotropic poroelastic model

In order to produce the comparable results, the value of Young’s modulus E in Table 1 was adjusted to be 0.91MPa to make the vertical deformation of the cartilage surface in Isotropic model match the DT- MRI model at the end of the ramp loading stage (Figure 4.7).

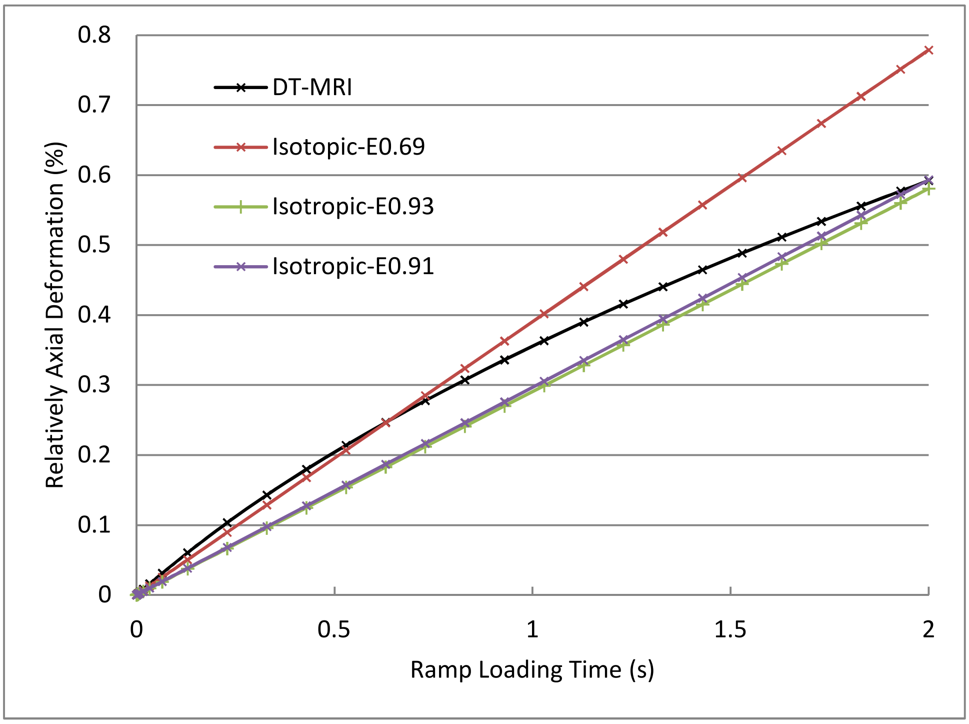

Figure 4.7 Adjustments of Young’s modulus in the ISO model to achieve the same maximum axial displacement as DT- MRI model at the end of ramp loading (t = 2s).

4.4 Results

The results from different models such as the contact pressure, the pore pressure, the fluid load support and the stress along the cartilage surface were collected and compared in a same figure. The axial and radial displacements of nodes on the open side were also compared. The fluid velocity and the contour of pore pressure through the whole cartilage sample were displayed separately.

In all of the modelling cases, nodes at the bottom of the lowest layer were prevented from displacing by the applied boundary conditions at that point; the radial deformation was normalized by the cartilage radius (2.59 mm) and the axial deformation by the cartilage thickness (1.19 mm).

4.4.1 Contact pressure, pore pressure and fluid load support on cartilage surface

Variation of the contact pressure distribution along the cartilage surface was apparently different among the three model-groups (Figure 4.8): The DT-MRI and DT-MRI-top model had a much higher maximum value but decreased faster while the other models varied smoothly. The slight difference between the curves of Uniform-Cons and Uniform-SD models showed that the strain dependent Young's modulus of collagen fibril did not affect contact pressure markedly in this group.

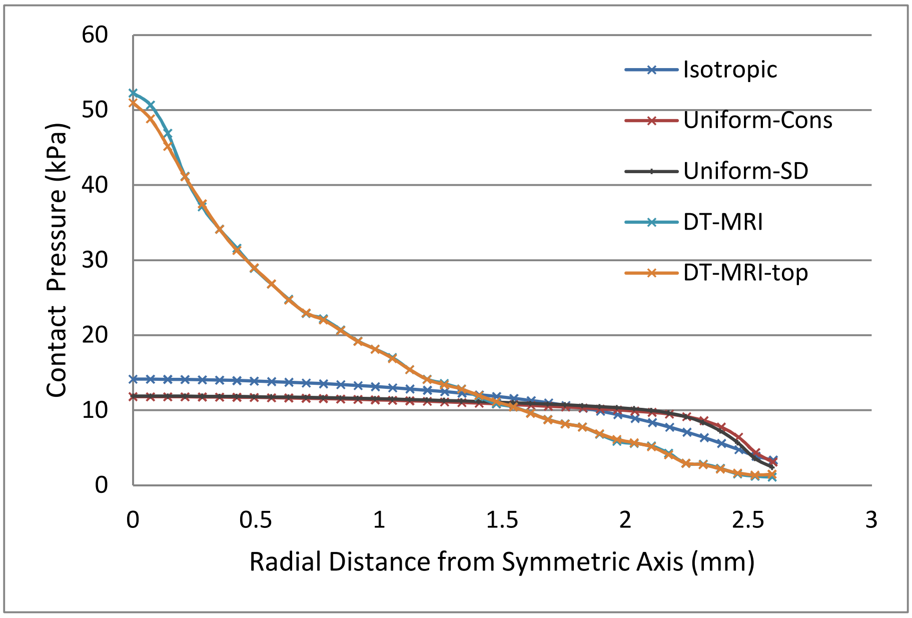

Figure 4.8 Distribution of contact pressure along cartilage surface at the end of ramp loading (t = 2s).

Figure 4.9 clearly shows that fibril reinforcement could increase the value of pore pressure comparing to the ISO model. It can also be found that strain dependent Young's modulus influenced pore pressure of Uniform-SD model more apparently than it did on contact pressure in Figure 4.8.

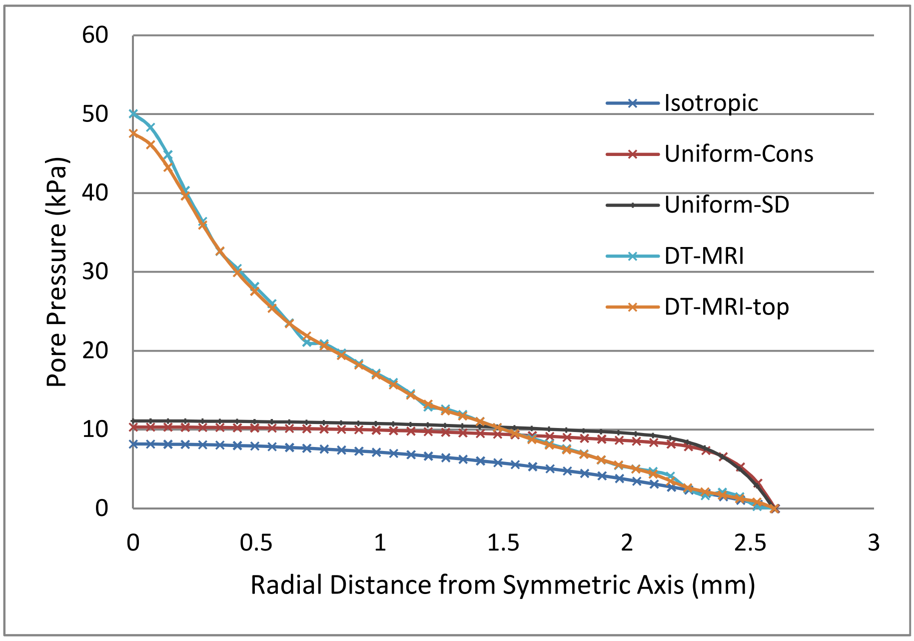

Figure 4.9 Distribution of pore pressure along cartilage surface at the end of ramp loading (t = 2s).

The value of fluid load support at the contact zone of cartilage surface in the four models with fibril reinforcement increased markedly compared to the simple Isotropic model (from <60% to >80%), although there were more fluctuations in the curve of the DT-MRI model than those of the other three models (Figure 4.10).

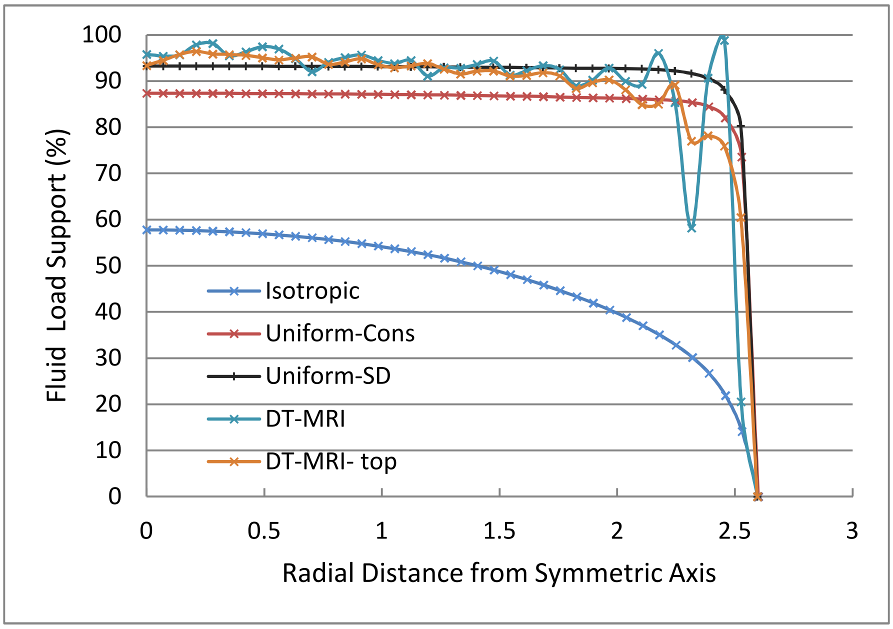

Figure 4.10 Comparison of fluid load support along cartilage surface at the end of ramp loading (t = 2s).

Figures 4.8 - 4.10 clearly show the peak value of observed parameters located on the symmetric centre of cartilage surface (except the fluid support of DT-MRI and DT-MRI-top models). The detailed values of the observed parameters at the end of ramp loading (t = 2s) are compared in Table 4.4.

Table 4.4 Comparison of results on axisymmetric surface centre of cartilage sample at the end of ramp loading (t = 2s).

Results on surface centre **Models**		**Contact pressure (KPa)**	**Pore pressure (KPa)**	**Fluid load support (%)**
Isotropic model		14.15	8.18	57.80
Uniform reinforced models	Uniform-Cons	11.67	11.0	87.33
	Uniform-SD	11.91	11.10	93.26
Realistic fibril distribution models	DT-MRI	52.26	50.06	95.78
	DT-MRI-top	50.95	47.57	93.35

Although the peak value of fluid load support in the Uniform-SD model was similar as that of the DT-MRI model (Table 4.4), it decreased much more rapidly after ramp load, while the load was maintained (Figure 4.11).

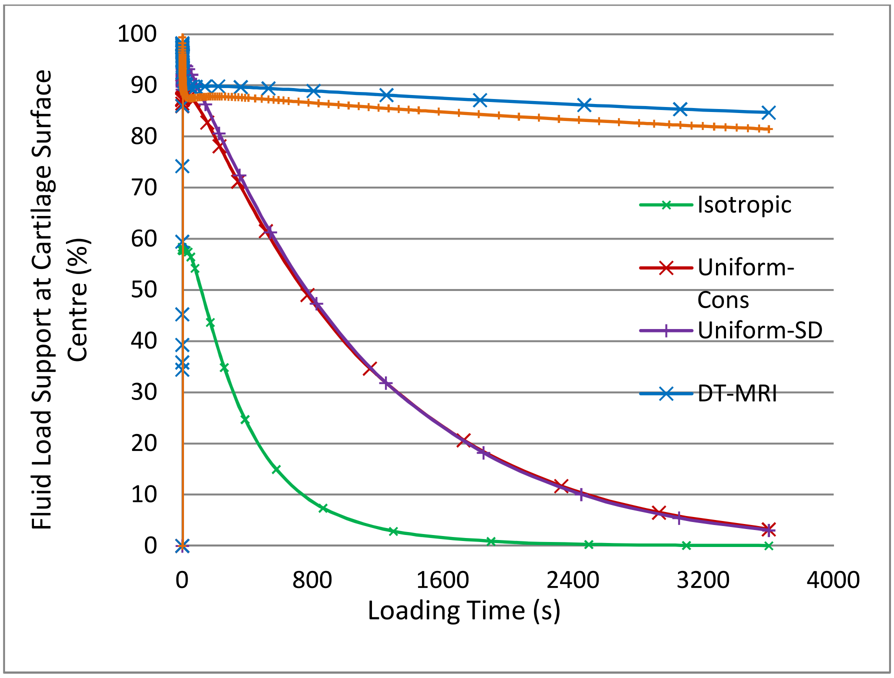

Figure 4.11 Comparison of fluid load support at the centre of cartilage surface during loading period.

4.4.2 The fluid velocity of cartilage

The fluid velocity (FLVEL) was fairly homogeneous in the Isotropic model and the Uniform reinforced models (Figure 4.12). In those cases, it increased from top to bottom along the open side (right) edge of cartilage although the magnitude was obviously higher in the two latter models. Both uniformly reinforced models generated velocity maps which were aligned with the fibril orientation, showing less fluid movement between layers than in the isotropic case.

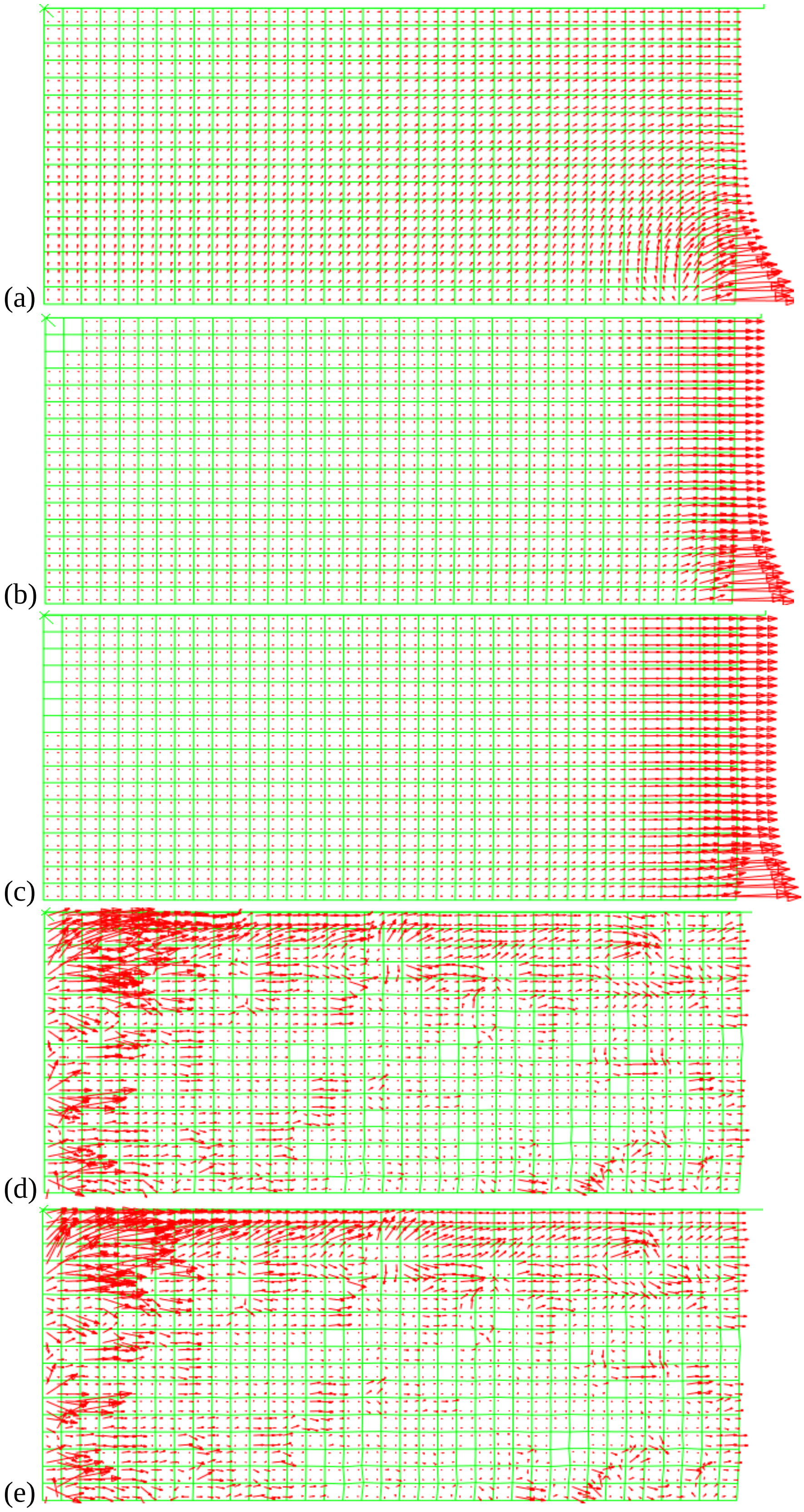

Figure 4.12 Fluid velocity (mm/s) of (a) Isotropic, (b) Uniform-Cons, (c) Uniform-SD, (d) DT-MRI and (e) DT-MRI-top at the end of ramp loading (t = 2s).

In the DT-MRI and DT-MRI-top cases, the velocity direction was highly variable. The higher velocity magnitude close to the Isotropic model and the Uniform reinforced models but much more concentrated around the symmetric axis. The lower magnitude close to the open edge implies that the fluid was trapped and less had been expelled at this time point (t = 2s). In the meantime, no apparent difference was found between the two models in the same group, except the more regular distribution in the first layer elements of the DT-MRI-top model compared to the DT-MRI model (Figure 4.12).

4.4.3 The contour of pore pressure within cartilage

The map of pore pressure throughout the tissue was similar for the two models within the same group. This is particularly clear for the two DT-MRI based models (Figure 4.13). However, the contours of pore pressure showed apparent differences in magnitude and distribution among the three groups of models. Low pressure region near the open edge is much wider in the DT-MRI group models than in the Uniform reinforced models; it is even wider near the cartilage surface in the Isotropic model but decreases rapidly to the cartilage bottom. High pressure regions near the symmetric axis in the DT-MRI group models confirm that fluid is trapped and pressurised in that area, when compared to the uniform distribution in the other cases (Figure 4.13).

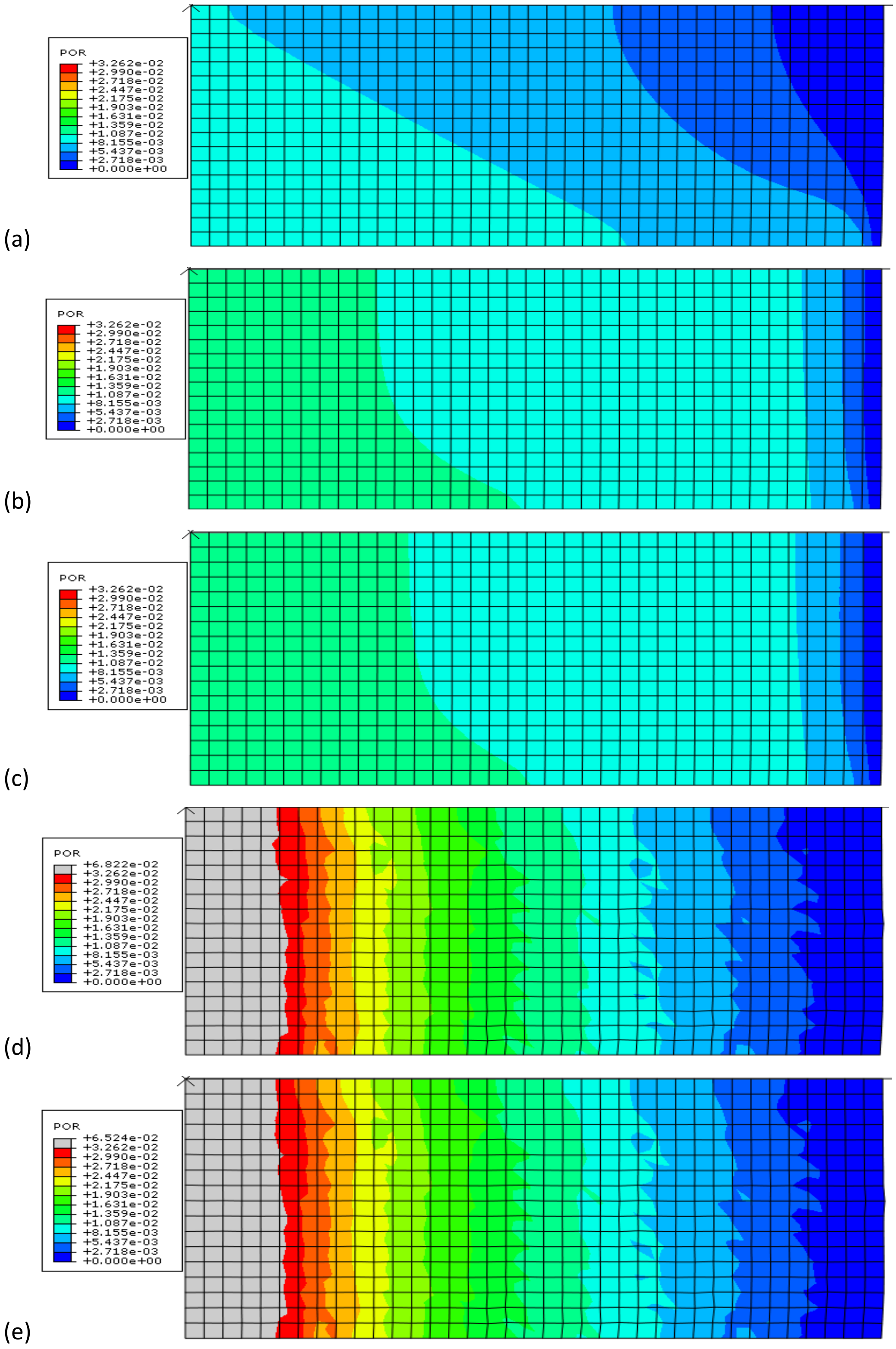

Figure 4.13 Contour of pore pressure (MPa) of (a) Isotropic, (b) Uniform-Cons, (c) Uniform-SD, (d) DT-MRI and (e) DT-MRI-top model at the end of ramp loading (t = 2s).

4.4.4 The radial and axial deformation of the cartilage open edge

4.4.4.1 The radial deformation of nodes on the open edge of cartilage

In Figure 4.14, the radial deformation of cartilage open edge was lowest in the Uniform-SD model; it decreased gradually from top to bottom in the curve of the Isotropic model but began to decrease from the 5th and 10th layer respectively in the Uniform-Cons and the Uniform-SD model.

In the curves of the DT-MRI model and the DT-MRI-top model, radial deformation of the top seven layers (nodes 1st-8th in Figure 4.12) was much lower than those in the Isotropic model although it was higher on the other ten layers (nodes 9th -18th); meanwhile, the top 2 layers in the DT-MRI-top model deformed apparently less than the DT-MRI model (Figure 4.14).

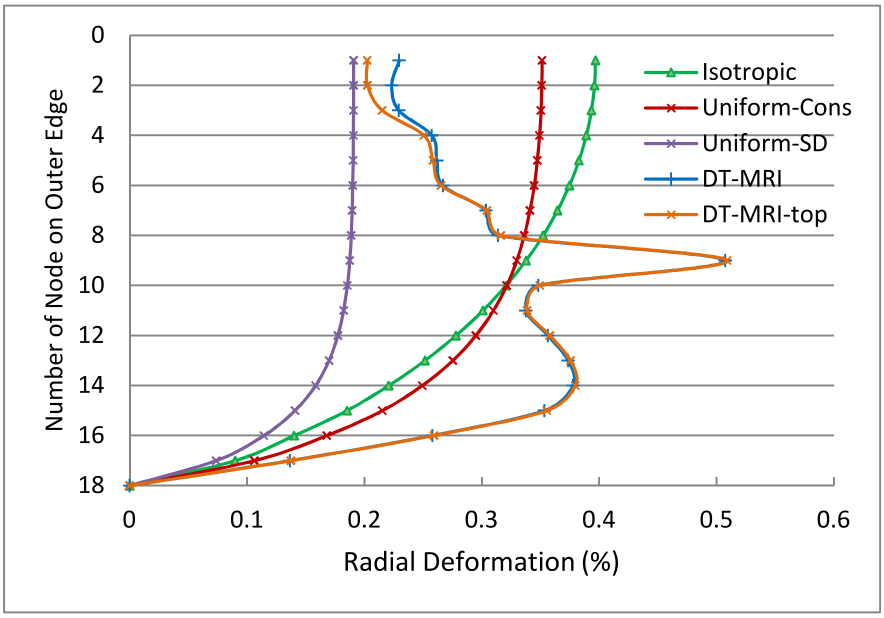

Figure 4.14 Comparison of radial deformation on open edge of cartilage at the end of ramp loading (t = 2s).

4.4.4.2 The axial deformation of the cartilage open edge

Although the Isotropic and Uniform-Cons model was designed to match the axial deformation of the DT-MRI model at the end of ramp loading (Figure 4.6 and 4.7), the axial displacement of each individual node along the open edge and the axial deformation of each layer of cartilage may be different.

The axial displacement of each node along the open edge of cartilage

The axial displacements of the nodes on the open edge of cartilage in the three models with same total axial deformation (i.e. Isotropic, Uniform-Cons and DT-MRI) were truly different. But between the corresponding nodes in the two models of DT-MRI group, only on the upper parts of the open cartilage edges were slight difference found while the lower parts of the open edges were nearly coincide. Nodes in the Uniform-SD model had the lowest axial displacements compared to the other four models (Figure 4.15).

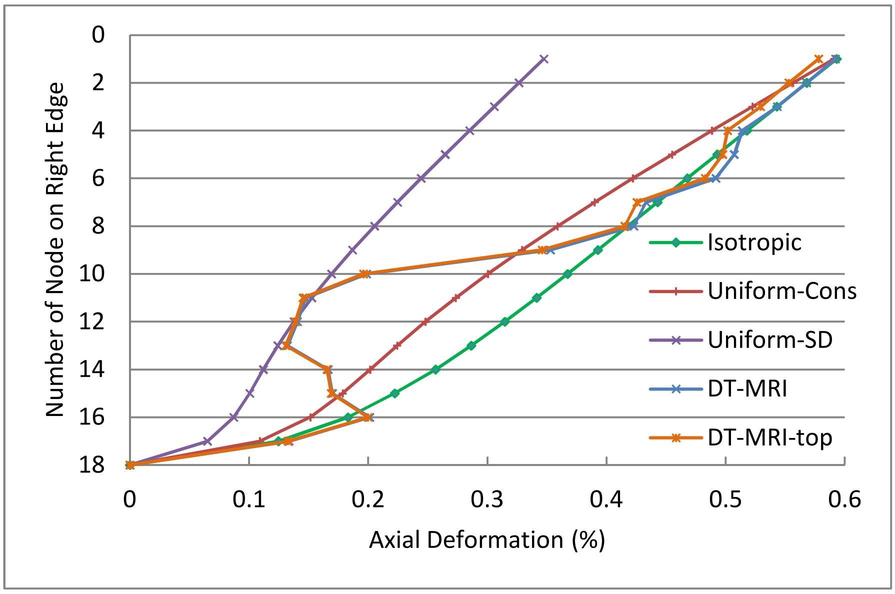

Figure 4.15 Comparison of axial displacement of nodes along the open edge of cartilage at the end of ramp loading (t = 2s).

The axial deformation of each layer of the cartilage

The axial deformation of a specific cartilage layer was defined as the difference of the axial displacement of the top and bottom vertex of the corresponding element along the open edge. This can be calculated from Figure 4.15: the difference of two contiguous nodes in the same curve (from top to bottom) was the axial deformation of cartilage layer between the two nodes (Figure 4.16). As the curves of the two models of DT-MRI group are nearly coincide (Figure 4.15), the axial deformation of cartilage layers of the DT-MRI-top model was not calculated in order to make the curves more distinguishable.

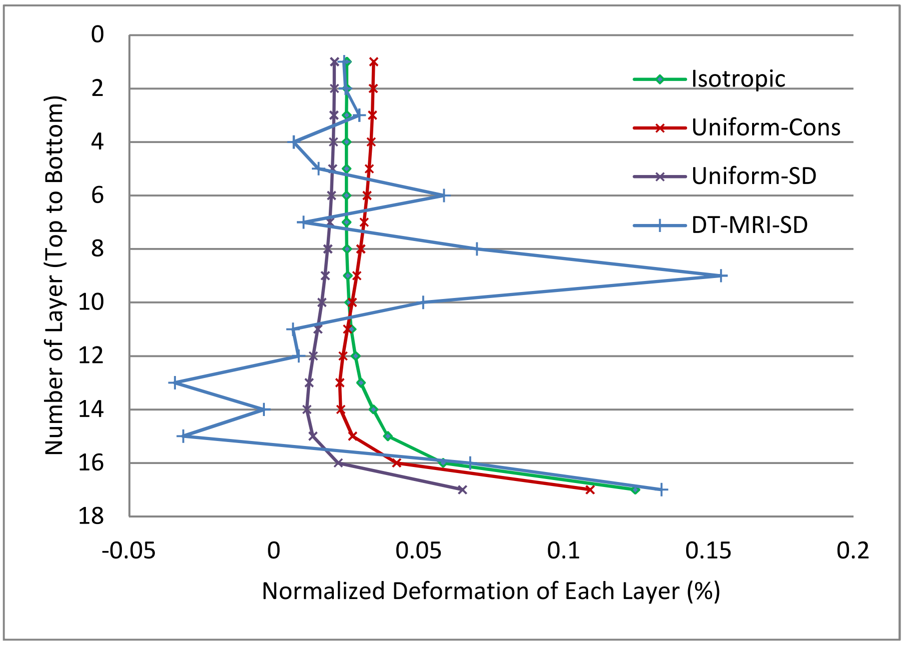

Figure 4.16 Comparison of axial deformation of elements along the open edge of cartilage at the end of ramp loading (t = 2s).

4.4.5 The radial stress on the cartilage surface

Radial stress around the symmetric axis along the cartilage surface was much higher in the two groups of fibril reinforced models than that in the Isotropic model. Larger fluctuations appeared in the curve of the DT- MRI model compared to the DT-MRI-top model, while the curves of other three models distributed smoothly (Figure 4.17).

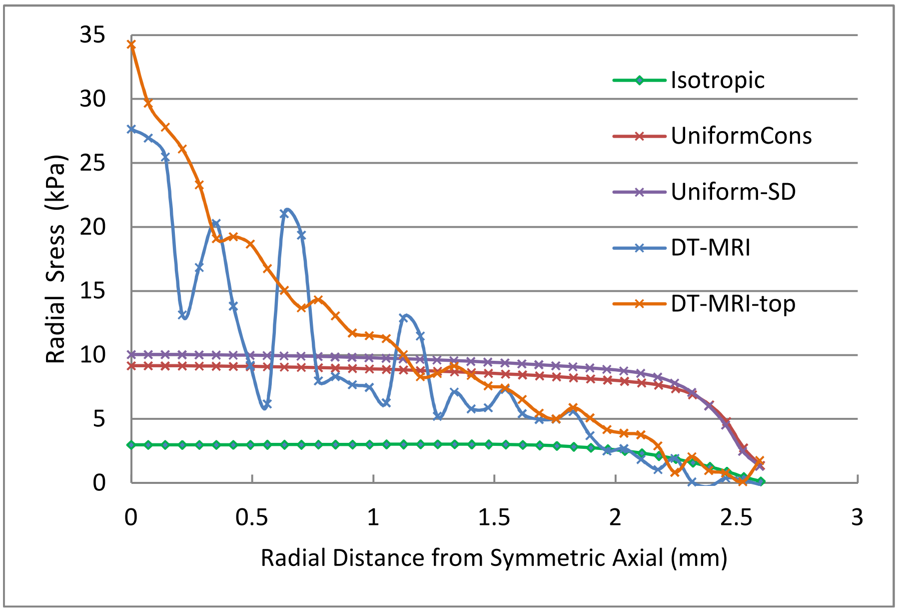

Figure 4.17 Distribution of radial stress (S11) along cartilage surface at the end of ramp loading (t = 2s).

4.4.6 The axial deformation of cartilage during loading period

The normalized axial deformation of cartilage was compared across all five models during the full loading period (Figure 4.18). After one hour’s creep all models had reached equilibrium with the exception of the group of DT-MRI based models.

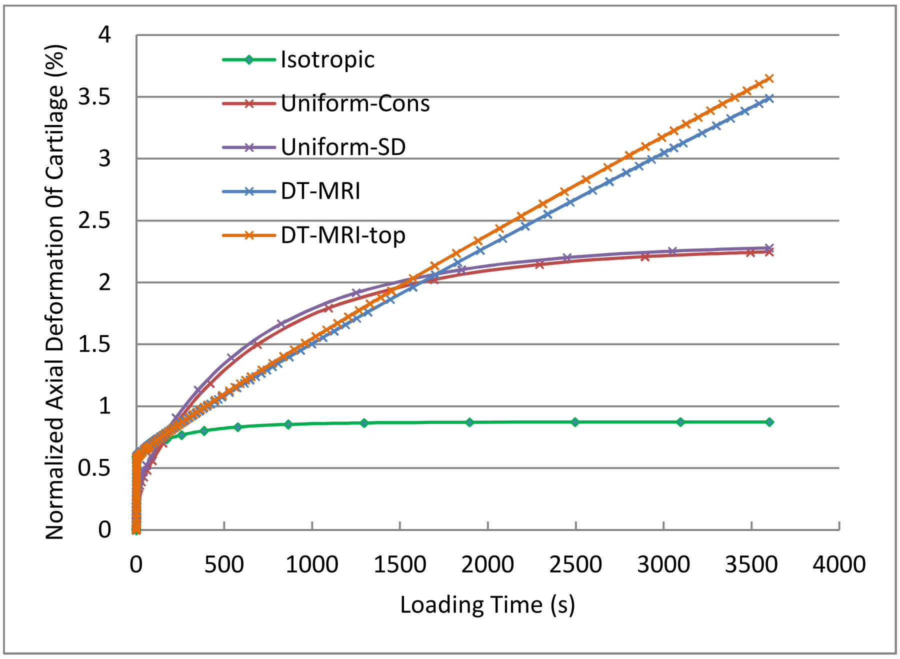

Figure 4.18 Normalized axial deformation of cartilage during the loading period (3602s).

4.5 Discussion

The functional role of collagen in unconfined compression of articular cartilage was clarified when the tension-compression nonlinearity had been incorporated in the theoretical modelling of cartilage collagen (Soltz and Ateshian, 2000): the high tensile stiffness of collagen acts in a similar way to as the rigid side-wall of a confining chamber, to resisting lateral expansion, and pressurizing the interstitial fluid considerably. The combination of these factors enables the interstitial fluid to support most of the applied external loading. However, no numerical results from realistic fibril-reinforced cartilage model have been reported to support the interpretation directly. The findings from implementing collagen fibril direction derived from DT-MRI data in this study were reasonably consistent with Park et al. (2003) and provided direct support to the theoretical explanation (Ateshian, 1996).

4.5.1 The effect of the user defined subroutine “UMAT”

4.5.1.1 The effect on the surface zone of cartilage

With the implementation of “UMAT” to the four reinforced models, the Young’s modulus in the axial direction (0.26 MPa) was defined much lower than in the Isotropic model (0.91 MPa). Theoretically, the axial deformation of the upper part of cartilage (the top two layers in Figure 4.2) in the reinforced models would be much greater than in the Isotropic model. However, the axial deformation of the top two cartilage layers in the reinforced models was nearly same as in the Isotropic model except slightly larger in the Uniform-Cons model (Figure 4.16). This was due to the powerful reinforcement of the large Young’s modulus in the radial direction ((0.26 + 2.15) MPa in the Uniform-Cons model or (0.26 + 3 +1600ε) MPa in the other three models) defined by the “UMAT”.

Compared to the Isotropic model, the cartilage surface in these four models was strengthened in the radial direction and became tangentially stiffer - radial stress around the symmetric axis along cartilage surface was therefore much higher in these models than that in the Isotropic model (Figure 4.17). Similarly, the underneath part of the top two layers of cartilage was also somewhat strengthened and became tangentially stiffer. When the cartilage was compressed, this upper zone in the reinforced models moved down readily with less radial deformation than those in Isotropic model (Figure 4.14) i.e. the lateral expansion of this zone was resisted by the higher tensile stiffness of collagen fibril in the reinforced models. Hence, pressurization of interstitial fluid in the upper part of cartilage in the reinforced models was enhanced markedly and higher pore pressure was produced (Figure 4.9 and Table 4.4) to support the applied load (Figure 4.10).

4.5.1.2 The effect on pore pressure and fluid velocity throughout the cartilage

As the hop direction remained unchanged in the 2D axisymmetric models, the Young’s modulus in this direction was still much greater than in the axial direction in the deeper region under the top two layers of cartilage in the reinforced models. So the “UMAT” not only enhanced the pressurization of interstitial fluid in the upper part of cartilage (Figure 4.9), but also throughout the tissue to produce different fluid flow in contrast with the Isotropic model (Figure 4.12 and 4.13).

As mentioned in Section 4.2.5, the differences of pore pressure at the various parts of cartilage made the interstitial fluid flowing from the parts with higher pore pressure to the other parts where pore pressure was lower. In the uniformly reinforced models implementing “UMAT”, high pore pressure distributed in the majority area of cartilage ((b) and (c) in Figure 4.13) leading to the fairly homogeneous fluid velocity within the tissue ((b) and (c) in Figure 4.12). Meanwhile, zero pore pressure distributed along the outer edge almost evenly and the adjacent area with low pore pressure was narrow ((b) and (c) in Figure 4.13). The higher pore pressure next to these two area produced a high fluid velocity and let the interstitial fluid flowed freely out through the whole edge ((b) and (c) in Figure 4.12).

For the Isotropic model, zero pore pressure distributed more and more wide from bottom to top along the outer cartilage edge ((a) in Figure 4.13). So the large difference of pore pressure was only produced near the corner between the outer edge and the bottom of cartilage ((a) in Figure 4.13) leading to the concentrated high fluid velocity at this corner ((a) in Figure 4.12).

4.5.2 The influence of the realistic fibril orientation

In the DT-MRI group models, the implementation of the realistic fibril orientation caused an inhomogeneous pore pressure field ((d) and (e) in Figure 4.13). The fluid was channelled towards lower pressure elements causing bottlenecks in the flow. It therefore took more time for the fluid to be expelled from the structure and a larger amount of pressure was built for a particular ramp load. Furthermore, the area of zero pore pressure and the adjacent low pressure area ((d) and (e) in Figure 4.13) were much wider than those in the uniformly reinforced models ((b) and (c) in Figure 4.13). The fluid in these two area could not get the high velocity from the tiny pressure difference between the two area. So the fluid flowing out of the cartilage was much less than in the uniformly reinforced models ((d) and (e) in Figure 4.12). All of these factors caused by the realistic fibril orientation combined together and led to the long maintaining of the high fluid load support at the centre of cartilage surface (Figure 4.11) although this is not consistent with the literature (Mow et al., 2005). However, this phenomena was also found in the equilibrium model of Kazemi et al. (2011) using the same “UMAT” and also implementing the realistic fibril orientation: the value of pore pressure was also remarkably high (66% of the peak value) after 2000 seconds’ creep.

As introduced in Section 2.4, several collagen fibril angles were greater than 50° in the top two layers. Although this phenomenon had been explained by

Visser et al. (2008b), it did cause the larger fluctuation of fluid load support in DT-MRI model. In the case where the fibrils in the top two layers were idealized to be flat, the curve of the DT-MRI-top model varied much more smoothly (Figure 4.10).

4.5.3 The effect of strain dependent Young’s modulus

Strain-dependent Young’s modulus had very little influence on contact pressure along cartilage surface in the two uniformly reinforced models (Figure 4.8). However, it did affect the pore pressure along cartilage surface more apparently (Figure 4.9 and Table 4.4). This is due to the markedly difference of radial deformation of cartilage top layer between the two models (Figure 4.14), compared to the much less difference of axial deformation in Figure 4.16. So the interstitial fluid in the top layer of cartilage in the Uniform-SD model was pressurized more greatly than in the Uniform-Cons model and the higher pore pressure was produced.

4.5.4 Limitation of the 2D axisymmetric DT-MRI model

There are a number of limitations related to the realistic fibril orientation in the 2D axisymmetric model.

First of all, the applied load was limited to 0.2N in the 2D model implementing fibril orientation derived from the DT-MRI data while much higher load (≥ 2.6N) could be applied to the Isotropic and uniformly reinforced models. Even the load was so low, the 2D DT-MRI based models were difficult to achieve the equilibrium after one hour’s creep (Figure 4.18).

Another limitation is the consideration of the fibril orientation in the 2D axisymmetric model: when it was rotated around the axis of symmetry, one vertical (or oblique) fibril in the 2D plane formed a ring of reinforced material which does not exist in the real tissue.

In order to solve the above problems, three dimensional fibril reinforced model will be set up in the following chapter.

Chapter 5 Three-dimensional Fibril-reinforced Model

5.1 Introduction

The systematic 2D axisymmetric models with poroelastic material set up in Chapter 4 investigated the capabilities of the fibril-reinforced model in describing the fluid load support in articular cartilage. However, the 2D DT-MRI based model could only support a low load (0.2N) and was difficult to achieve the equilibrium after one hour creep (Figure 4.18). This made it impossible to validate the fibril-reinforced model with the data under the higher load, or simulate physiological stress and strain conditions. In order to solve this problem, a 3D fibril reinforced model is set up in this chapter implementing the fibril orientation derived from the DT-MRI data, and the modeling result is compared to the corresponding information recorded from the unconfined compression experiment under a higher load of 5.4N. Furthermore, the fibril orientations from the whole DT-MRI slice can be implemented to the 3D model while only half of the DT-MRI data used in the 3D model.

As in Chapter 4, a simple 3D isotropic poroelastic model was created to carry out the mesh sensitivity analysis in the second section. The geometry of the 3D model was set up first. The element type was then determined and the mesh sensitivity analysis was performed. The verified mesh was used in all of the 3D models in Section 3 including the model implementing DT-MRI data, the uniformly reinforced model incorporating constant Young’s modulus and the isotropic model.

In the fourth section, the normalized vertical displacement of cartilage surface was transformed from the experimental record of cartilage thickness provided by Dr Robin Damion, derived in the MRI experiments. The curve of cartilage deformation during the creep test was also produced. In order to fit this curve, the values of the material parameters of the DT-MRI based model were adjusted to carry the higher applied loads.

In Section 5, the results of the models in Section 3 were compared and the validation results from Section 4 were also displayed. Then, all of these results were analyzed in the final section.

5.2 Model and Method

The 3D models in this chapter were set up to replicate the unconfined compression of a cylindrical specimen of articular cartilage with 6.0mm diameter and 1.36mm thickness (excluding bone; Figure 4.1). The cartilage was fixed to the bone. The concentrated load was applied through a rigid plate over a ramp time of 2 seconds and then maintained for one hour (Figure 4.1). The following boundary conditions, geometry, and mesh were used in all of the 3D models.

5.2.1 Geometry of the 3D models

As introduced in Chapter 2, the orientations of the collagen fibrils were derived from the DT-MRI data by scanning a cross-section slice of a cylindrical cartilage sample (Figure 2.1). There were no such data in other parts of the cartilage to define the direction of the collagen fibril in those areas. The limited fibril orientation information means that we must make assumptions which extrapolate the data from the single slice to any 3D volume modelled. So the cylinder geometry should not be used in the 3D model, although it was most accurate. However, the scanning slice itself could not be used to simulate the cylindrical cartilage specimen, with a thickness of only 2.0mm along the global Y-axis (Figure 5.1).

In order to implement the collagen fibril orientation throughout the cartilage geometry in the 3D fibril reinforced model, the structured pixel grid of diffusion tensor MRI with 17 rows and 74 columns (Figure 5.1) was extruded to 5.18mm along the global Y-axis. The rectangular cube was formed as the geometry of the 3D model (Figure 5.2), with 5.18 × 5.18 mm^2 squared top surface and bottom perpendicular to global Z-axis.

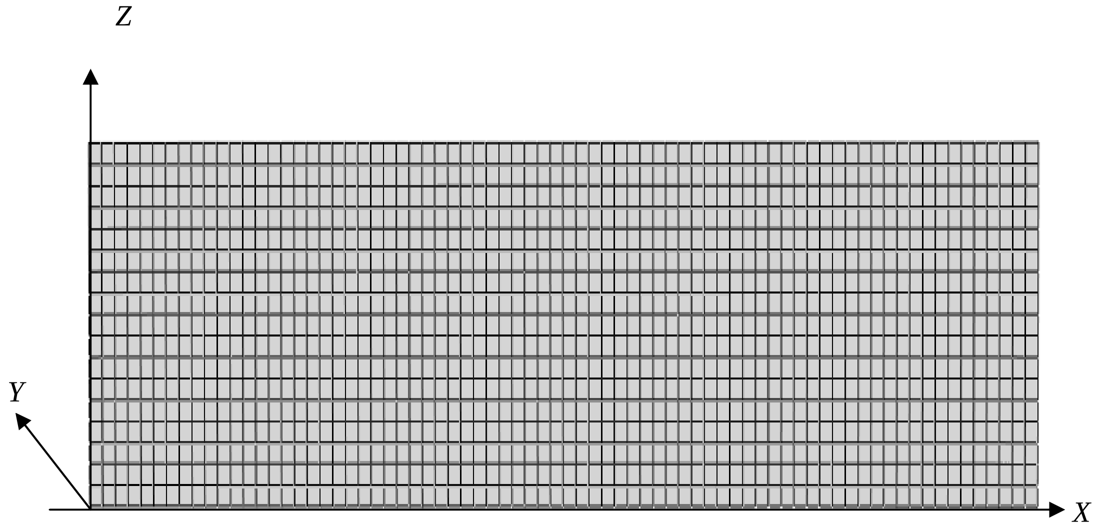

Figure 5.1 The structured pixel grid of diffusion tensor MRI (17 rows and 74 columns).

5.2.2 Boundary conditions and load

As in the 2D axisymmetric models in Chapter 4, all nodes on the cartilage base were constrained in all directions, replicating a perfectly rigid substrate. The pore pressure at the nodes on the outer cartilage edges was set to be zero. Flow was prevented from nodes on the base and top surface of cartilage. The 1.1N concentrated load was applied through the reference point of the rigid plate. The reference point was constrained in the horizontal direction to prevent translation parallel to the surface; its rotation was also constrained. A contact condition, with a zero coefficient of friction, was created between the rigid plate and the top surface of cartilage. The soil consolidation procedure in ABAQUS was used to simulate the creep test in the tissues.

5.2.3 Material model

Each of the 3D model cases was assigned a poroelastic material where both a solid and fluid phase are considered. In cases where the fibre reinforcement was included, a distribution of fibre orientations was created. The material model was modified in these local fibre directions. Fibril strain-dependence was introduced using a user-defined material subroutine.

5.2.4 Mesh of the 3D models

5.2.4.1 Element type

For the three dimensional contact problems simulated in this thesis, the twenty-node hexahedral elements (C3D20) in ABAQUS experienced very slow solver convergence (Li et al., 2009). In order to reduce the running time of the 3D finite element models, reduced integration with lower-order integration was used to form the element stiffness (ABAQUS 6.10, Analysis user’s manual 25.1.1). For example, the hexahedral element C3D20 has 27 integration points while C3D20R has only 8. Therefore, element assembly is roughly 3.5 times more costly for C3D20 than for C3D20R. However, the first-order, reduced-integration elements such as C3D8R may cause hour glassing problem in 3D stress/displacement analyses in Abaqus/Standard. Since these elements have only one integration point, it is possible for them to distort in such a way that the strains calculated at the integration point are all zero leading to uncontrolled distortion of the mesh. However, the second-order reduced-integration elements do not have the same difficulty (ABAQUS 6.10, Analysis user's manual 25.1.1). According to this point and also to include the interstitial pore fluid analysis, the C3D20RP element was chosen for the 3D models.

5.2.4.2 Mesh of the 3D model

On the vertical surface perpendicular to global Y-axis in the 3D model (Figure 5.2), the mesh was identical with the structured pixel grid of the MRI imaging i.e. 17 rows and 74 columns of elements with both vertical and horizontal dimensions were 70μm.

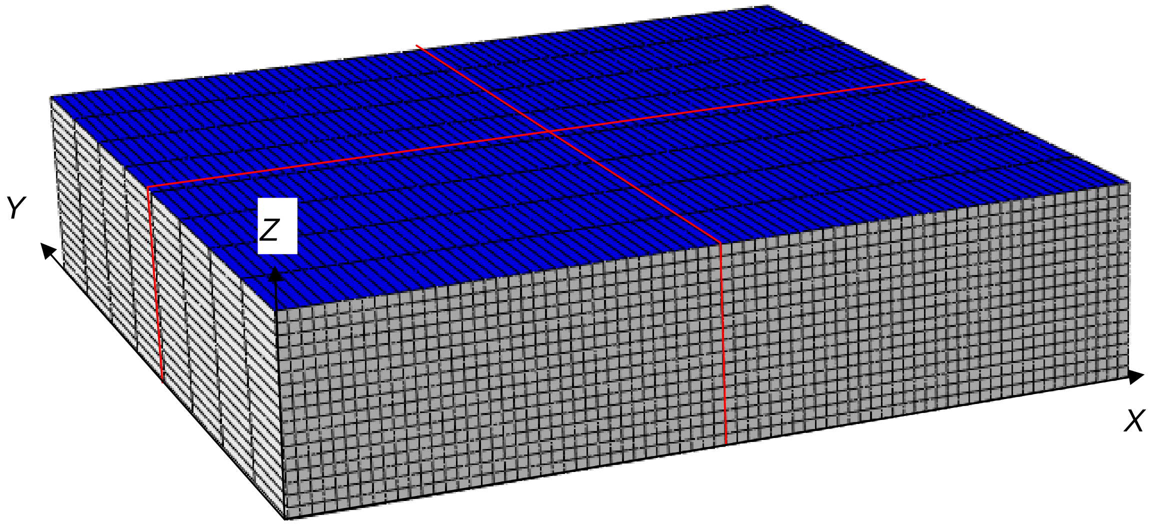

Figure 5.2 Mesh of the 3D fibril-reinforced cartilage model with 8×17×74 elements.

For the convenience to define the centre and midlines on the top surface of cartilage, the element number along the cartilage edge parallel to the Y-axis was designed to be even. In order to determine this specific number, mesh sensitivity analysis was carried out.

5.2.5 Mesh sensitivity analysis of the 3D isotropic model

In order to analyze the mesh sensitivity on the peak value of fluid load support, poroelastic material in Table 4.1 was employed in the 3D axisymmetric isotropic FE model: Young's modulus E = 0.69 MPa (Mononen et al., 2010), the Poisson's ratio v = 0.36, the permeability k = 0.003 $mm^4/N{\cdot}s$ and the initial void ratio e_0 = 4.0 (Li et al., 2009). The model was homogenous i.e. all material parameters were constant through the tissue depth.

As the element numbers along the edge parallel to the X and Z-axis were coincide to the MRI pixel grid (17 rows and 74 columns; Figure 5.1), the mesh sensitivity analysis was performed by doubling the even number of elements along the cartilage edge parallel to the Y-axis. In order to save the computation time, '8' was selected to be the initial number.

The 3D isotropic models with the mesh densities of 32×17×74 and 64×17×74 elements were too computationally intensive to be practical. So only the results of two models with 8×17×74 (Figure 5.2) and 16×17×74 elements were compared:

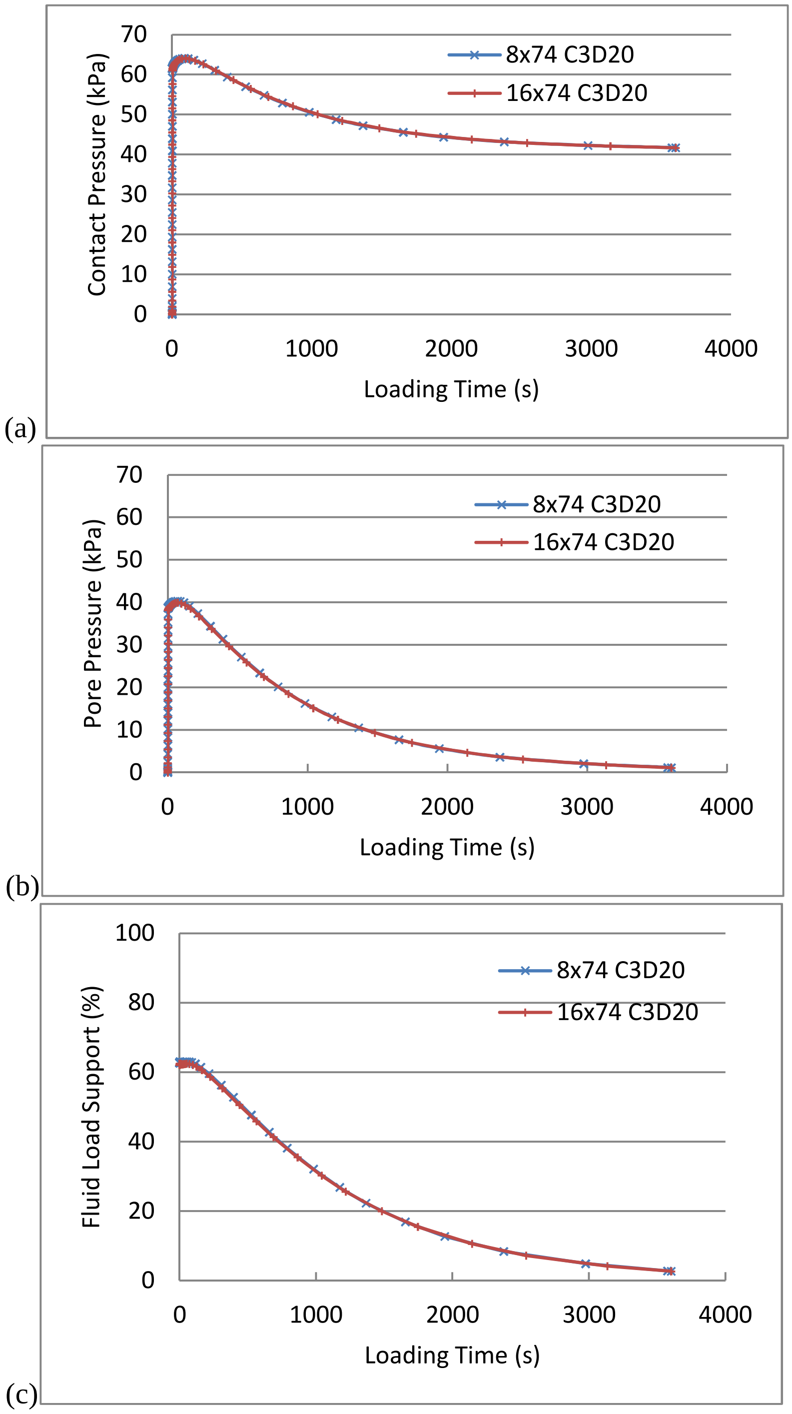

Figure 5.3 Comparison of contact pressure (a), pore pressure (b) and fluid load support (c) at the centre of cartilage surface in isotropic models with different number of elements during the simulation (t=3600s).

The axial displacement of cartilage surface during the simulation is also compared in Figure 5.4:

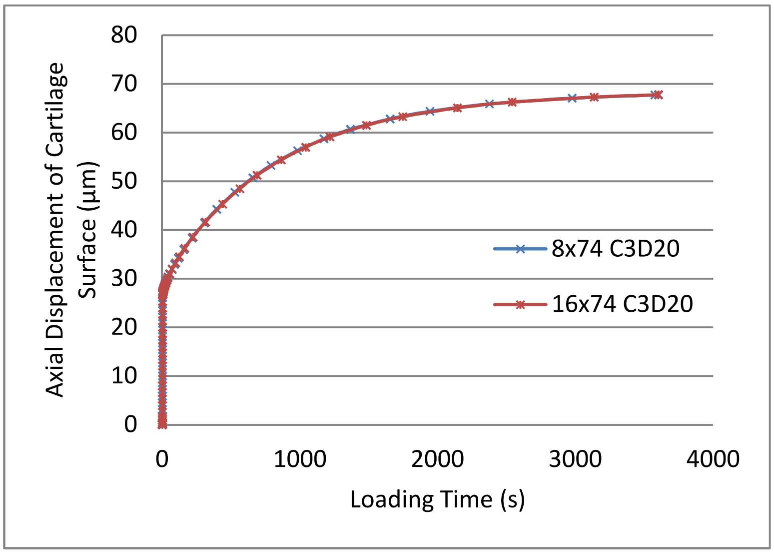

Figure 5.4 Comparison of axial displacement of cartilage surface in isotropic models with different number of elements during the simulation (t=3600s).

In Figures 5.3 and 5.4, no apparent differences were found between the corresponding curves of the two 3D isotropic models with different element number. To reduce the running time of computation, the mesh with 8×17×74 elements was selected to set up the 3D fibril-reinforced model.

5.2.6 Method to implement the DT-MRI data

The similar method as that in the 2D axisymmetric model introduced in Section 3.3 was used in the 3D model to implement the DT-MRI data (as the collagen fibril orientation). The collagen fibril orientation was defined it as the x-axis of the local rectangular coordinate system.

Except the similar part in the process to set up local system, there were two important differences in the 3D model in contrast with the 2D axisymmetric model according to Section 3.4. First, two coordinate axes of the local system were required to be defined in the 3D model while the coordinates of point b lying on the local y-axis needed to be calculated in advance. The second difference was, in each single horizontal layer of the 3D mesh (Figure 5.2), all of the eight elements along each unique line perpendicular to the vertical surface with 17×74 elements were defined as an element set - totally 1258 element sets. All other seven elements in the same set were implemented with the same fibril direction (and also the same local system) as the corresponding element on the vertical surface.

To implement the orientation of collagen fibril to each element set in the DT-3D model, the code to use ‘ORIENTATION’ and ‘DISTRIBUTION’ was the same as the one in Figure 3.6.

5.2.7 Outputs from the 3D models

The output parameters in this chapter were similar as those in the 2D axisymmtric models and most of the parameters were measured at the end of the ramp loading i.e. the instant at t = 2s. However, the detailed positions to collect these data were different due to the more complicated geometry and element type. The element vertexes on the cartilage surface were selected to form a path in the 2D models, and the values of the chosen parameters on this path were recorded. But in the 3D models meshed by C3D20RP elements, the path was composed of the midpoint of the related element edges on the cartilage surface since the contact pressure was zero on all of the element vertexes on cartilage surface.

5.2.7.1 Contact pressure, pore pressure, fluid load support and stress on the surface of cartilage

Theoretically, the pore pressure with higher values should distribute in the central area of the cartilage in the 3D models. As the element numbers along the cartilage edge parallel to the global X- and Y-axis were designed to be even (74 and 8 respectively) in Section 5.2.3, there were two existing midlines crossing the centre on the cartilage surface in Figure 5.2. So the surface paths used to collect the parameter value were defined to coincide with these two midlines respectively, composing of the integration points of the corresponding hexahedral element. The path parallel to the global X-axis was named as Midline-X including 74 integration points, while the other one parallel to the global Y- axis was Midline-Y having 8 points (Figure 5.5).

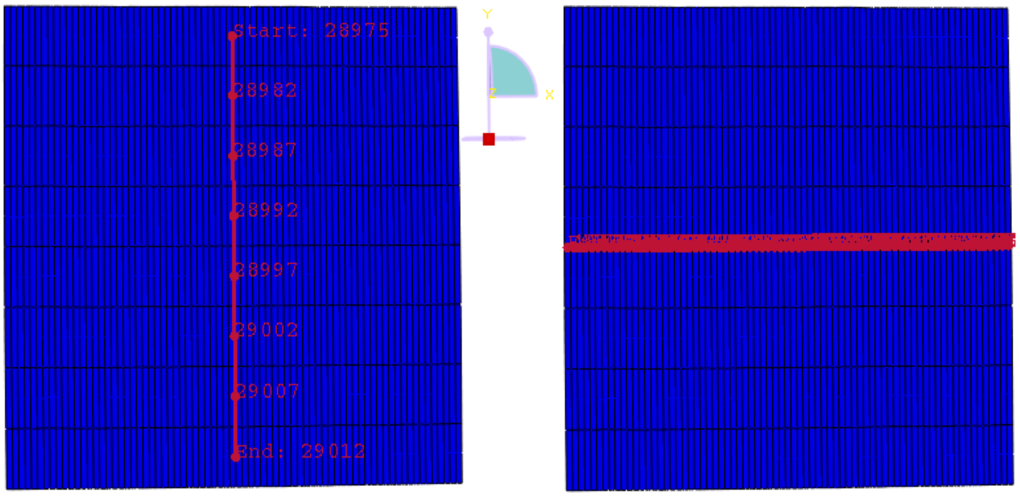

(a) (b)

Figure 5.5 Paths defined on the cartilage surface to collect the data of related measurements in the 3D models (a) Midline-Y parallel to the global Y-axis; (b) Midline-X parallel to the global X-axis (from right to left).

5.2.7.2 The fluid velocity and contour of pore pressure

The fluid velocity (FLVEL) within the cartilage represents the direction and magnitude of the interstitial fluid flow. The contour of pore pressure illustrates the pressure distribution at various parts of the cartilage. In the 2D axisymmetric models in Chapter 4, the distributions of these two parameters could only be displayed in a two dimensional map representing the distributions at any other parts of the realistic three dimensional cartilage. This may be feasible in the homogeneous models such as isotropic (or transversely isotropic) model. But for the non-homogeneous models, particularly the fibril reinforced model implementing realistic fibril orientation, it is unreasonable due to the anisotropic material properties of the tissue.

For the 3D models in this chapter, the distributions at any part inside cartilage could be investigated directly by view-cutting (ABAQUS manual - Getting Started) the 3D geometry of the tissue. The most frequently used patterns to cut the cartilage are the two cross-sections along the two midlines (red lines in Figure 5.6) and perpendicular to the global X- and Y-axis respectively in the meantime.

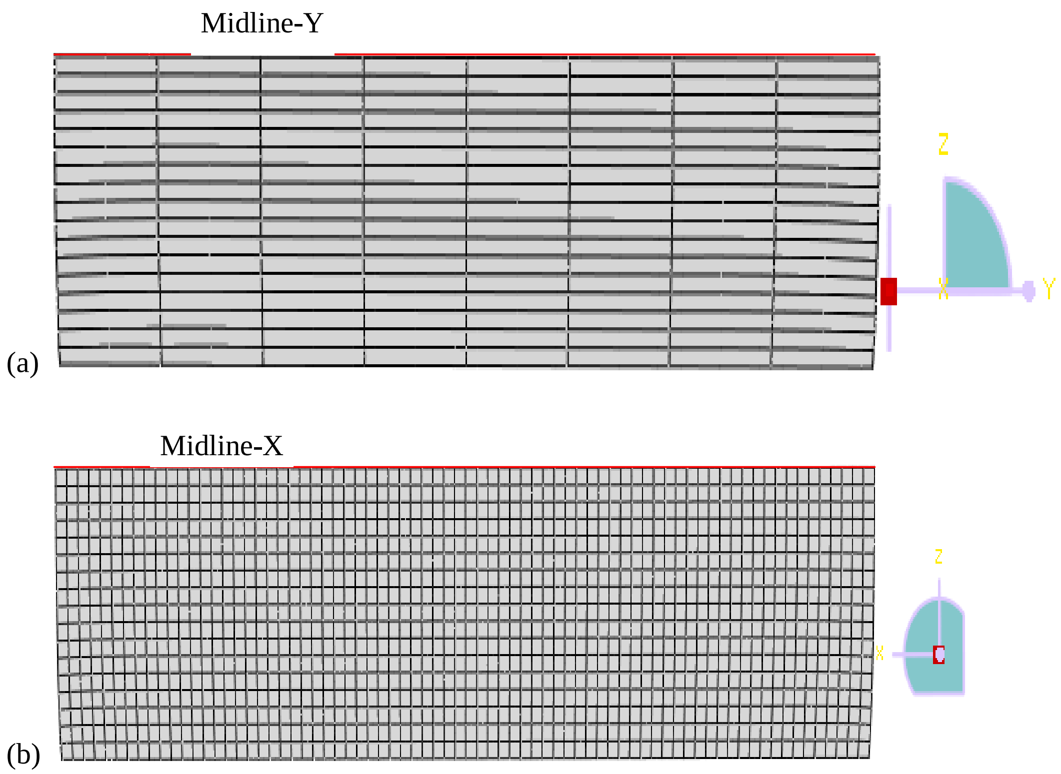

Figure 5.6 The two cross-sections to investigate the distributions of related measurements inside cartilage in the 3D models: (a) the cross-section perpendicular to the global X-axis; (b) the cross-section perpendicular to the global Y-axis.

5.2.7.3 Deformation of the cartilage

The vertical deformation

Similar as in the 2D axisymmetric models of Chapter 4, the vertical deformation of the whole cartilage was set up to be the same in the different 3D models in order to make it reasonable to compare the results. However, the vertical deformation of the top layer elements of the cartilage, which was crucial for the investigation of fluid load support on the cartilage surface, may not be same. The vertical deformation of a specific element was defined as the difference of the axial displacement of the top and bottom vertex of this element. Information from the elements along the two midlines in Figure 5.5

and the four edges of the cartilage surface were recorded and calculated to represent the vertical deformation of the top layer of cartilage.

The radial deformation

In order to compare the radial deformation of cartilage in different 3D models, another two midlines perpendicular to the horizontal surface on the corresponding vertical surface were defined respectively in Figure 5.2 - Midline-X-Z in the global X-Z plane perpendicular to Midline-X and Midline-Y-Z perpendicular to Midline-Y in the global Y-Z plane.

5.3 Modelling Cases

Three dimensional models were set up with different material settings: the realistic fibril orientation model with strain dependent fibrillar Young's modulus (named DT-MRI-3D); the Uniform reinforced model with constant dependent fibrillar Young's modulus (Uniform-3D model); and the basic model with isotropic poroelastic material (Isotropic-3D) - totally three modeling cases. The same geometry, mesh, boundary conditions and loading were used in all of the three models. The material properties employed in these models, including the collagen fibril orientation (except in the Isotropic-3D model), are described in Table 5.1.

The value of the fibril *Young's* modulus on the local *x*-axis, Ef_x, in the Uniform-3D model had been adjusted to 4.0 MPa and $Ef_y = Ef_z = 1.33$ MPa to match the vertical displacement of the cartilage surface centre in the DT-MRI -3D model at the end of the ramp loading stage, in order to make the comparison reasonable. The *Young's* modulus E_m was also adjusted in the

Isotropic model. To provide the information of the cartilage deformation to carry out this adjustment, the DT-3D model was set up first.

Table 5.1 Material properties of different models (ε is the fibrillar strain in each iteration and 4.0 represented 80% interstitial fluid).

Modelling case / Material parameter	DT-MRI - 3D	Uniform-3D	Isotropic-3D
Young's modulus of nonfibrillar matrix, E_m (MPa)	0.52	0.52	1.13
Poisson's ratio of nonfibrillar matrix, v_{m}	0.36	0.36	0.36
Young's modulus of fibril on local x-axis, Ef_x (MPa)	$3+1600\varepsilon_x$	4.0	n/a
Young's modulus of fibril on local y-axis, Ef_y (MPa)	$0.9+480\varepsilon_y$	1.33	n/a
Young's modulus of fibril on local z-axis, Ef_z (MPa)	$0.9+480\varepsilon_z$	1.33	n/a
Permeability, k (m^4/N·s)	3.0×10^{-15}	3.0×10^{-15}	3.0×10^{-15}
Initial void ratio, e_0	4.0	4.0	4.0
Source of fibril orientation	DT-MRI	Manual uniform	n/a

5.3.1 The 3D fibril reinforced model

5.3.1.1 Mechanical property of material

In the DT-3D model, the *Young's* modulus of the fibrillar network was direction dependent and varied linearly with tensile strain but to be zero for compression: $Ef_x = 3 + 1600\varepsilon_x$ MPa; $Ef_y = 0.9 + 480\varepsilon_y$ MPa; $Ef_z = 0.9 + 480\varepsilon_z$ MPa (Ef_x, Ef_y and Ef_z represent modulus in local x, y and z direction respectively), ε_x, ε_y and ε_z is the fibrillar strain in local *x*, *y* and *z* direction as described in Chapter 3. Ef_y and Ef_z were defined to simulate the tensile stiffness of the collagen network produced by the cross-links (Kazemi *et al.*, 2011).

The material property of the nonfibrillar poroelastic matrix was same as the 2D fibril reinforced model except the *Young's* modulus E_m: isotropic with Poisson's ratio ν_m = 0.36, permeability k = 0.003 mm^4/Ns and the initial void ratio e_0 = 4.0 (Li *et al.*, 1999 and 2009). If 0.26 MPa was still used as the value of E_m, the fluid load support was higher than 100% at the end of ramp loading (Figure 5.7) which was unreasonable at several integration points on the Midline-X parallel to the global *X*-axis. When E_m was increased to 0.52 MPa, all of the values of fluid load support were less than 100% (Figure 5.7).

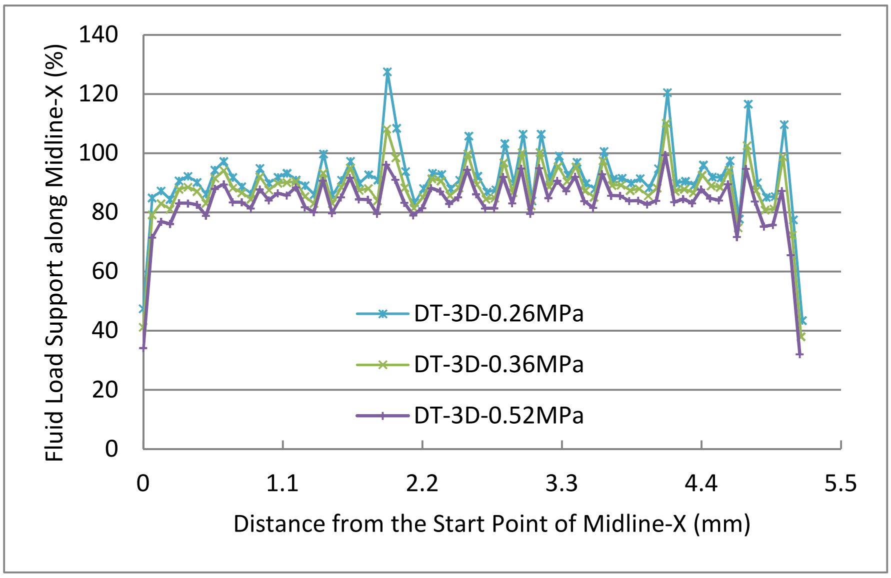

Figure 5.7 Fluid load support along the Midline-X on cartilage surface parallel to the global X-axis in the DT-MRI-3D models with different values of Young's modulus Em of the nonfibrillar at the end of ramp loading (t = 2s).

5.3.1.2 Implementation of fibril orientation

The user-defined “ORIENTATION” including “Distribution” introduced in Section 3.4 was used to incorporate the fibril orientation in the DT-3D model. Part of the detailed input file is displayed below:

```
*DISTRIBUTION TABLE, NAME=tab2
       COORD3D, COORD3D
*DISTRIBUTION, NAME=dist2, LOCATION=element, TABLE=tab2
                            , aX_0,aY_0,aZ_0,bX_0,bY_0,bZ_0
          element set name, X_{17,1}, Y_{17,1}, Z_{17,1},bX_{17,1},bY_{17,1},bZ_{17,1}
          element set name, X_{17,2}, Y_{17,2}, Z_{17,2},bX_{17,2},bY_{17,2},bZ_{17,2}

                          …

          element set name, X_{17,74}, Y_{17,74}, Z_{17,74},bX_{17,74},bY_{17,74},bZ_{17,74}
          element set name, X_{16,1}, Y_{16,1}, Z_{16,1},bX_{16,1},bY_{16,1},bZ_{16,1}

                          …

          element set name, X_{2,74}, Y_{2,74}, Z_{2,74},bX_{1,74},bY_{1,74},bZ_{1,74}
          element set name, X_{1,1}, Y_{1,1}, Z_{1,1},bX_{2,1},bY_{2,1},bZ_{2,1}

                          …

          element set name, X_{1,74}, Y_{1,74}, Z_{1,74},bX_{1,74},bY_{1,74},bZ_{1,74}
*ORIENTATION, NAME=ORI, DEFINITION=COORDINATES
       dist2
```

“Distribution” in the DT-3D model

As introduced in Section 5.2.4, the principal eigenvector of a specific diffusion tensor was defined as the x-axis of the local Cartesian coordinates of the corresponding element set: the three components (Xij, Yij and Zij; i = 1 ··· 17, j = 1 ··· 74) of every single principal eigenvector were implemented to the corresponding element set in Figure 5.2 to represent the fibril orientation in all elements of this set.

Calculation of the coordinates of point b lying on the local y-axis

There were two steps to define the coordinates of the second local point b for each element set in the “Distribution”. Firstly, the three coordinate components of the point (bXij, bYij, bZij; i = 1 ··· 17, j = 1 ··· 74) should be calculated in advance using Formula 3.9. Then, the components were input to the corresponding element set.

5.3.2 The 3D uniformly reinforced model

5.3.2.1 Mechanical property of material

In order to make the vertical displacement at the cartilage surface centre of the 3D uniformly reinforced models match the DT-MRI-3D model at the end of the ramp loading stage, the values of the fibril Young’s modulus on the local axes in this model had been adjusted (Figure 5.8) while the other material parameters in Table 5.1 remained unchanged.

In Figure 5.8, only the curve of the Uniform-3D model with 4.0 MPa fibril *Young’s* modulus Ef_x (and 1.33 MPa for Ef_y and Ef_z) could match the vertical displacement of the cartilage surface of the DT-MRI-3D model at t = 2s. The other material parameters in this model (Table 5.1) were same as the DT-MRI-3D model. The user-defined subroutine “UMAT” was still used in this model, although the *Young’s* modulus was constant.

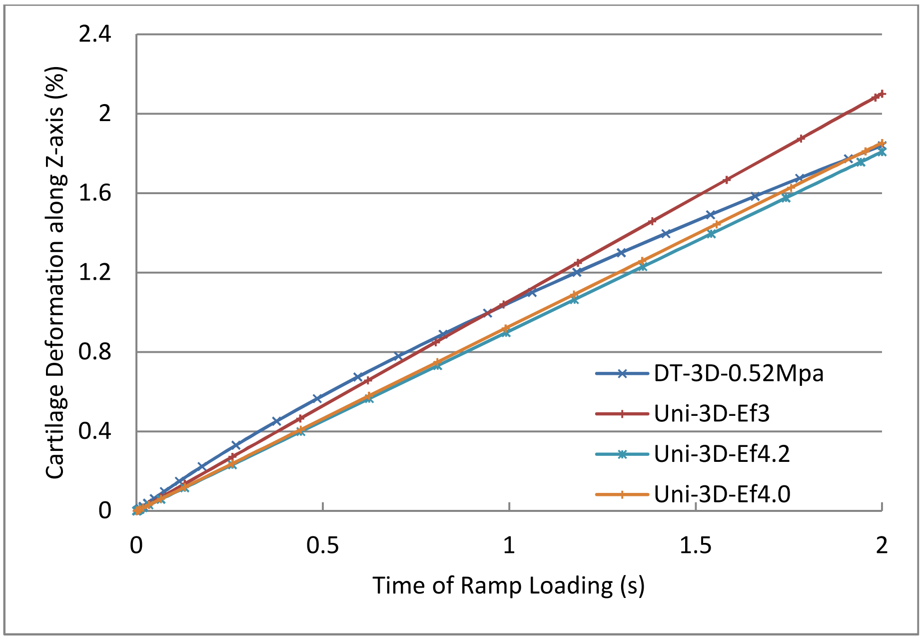

Figure 5.8 Adjustments of Young's modulus in the Uniform-3D model to achieve the same axial displacement of cartilage surface centre as DT-MRI-3D model at the end of ramp loading (t = 2s).

5.3.2.2 Definition of the local coordinate system

Similar as the 2D uniformly reinforced models in Section 4.3, no specific orientation of collagen fibrils were implemented this 3D uniformly reinforced model. The local Cartesian coordinate in each element was defined to be the same as the global system. This effectively aligned the fibril orientation with the global X-axis. Each element was given an equal, maximum reinforcement in the local x-direction when the material model was modified based on this orientation.

Instead of the user-defined "ORIENTATION" including "Distribution" in Section 3.3, the 'Keyword' method was used to define the local system by specifying the locations of points a and b directly (Abaqus Analysis User's Manual 2.2.5). The detailed input file in this model to define the local

Cartesian coordinate was the same as the one used in the 2D uniformly reinforced models in Section 4.3:

```
*Orientation, name=Ori-1, DEFINITION=COORDINATES, SYSTEM=RECTANGULAR
1.0, 0.0, 0.0, 0.0, 1.0, 0.0
```

5.3.3 The isotropic poroelastic model

In order to produce the comparable results, the value of Young's modulus E in Table 5.1was increased to 1.13MPa from 0.69MPa in Section 5.2 (Mononen et al., 2010) while the other material parameters remained. This adjustment made the vertical deformation of the cartilage surface centre in the Isotropic-3D model match the DT-MRI-3D model at the end of the ramp loading stage (Figure 5.9).

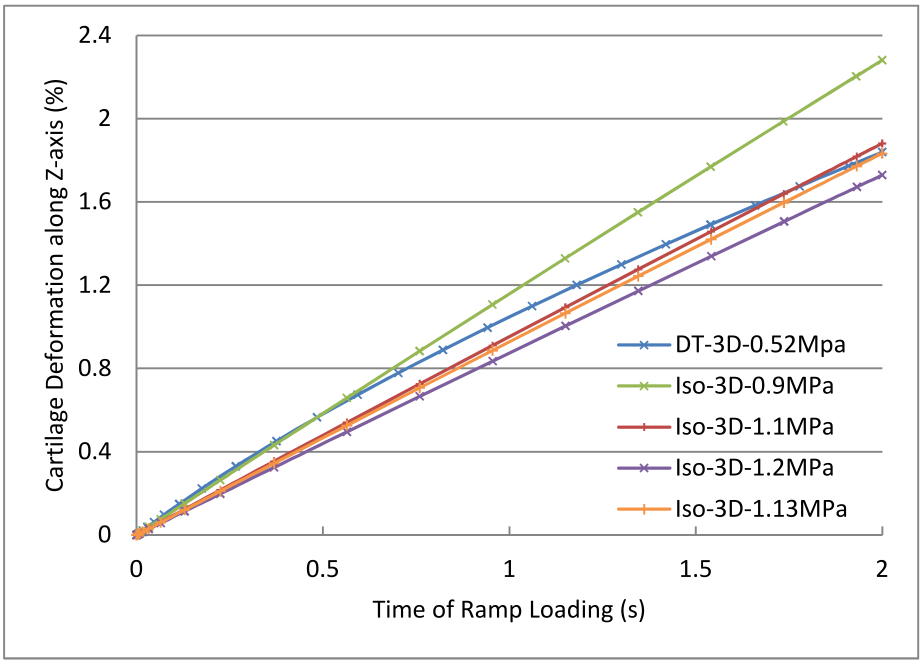

Figure 5.9 Adjustments of Young's modulus in the Isotropic-3D model to achieve the same axial displacement of cartilage surface centre as the DT-MRI-3D model at the end of ramp loading (t = 2s).

5.4 Validation of the 3D DT-MRI based model

The MRI experimental data used in this project was generated from tests performed by Robin Damon (School of Physics, University of Leeds), a creep test (unconfined compression) were carried out on the cartilage sample for 37.5 minutes under 0.2 MPa pressure after the acquirement of the diffusion tensor, using a 9.5T MRI machine in the School of Physics and Astronomy. Cartilage thickness was recorded during the loading period. The measurement was performed using the AnalyzeTM image analysis software.

According to the experimental record, the initial cartilage thickness was 1355μm (slightly thinner that the result of 1.36 mm in Fermor et al., 2013). This is not consistent with the corresponding data in the 3D DT-MRI model which was 1190μm. In order to validate the 3D DT-MRI model, the data of cartilage thickness was transformed to the information of the vertical displacement of cartilage surface i.e. the vertical cartilage deformation and normalized. The original deformation value at a specific time of the cartilage sample was defined as the difference between the initial value and the value corresponding to this time in the thickness record. Then the deformation values were normalized as a percentage i.e. divided by the initial thickness of cartilage (1355μm). Finally, the curve of the normalized vertical displacement of cartilage surface during the creep test was produced (Figure 5.10).

In Figure 5.10, the vertical deformation of the cartilage sample did approach the equilibrium which was slightly higher than 18% at the last stage of the creep test. The validation of the DT-MRI-3D model was carried out by curve-fitting this experimental result.

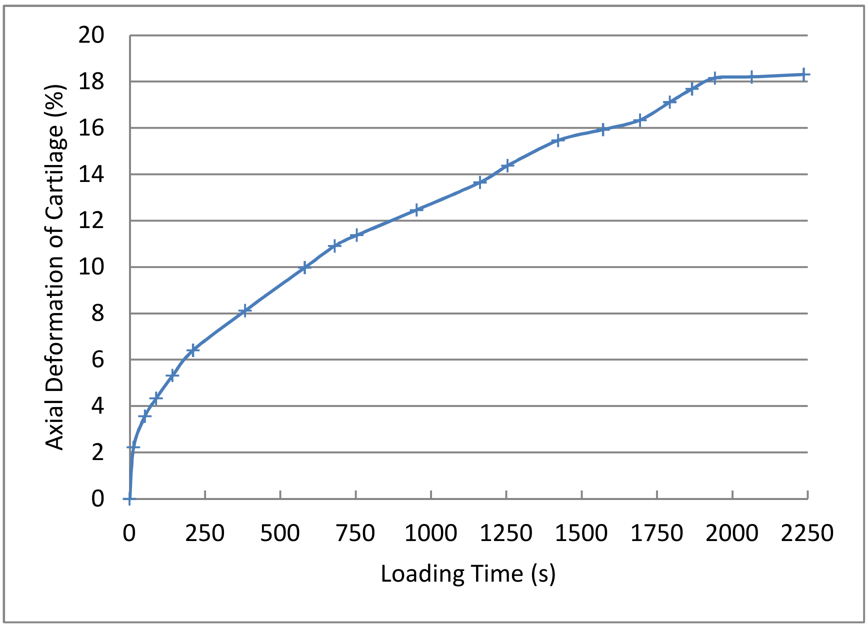

Figure 5.10 Normalized vertical displacements (%) of cartilage surface in the creep test.

In order to perform the validation, the value of the Young's modulus of the nonfibrillar matrix Em in the DT-MRI-3D model (Table 5.1) was increased to enable the cartilage to support the higher applied load equivalent to the applied pressure (0.2 MPa) in the experiment.

As the permeability k used in the previous models in this thesis was 3.0×10-15 m4/(N·s) which was cited from Li et al. (2009). This value was in the typical range of ~ 0.1-10×10−15 m^4/(Ns) for permeability of articular cartilage (Chen et al., 2001; Frank et al., 1987; Jurvelin et al., 2003; Mow et al., 1984). However, the permeability of cartilage from bovine groove was determined as 0.663×10−15 m4/(Ns) according to the latest measurement of Fermor et al. (2013). So the value of permeability was also adjusted to investigate its effects on the modelling results of cartilage deformation and the curve-fitting of the experimental data.

5.5 Results

The results from different modelling cases described in Section 5.3 are collected and compared to each other in the first subsection. The validation results are displayed separately in the second subsection.

5.5.1 Comparison of results from different 3D models

5.5.1.1 Contact pressure, pore pressure and fluid load support on the cartilage surface

Comparison of contact pressure along midlines of the cartilage surface

The value of contact pressure was highest in the central parts of the midlines and decreased to the parts near the edges in all of the three models (Figure 5.11), while the curve along Midline-X of the DT-MRI-3D model fluctuated frequently (Figure 5.11(a)). The Isotropic model had the highest values along Midline-Y (Figure 5.11 (b)).

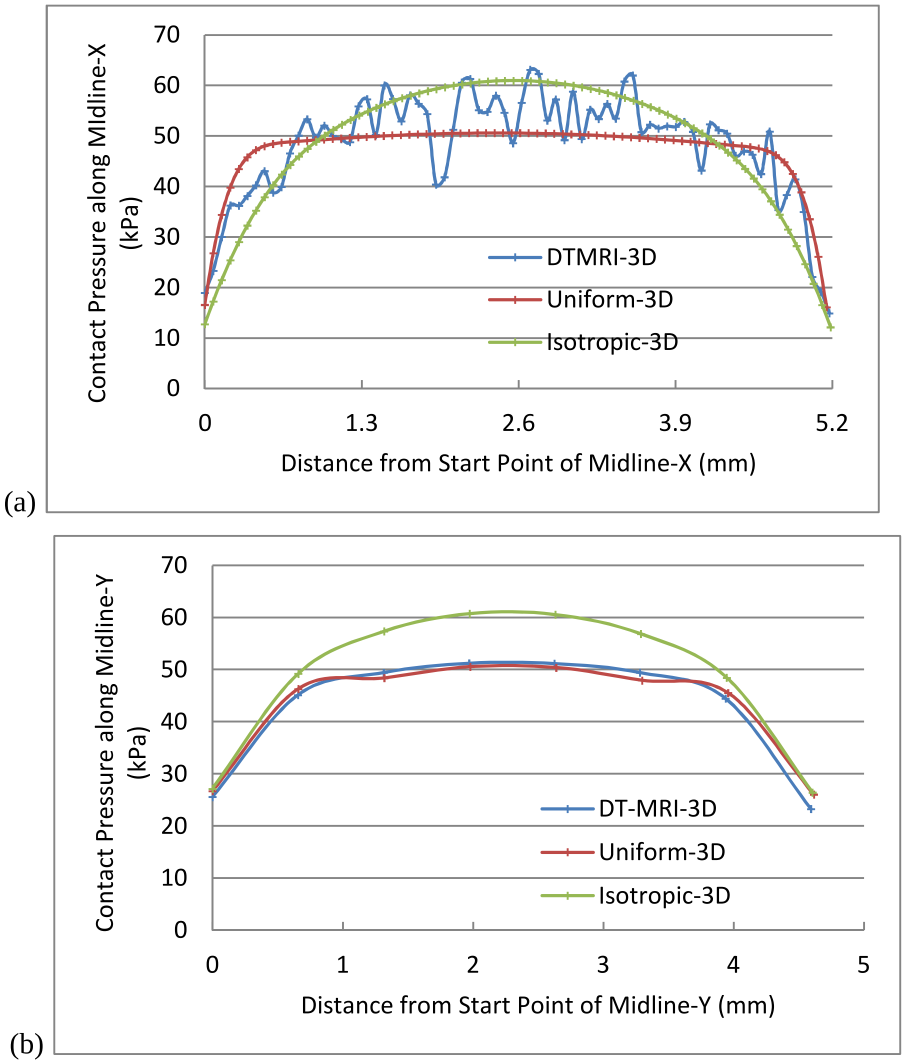

Figure 5.11 Comparison of contact pressure on the cartilage surface along (a) Midline-X and (b) Midline-Y at the end of ramp loading (t = 2s).

Comparison of pore pressure along midlines of the cartilage surface

Similar as the distribution of contact pressure, the value of pore pressure was also higher in the central parts of the midlines than in the parts aside while the curves of the Isotropic-3D model were lowest along both midlines (Figure 5.12). The curves of the DT-MRI-3D model had the highest values although fluctuated along Midline-X (Figure 5.12 (a)).

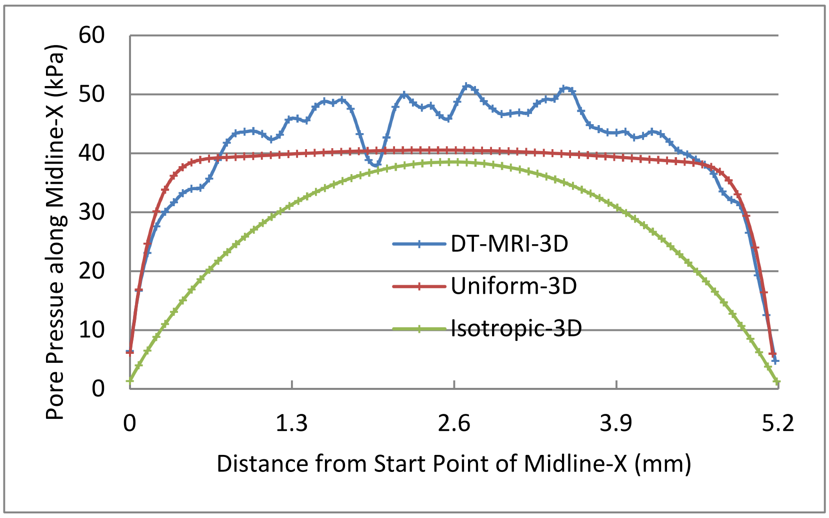

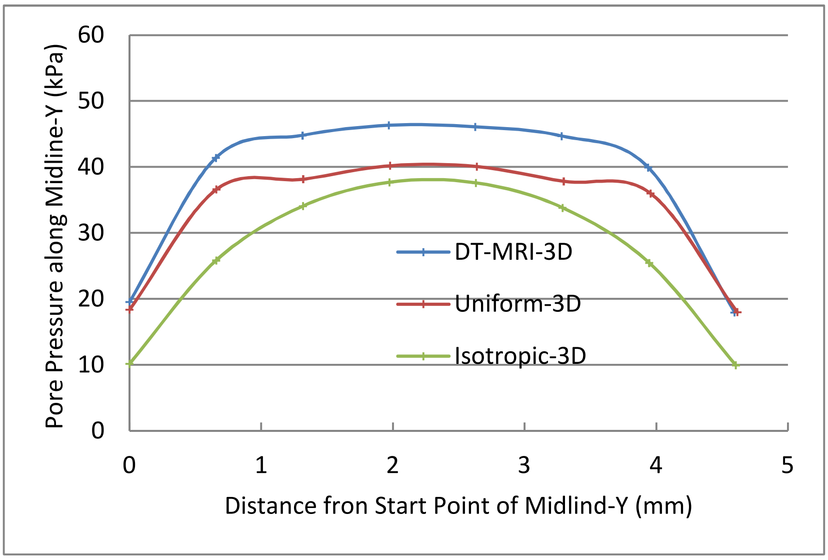

Figure 5.12 Comparison of pore pressure on the cartilage surface along (a) Midline-X and (b) Midline-Y at the end of ramp loading (t = 2s).

Comparison of fluid load support along midlines of the cartilage surface

Except on the limited number of points along Midline-X, the values of fluid load support of the DT-MRI-3D model were higher than the corresponding value of the other two models as expected (Figure 5.13 (a)). The curves of the Isotropic-3D were the lowest with values less than 65% (Figure 5.13).

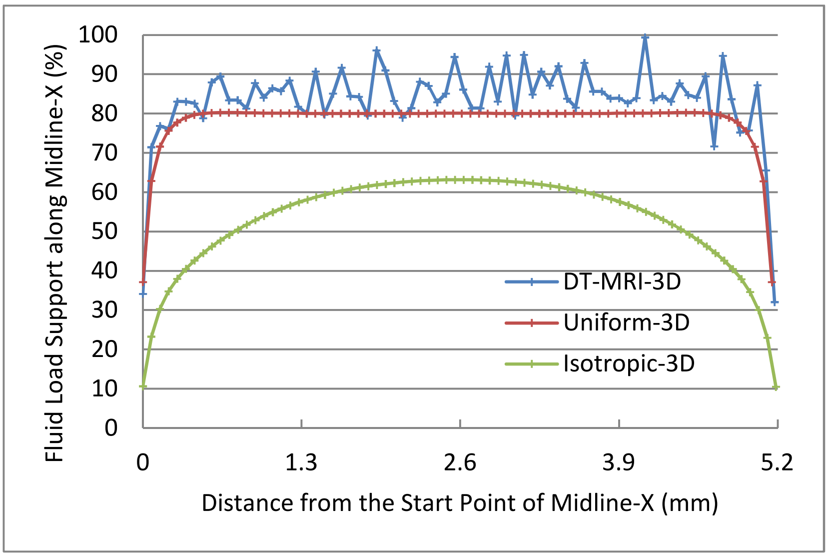

(a)

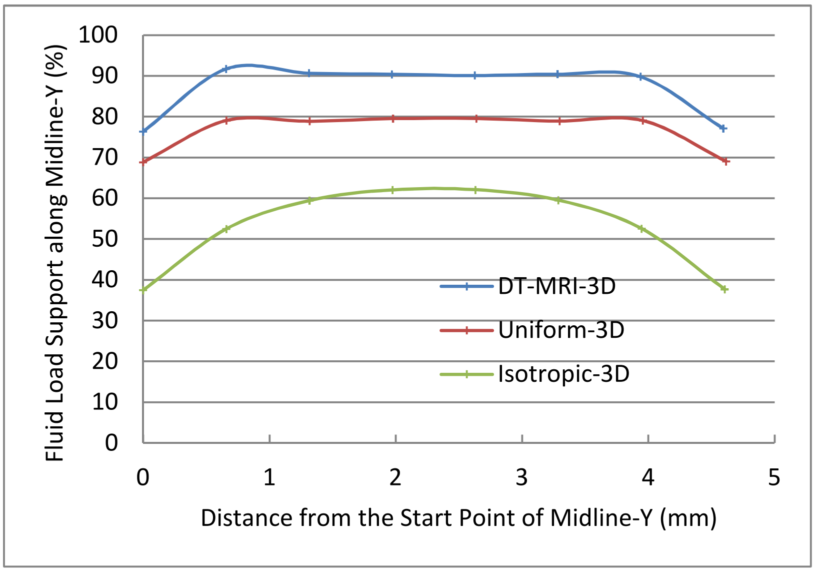

(b)

Figure 5.13 Comparison of fluid load support on the cartilage surface along (a) Midline-X and (b) Midline-Y at the end of ramp loading (t = 2s).

Distribution of contact pressure on the cartilage surface

Calculated only on the integration points of the reduced hexahedral element, contact pressure distributed discontinuously with the higher values at the central area of the cartilage surface and decreased to the region near the edges in all of the three models (Figure 5.14).

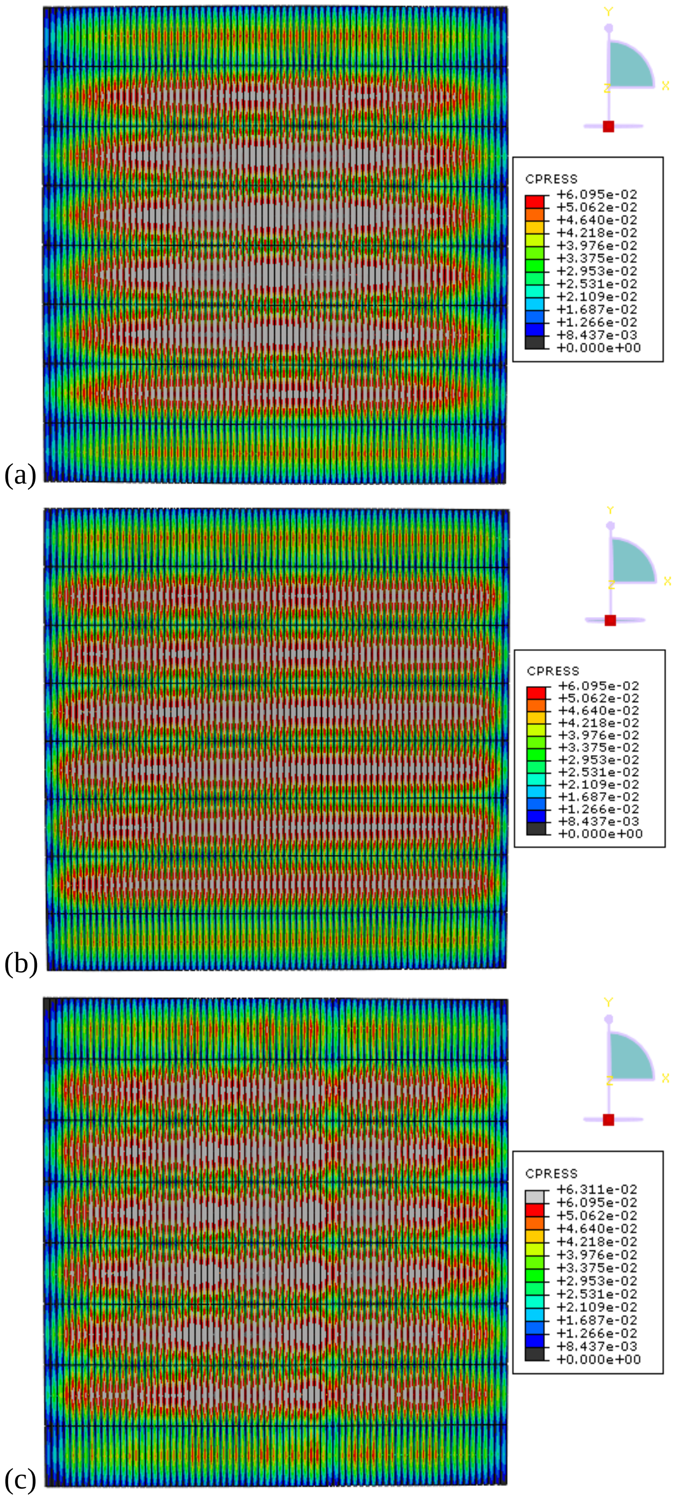

Figure 5.14 Contour of contact pressure (MPa) on the cartilage surface of (a) the Isotropic-3D, (b) the Uniform-3D and (c) the DT-MRI-3D model at the end of ramp loading (t = 2s).

Distribution of pore pressure on the cartilage surface (Figure 5.15)

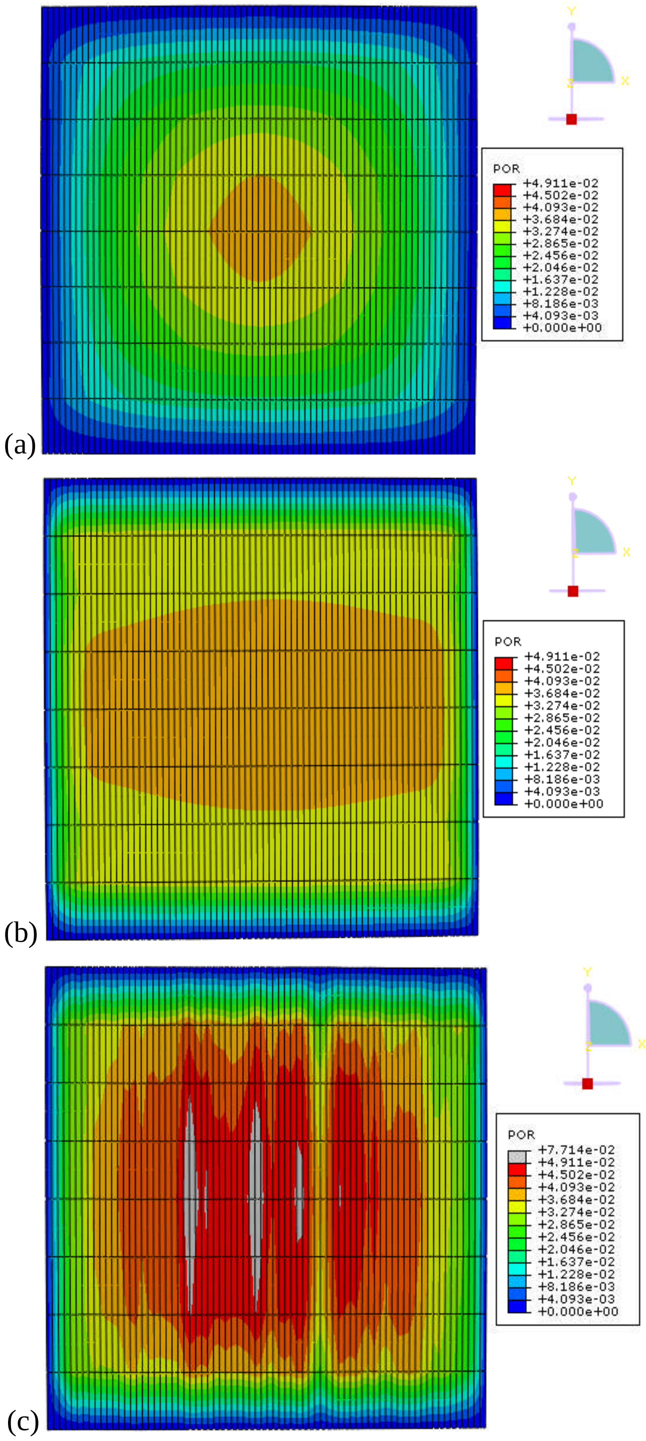

Figure 5.15 Contour of pore pressure (MPa) on the cartilage surface of (a) the Isotropic-3D, (b) the Uniform-3D and (c) the DT-MRI-3D at the end of ramp loading (t = 2s).

The region with higher pore pressure around the cartilage surface centre was much smaller in the Isotropic-3D model than in the Uniform-3D model (brown area in Figure 5.15 (a) and (b)). Only in the DT-MRI-3D model, the highest values of pore pressure emerged on the cartilage surface (central region with grey and red colour in Figure 5.15 (c)).

Inside distribution of pore pressure on the cross-section of cartilage perpendicular to the global X-axis

The highest value of pore pressure arose at different position of the cartilage bottom in the three models (Figure 5.16). Different from the two simpler models, the pore pressure with the second highest value also emerged from the middle zone to the surface of cartilage (the upper red area in Figure 5.16 (c)) in the DT-MRI-3D model.

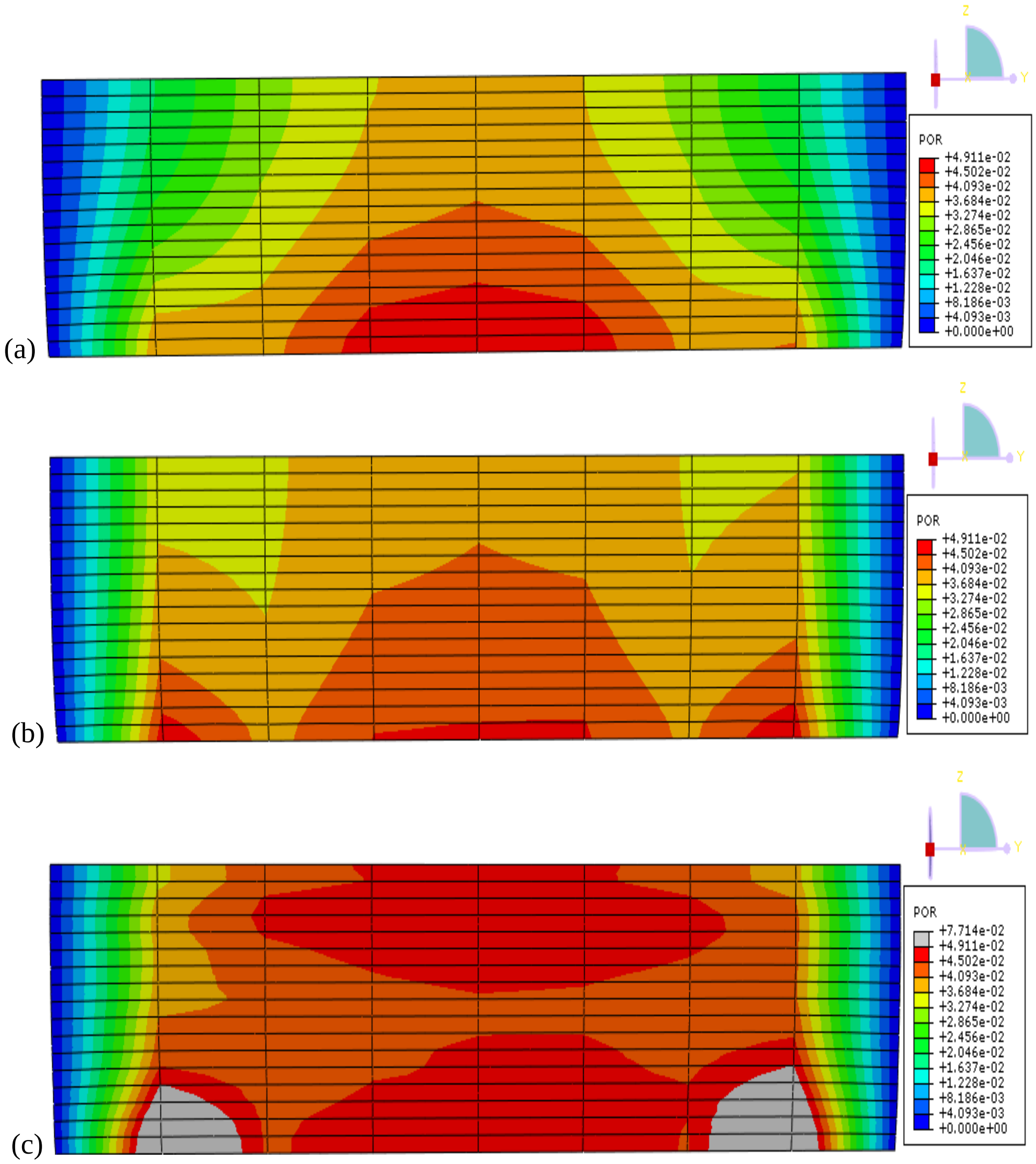

Figure 5.16 Contour of pore pressure (MPa) on the cross-section perpendicular to the global X-axis (out of the page) of (a) the Isotropic-3D, (b) the Uniform-3D and (c) the DT-MRI-3D model at the end of ramp loading (t = 2s).

Inside distribution of pore pressure on cross section of cartilage perpendicular to the global Y-axis (Figure 5.17)

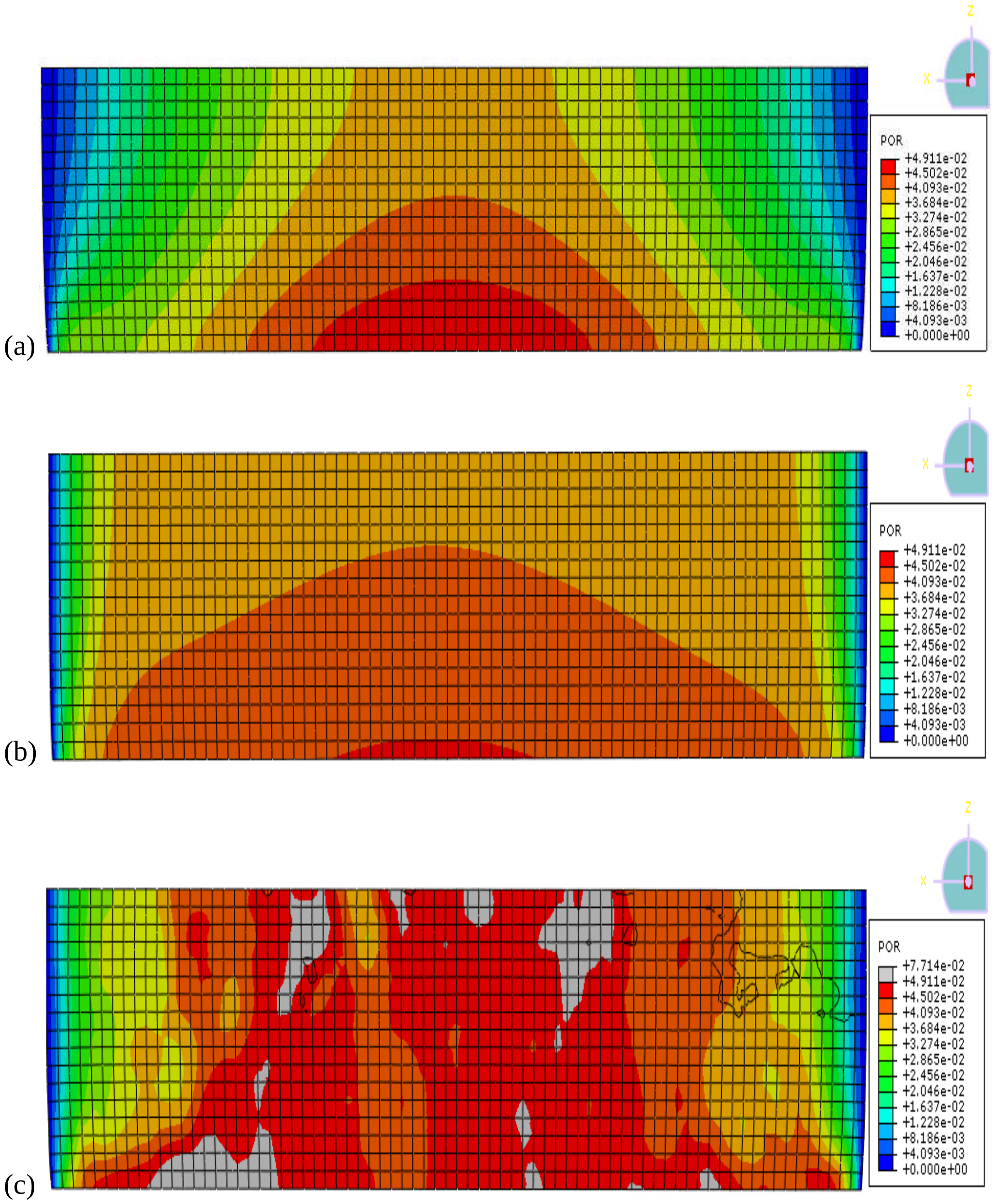

Figure 5.17 Contour of pore pressure (MPa) on the cross-section perpendicular to the global Y-axis (out of the page) of (a) the Isotropic-3D, (b) the Uniform-3D and (c) the DT-MRI-3D model at the end of ramp loading (t = 2s).

In the Isotropic-3D and Uniform-3D model, the highest value of pore pressure only arose around the centre of cartilage bottom (red region in Figure 5.17 (a) and (b)). But in the DT-MRI-3D model, the highest pore pressure also distributed in the whole central area of the tissue from the surface to the bottom (grey and red region in Figure 5.17 (c)).

Contact pressure, pore pressure and fluid load support at cartilage surface centre during the loading period

Although the peak values of contact pressure were similar in the three models, the peak pore pressure was much higher in the DT-MRI-3D model than in the other two models leading to the highest peak fluid load support (Figure 5.18). The pore pressure and fluid load support decreased similarly after ramp load and tended to zero while the load was maintained.

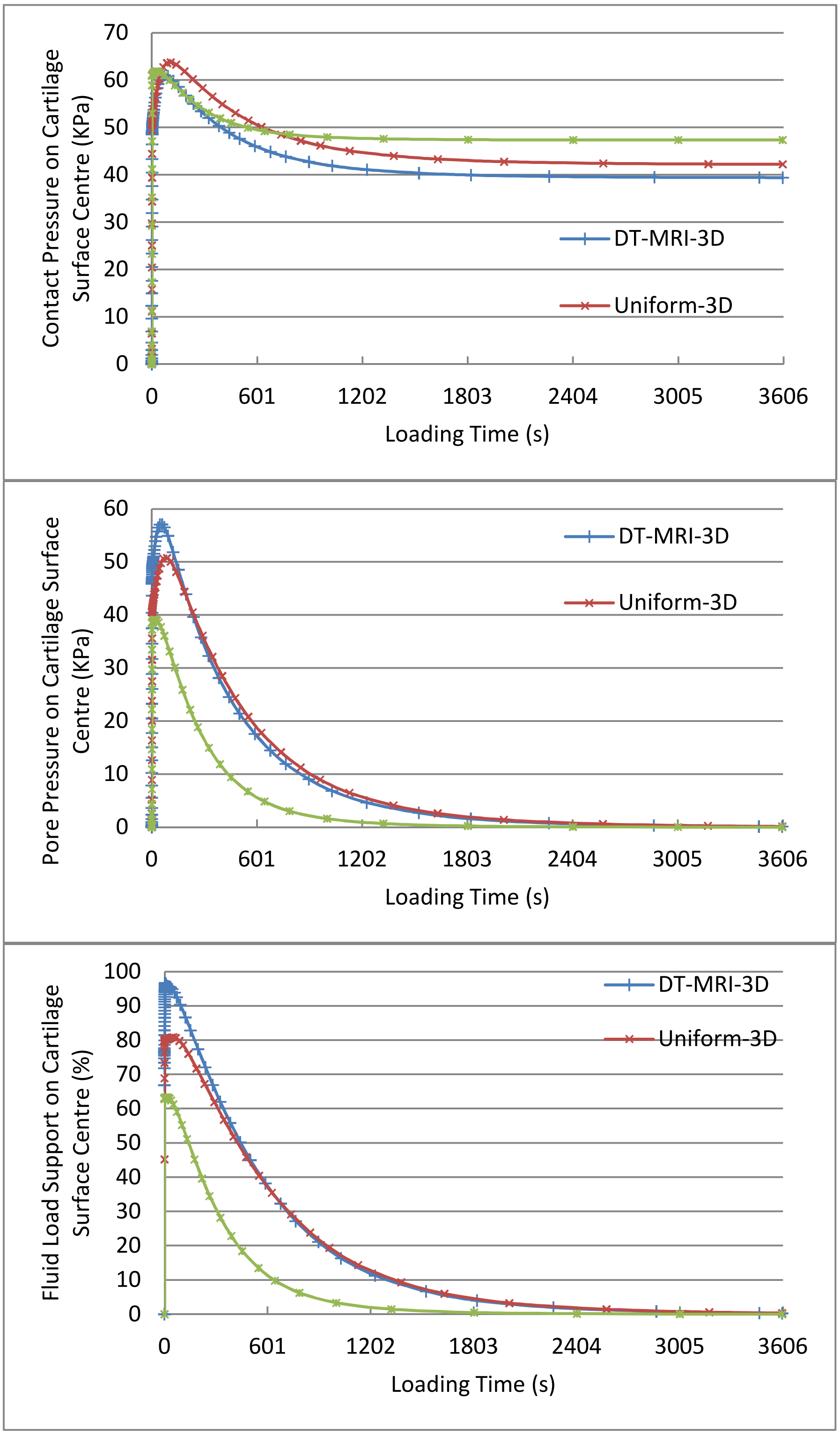

Figure 5.18 Comparison of fluid load support at cartilage surface centre during the loading period (t = 3602s).

5.5.1.2 Distribution of fluid velocity

Distribution of fluid velocity on the vertical outer sides surfaces of cartilage (Figure 5.19)

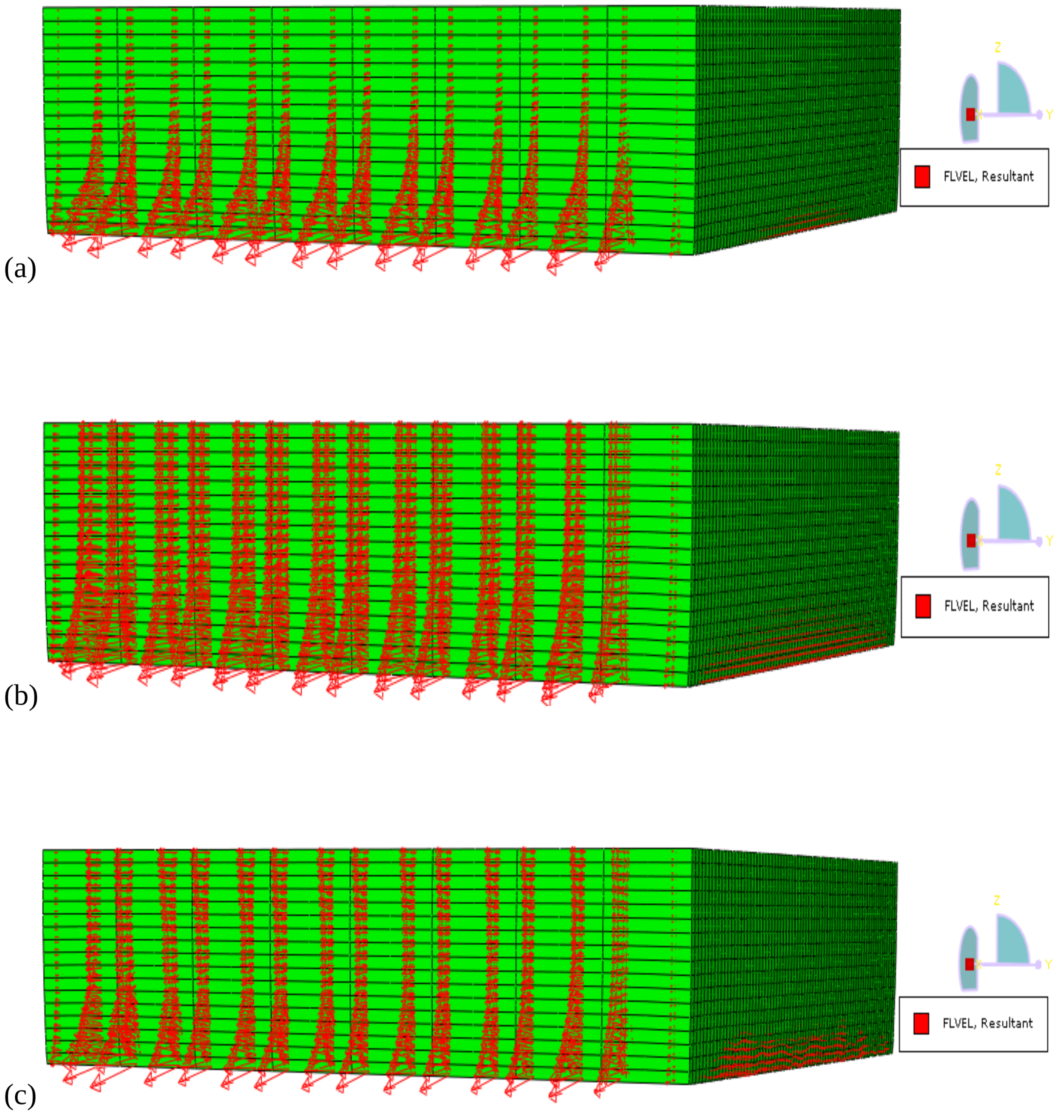

Figure 5.19 Distribution of fluid velocity (mm/s) on the vertical outer sides of cartilage in (a) the Isotropic-3D, (b) the Uniform-3D and (c) the DT-MRI-3D model at the end of ramp loading (t = 2s).

On the vertical sides perpendicular to the global X-axis, the Unifrom-3D model had the largest fluid velocity (Figure 5.19 (b)); the Isotropic-3D model had similar distribution near the cartilage bottom as the DT-MRI-3D model but less magnitude from the middle area to the cartilage surface (Figure 5.19 (a) and (c)). On the two vertical sides perpendicular to the global Y-axis, fluid flew out only near the bottom of the tissue while increasing with the complexity of the material, although the magnitude was much lower than that on the adjacent sides (Figure 5.19).

Inside distribution of fluid velocity on the cross section of cartilage perpendicular to the global X-axis

In each individual model in Figure 5.20, the distribution of fluid velocity decreased from the outer edges to the central part of the cross section of cartilage perpendicular to the global X-axis. Compared to the other two models, the Unifrom-3D model had the lowest inside fluid velocity on the section (Figure 5.20).

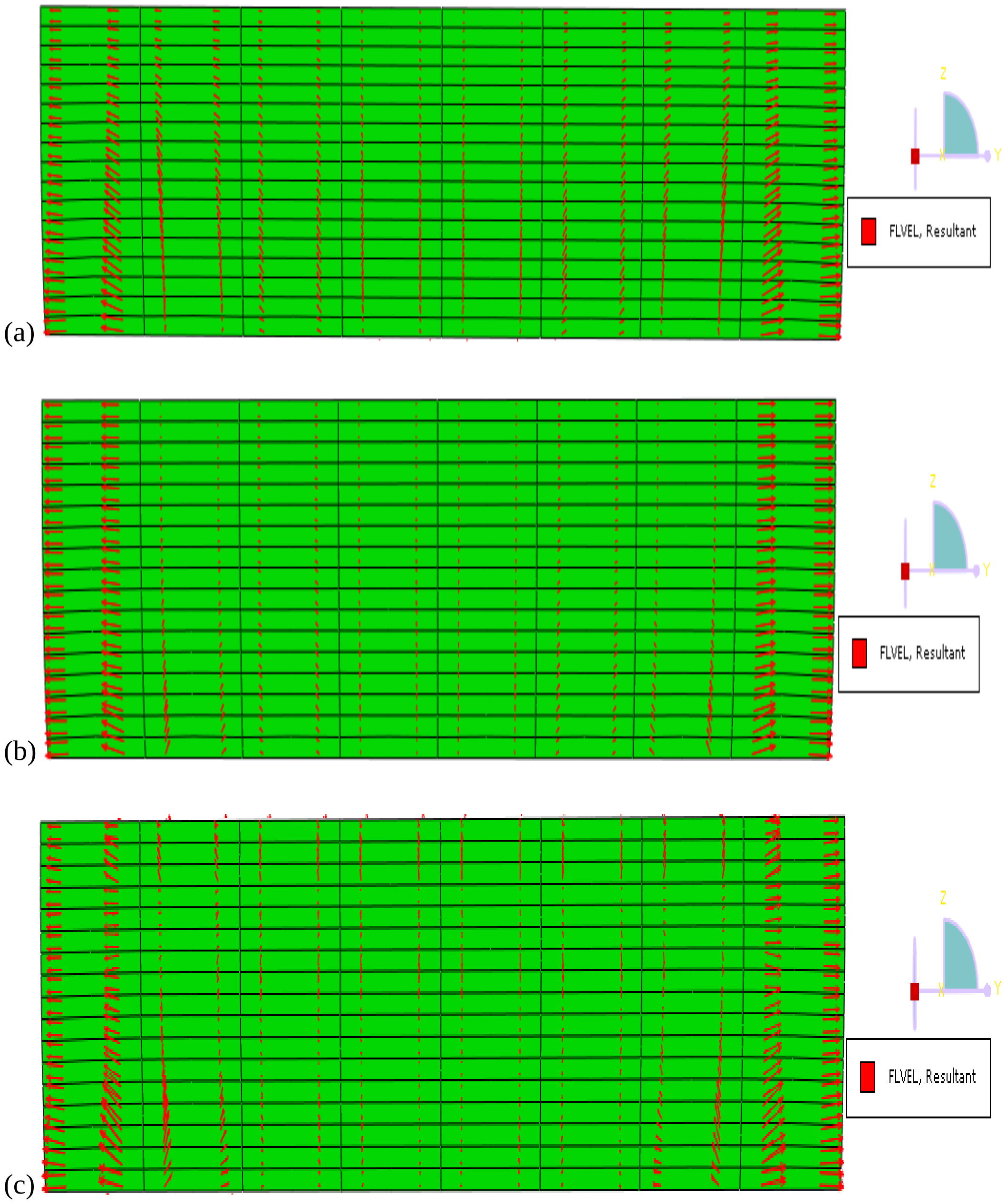

Figure 5.20 Distribution of fluid velocity (mm/s) on the cross-section perpendicular to the global X-axis (out of the page) of (a) the Isotropic-3D, (b) the Uniform-3D and (c) the DT-MRI-3D model at the end of ramp loading (t = 2s).

Inside distribution of fluid velocity on the cross section of cartilage perpendicular to the global Y-axis (Figure 5.21)

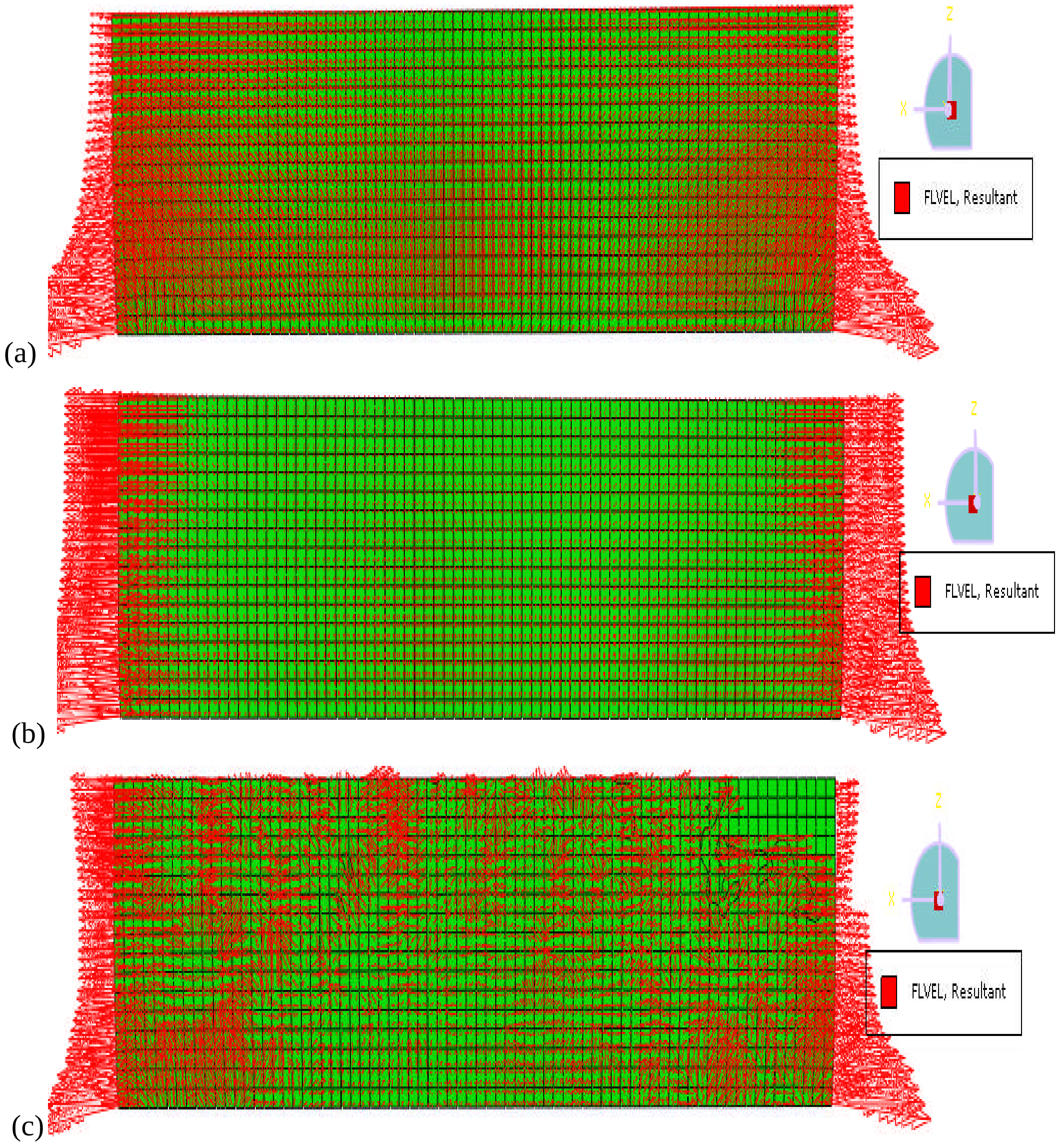

Figure 5.21 Distribution of fluid velocity (mm/s) on the cross-section perpendicular to the global Y-axis (out of the page) of (a) the Isotropic-3D, (b) the Uniform-3D and (c) the DT-MRI- 3D model at the end of ramp loading (t = 2s).

The Unifrom-3D model also had the lowest inside fluid velocity on the cross section of cartilage perpendicular to the global Y-axis (Figure 5.21 (b)). Fluid velocity inside the Isotropic model distributed much more regularly in contrast to the disorder distribution in the DT-MRI-3D model (Figure 5.21 (a) and (c)).

5.5.1.3 Deformation of the cartilage

Radial deformation of cartilage along Midline-X-Z and Midline-Y-Z (Figure 5.22)

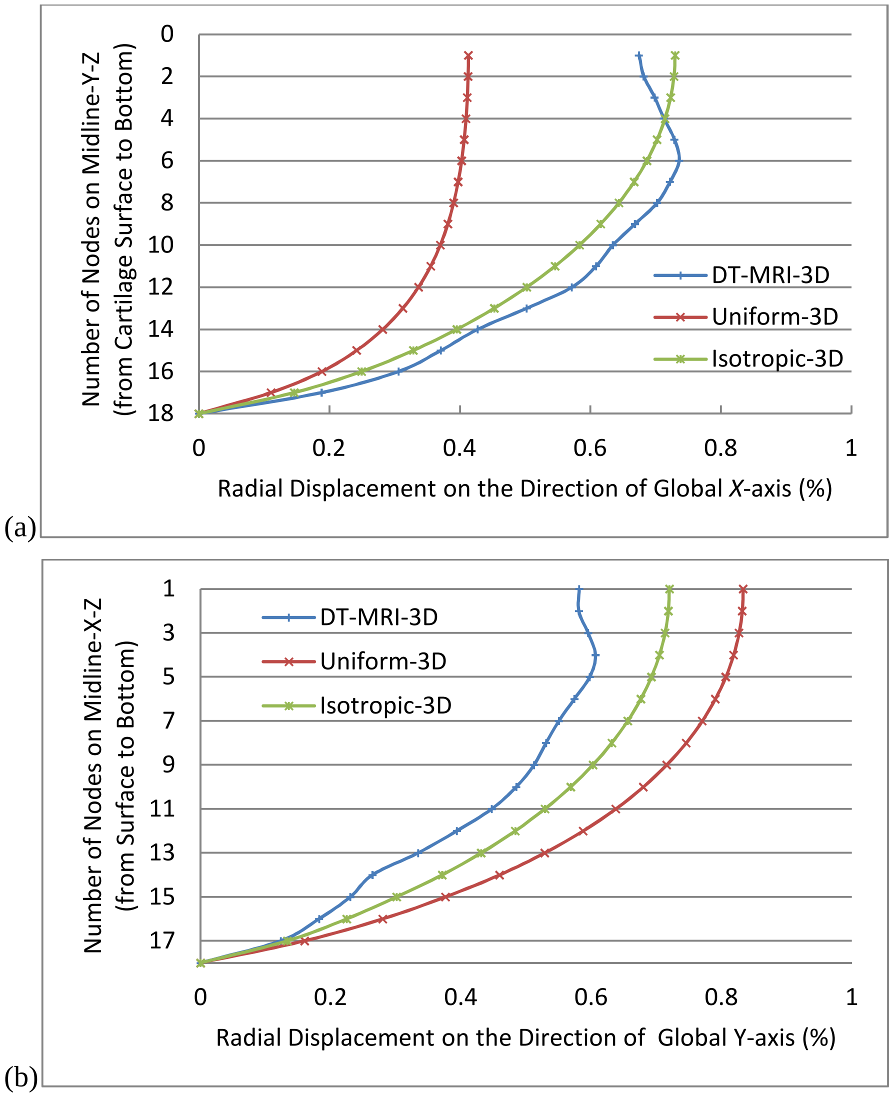

Figure 5.22 Comparison of radial deformation of cartilage on the direction of (a) global X-axis and (b) global Y-axis at the end of ramp loading (t = 2s).

For the DT-MRI-3D model, radial displacement along the global X-axis of points on Midline-Y-Z was higher than the value of the corresponding points in the Uniform-3D model (Figure 5.22 (a)); but the values along the global Y-axis on Midline-X-Z were lower than the Uniform-3D model (Figure 5.22 (b)).

Vertical deformation of cartilage layers along Midline-X-Z and Midline-Y-Z (Figure 5.23)

Along both Midline-X-Z and Midline-Y-Z, the vertical deformation of the first cartilage layer in the DT-MRI-3D model was larger than in the other two models (Figure 5.23). The curves in this figure only represented the information of the central region of cartilage and were not enough to investigate the effect on the interstitial fluid pressurization in the whole first layer of cartilage. More data on the vertical deformation of the first cartilage layer were collected below, along the two midlines and edges of the cartilage surface.

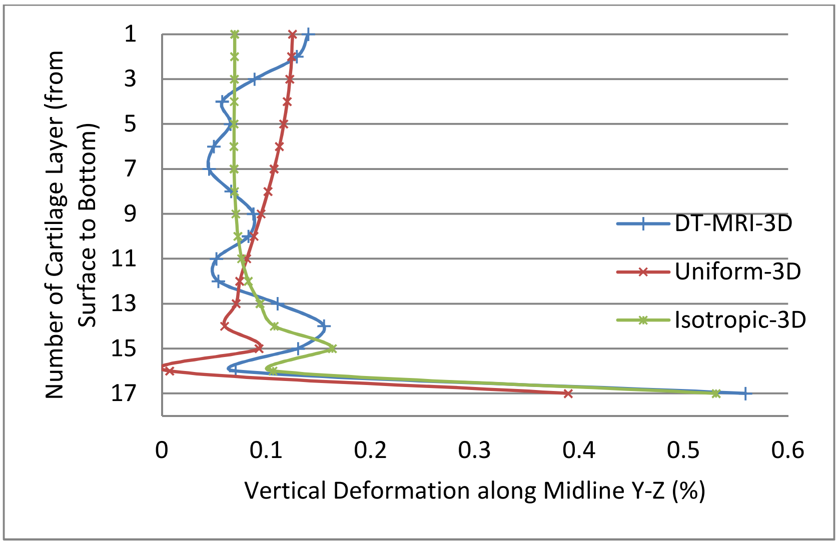

(a)

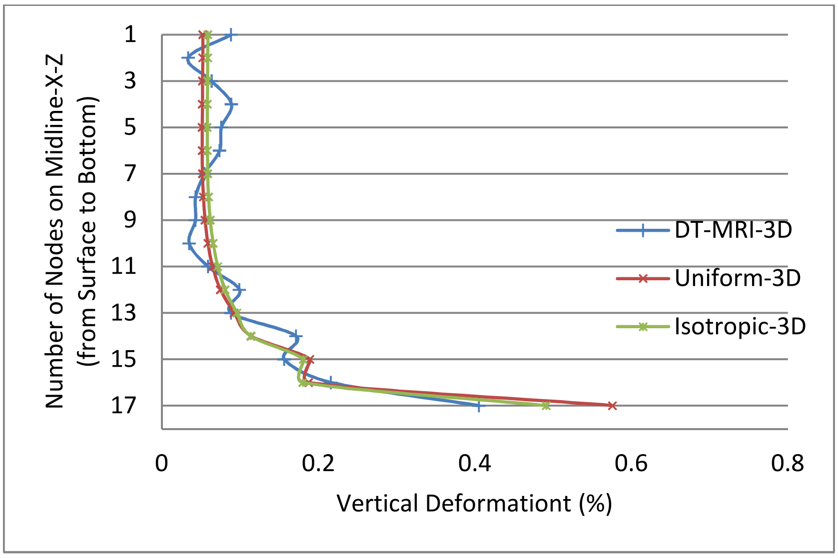

(b)

Figure 5.23 Comparison of vertical deformation of cartilage layers along (a) Midline-Y-Z and (b) Midline-X-Z at the end of ramp loading (t = 2s).

The vertical deformation of elements along Midline-X and the two cartilage surface edge in global X-Z plane (Figure 5.24; next page).

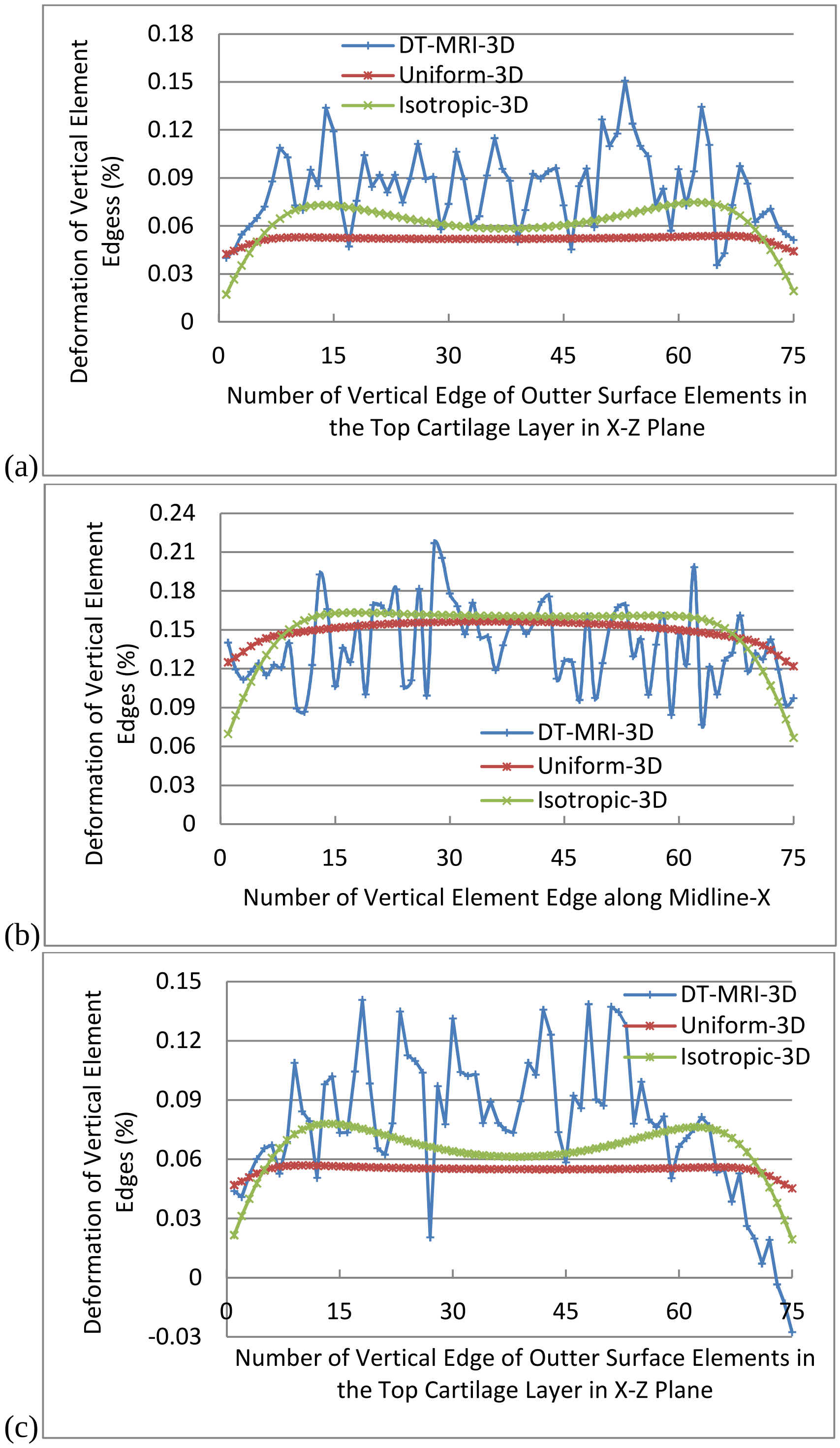

Figure 5.24 Comparison of vertical deformation of elements along Midline-X and the two cartilage surface edge in global X-Z plane at the end of ramp loading (t = 2s).

For the DT-MRI-3D model, the deformation of the vertical edges of most elements was apparently higher along both of the cartilage surface edges in global X-Z plane (Figure 5.24 (a) and (c)) but lower than in the other two models along Midline-X (Figure 5.24 (b)).

Vertical deformation of elements along Midline-Y and the two cartilage surface edge in global Y-Z plane

The deformation of the vertical edges of elements along Midline-Y was similar nearly coincide in the three models; and the differences between the values in the DT-MRI-3D and Uniform-3D model were not so apparent small (Figure 5.25) as those in Figure 5.24.

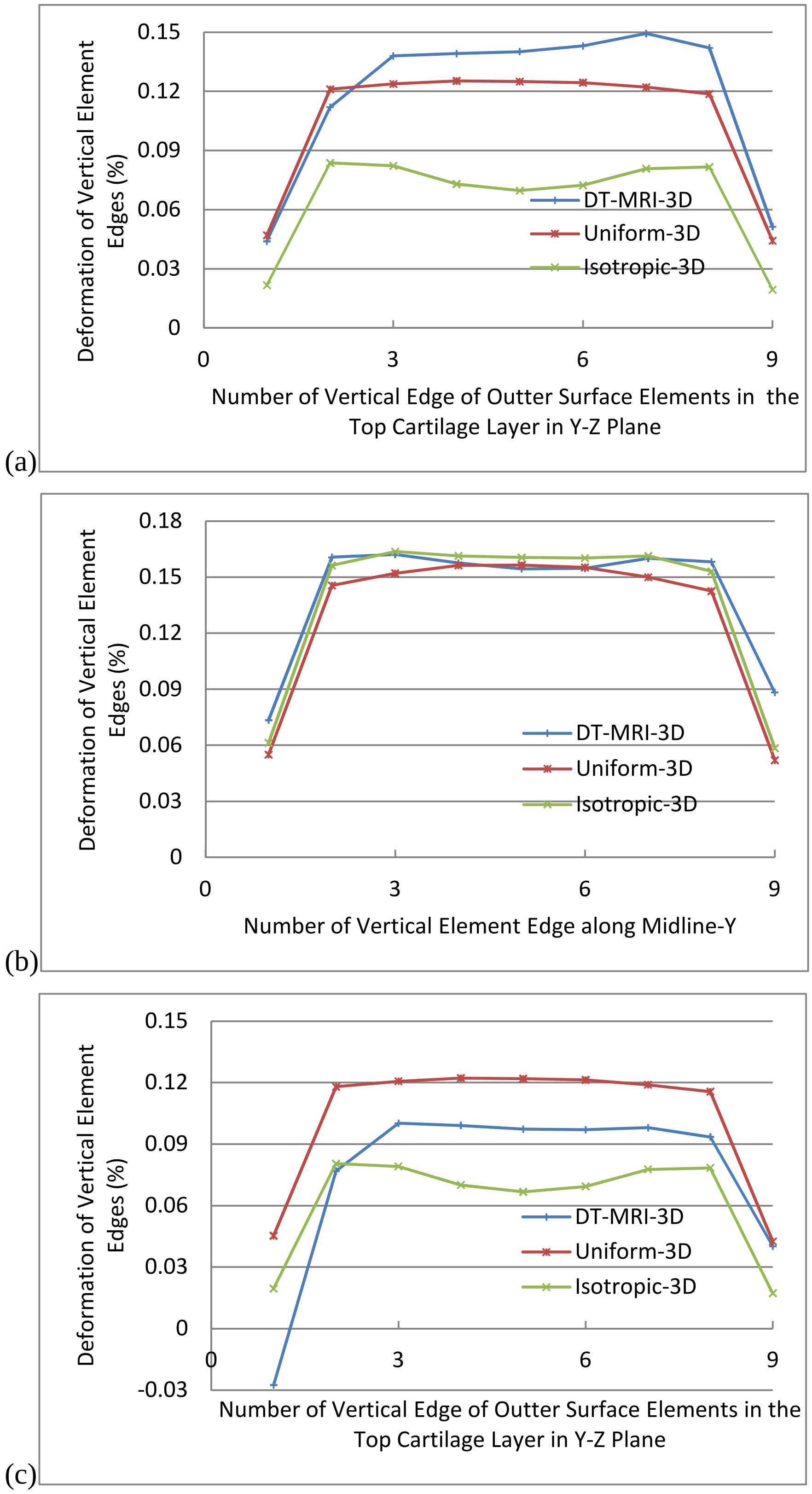

Figure 5.25 Comparison of vertical deformation of cartilage layers in global Y-Z plane at the end of ramp loading (t = 2s).

Vertical displacement of cartilage surface centre during loading period

The normalized vertical displacement of cartilage surface centre was compared across three models during the full loading period (Figure 5.26). After one hour’s creep all models had reached equilibrium.

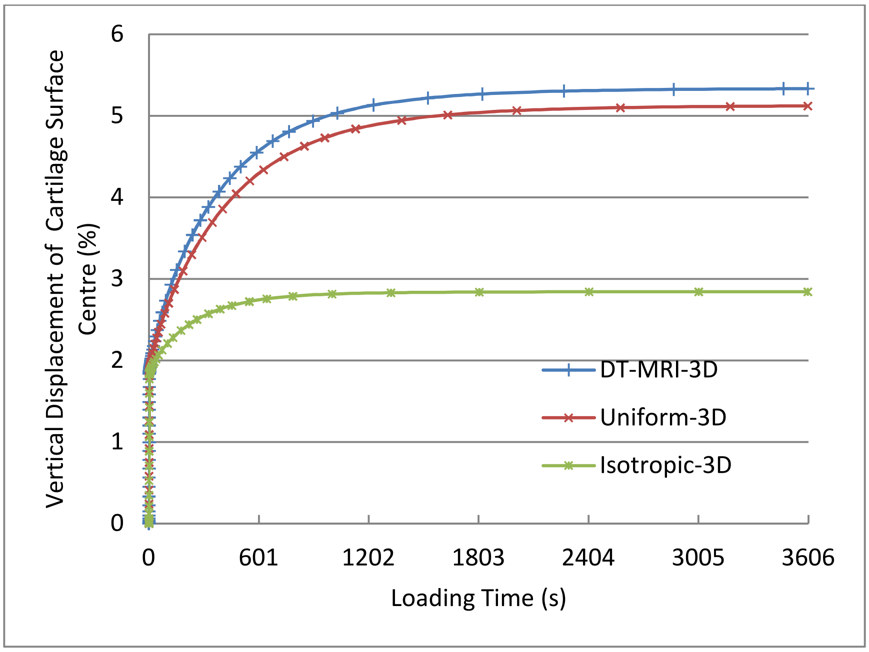

Figure 5.26 Comparison of vertical displacement of cartilage surface centre during loading period.

5.5.1.4 Stress on the cartilage surface

Stress along Midline-X (S_{11}) and Midline-Y (S_{22})

The highest values of stress (S_{11}) along Midline-X of cartilage surface distributed in the central area and decreased to the parts near the edges in all of the three models, although the curve in the DT-MRI-3D model fluctuated severely (Figure 5.27(a)). The value of stress along Midline-Y (S_{22}) increased with the complexity of the material (Figure 5.27(b)).

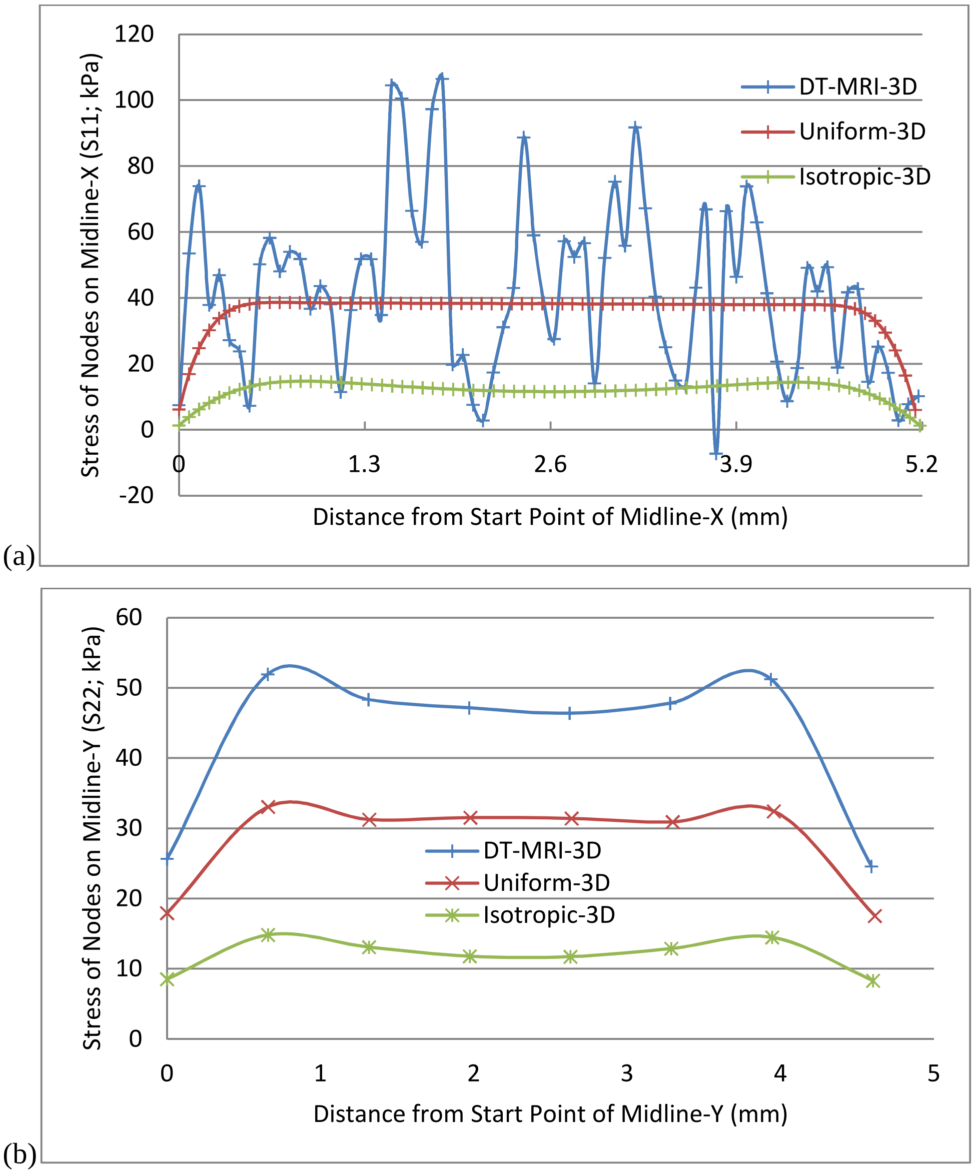

Figure 5.27 Comparison of stress: (a) S_{11} (kPa) along Midline-X and (b) S_{22} (kPa) along Midline-Y at the end of ramp loading (t = 2s).

Stress along global X-axis (S_{11}) and Y-axis (S_{22}) on the cartilage surface

In order to investigate of the effects of the implementation of “UMAT” and fibril orientation, the distribution of S_{11} and S_{22} on the whole cartilage surface are compared in Figure 5.28 and Figure 5.29 respectively.

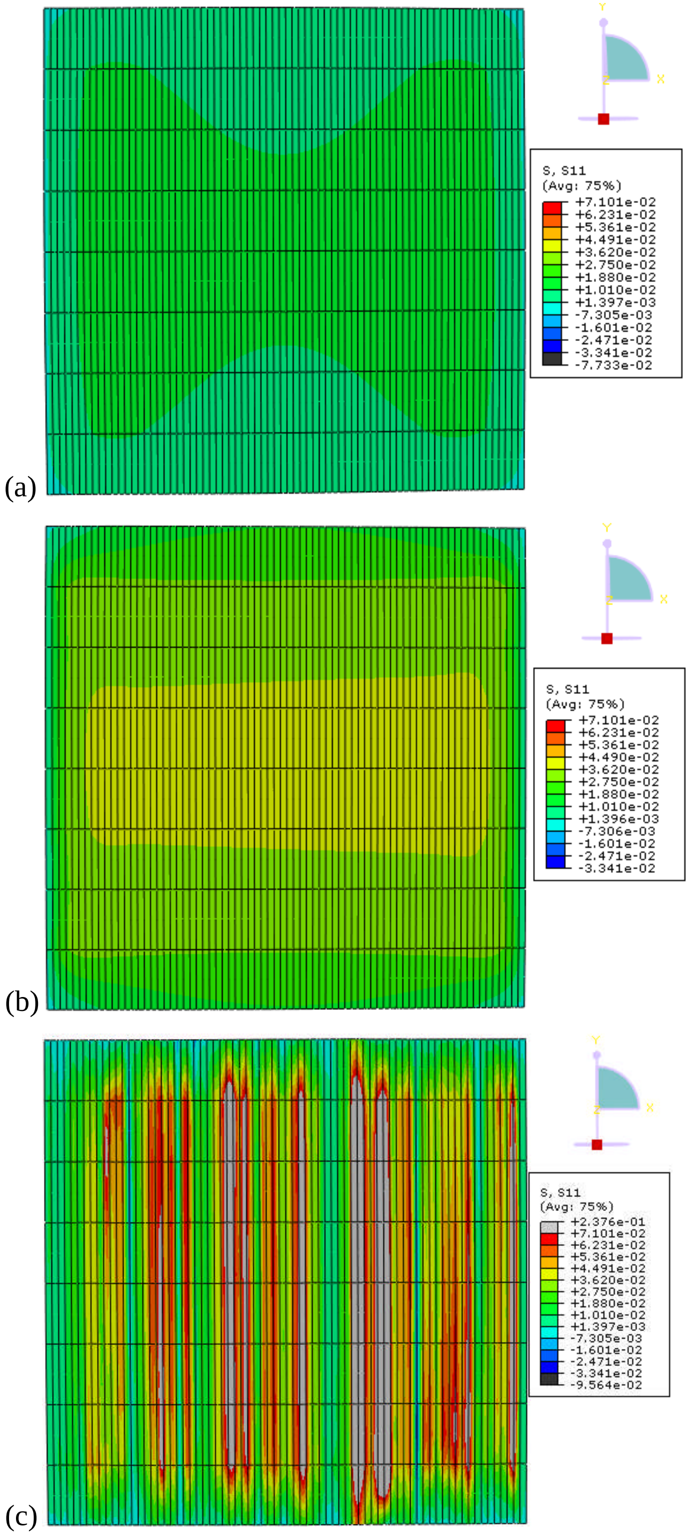

Figure 5.28 Stress along global X-axis (S_{11}; MPa) on cartilage surface of (a) the Isotropic-3D, (b) the Uniform-3D and (c) the DT-MRI-3D model at the end of ramp loading (t = 2s).

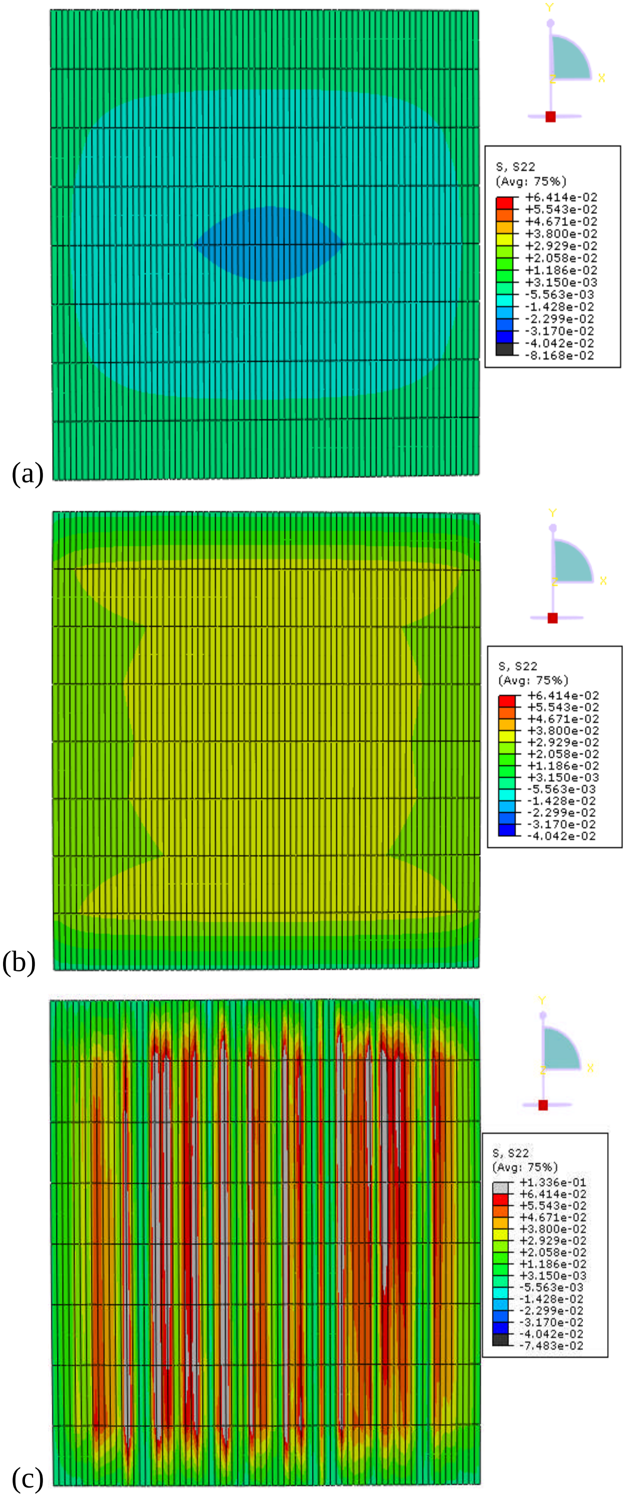

Figure 5.29 Stress along global Y-axis (S_{22}; MPa) on cartilage surface of (a) the Isotropic-3D, (b) the Uniform-3D and (c) the DT-MRI-3D model at the end of ramp loading (t = 2s).

In the DT-MRI-3D model, highest values of S_{11} and S_{22} distributed in narrow stripes along global Y-axis (grey and red area in Figure 5.28 (c) and Figure

5.29 (c)) separated by the stripes with low values (green and blue area in Figure 5.28 (c) and Figure 5.29 (c)). In contrast, S_{11} and S_{22} distributed regularly in the Isotropic-3D and Uniform--3D model with higher values in the central region ((a) and (b) in Figure 5.27 and Figure 5.29).

5.5.2 Validation results of the 3D DT-MRI based model

In order to enable the cartilage to support the higher load equivalent to the applied pressure which was 0.2 MPa in the experiment, the Young's modulus of the nonfibrillar matrix E_m in the DT-3D model were increased to the range of 0.63 - 0.99 MPa from the value of 0.26 MPa in Table 5.1. The axial displacements of the 3D-DT models with different Young's modulus were compared with the result of experiment (Figure 5.30).

In Figure 5.30, the curve of the DT-3D model with the *Young's* modulus of the nonfibrillar matrix E_m = 0.66 MPa fitted the experimental data (blue curve) better than the green curve with 0.63 MPa *Young's* modulus at the stage of equilibrium. The purple curve with 0.96 MPa *Young's* modulus could not follow the increase trend of the experimental data and achieved a much lower equilibrium.

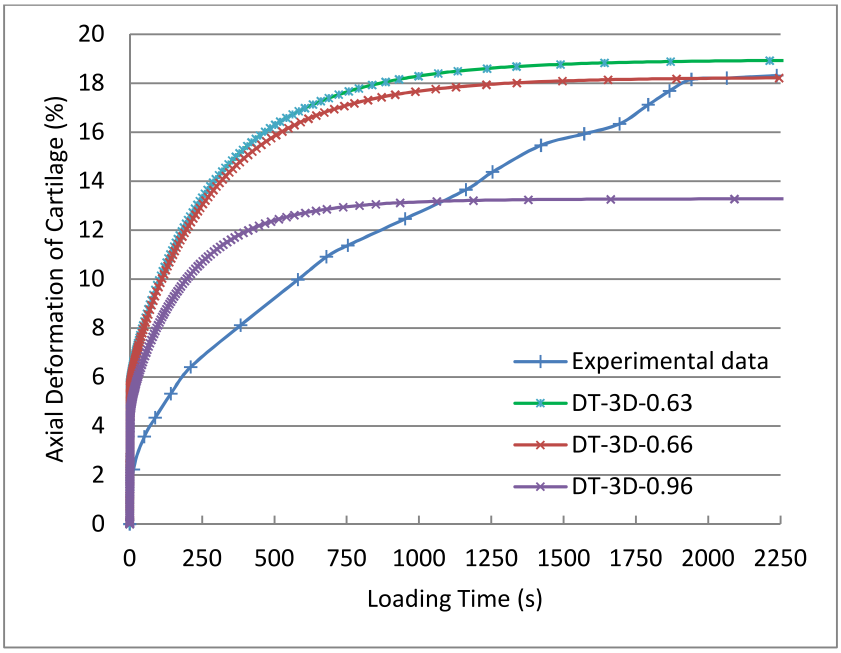

Figure 5.30 Comparison of axial deformation of cartilage in experiment and modelling with different Young's modulus of the nonfibrillar matrix (t = 2250s).

However, the red curve increased much faster than the experimental data before the equilibrium stage. To fit the experimental curve better, the permeability in the models with 0.63 MPa and 0.66 MPa *Young's* modulus was decreased to 1.0×10^{-15} $m^4/(N{\cdot}s)$ and 2.0×10^{-15} $m^4/(N{\cdot}s)$ respectively from the value of 3.0×10^{-15} $m^4/(N{\cdot}s)$ in Table 5.1. The results of the modified models were also compared with experimental data (Figure 5.31).

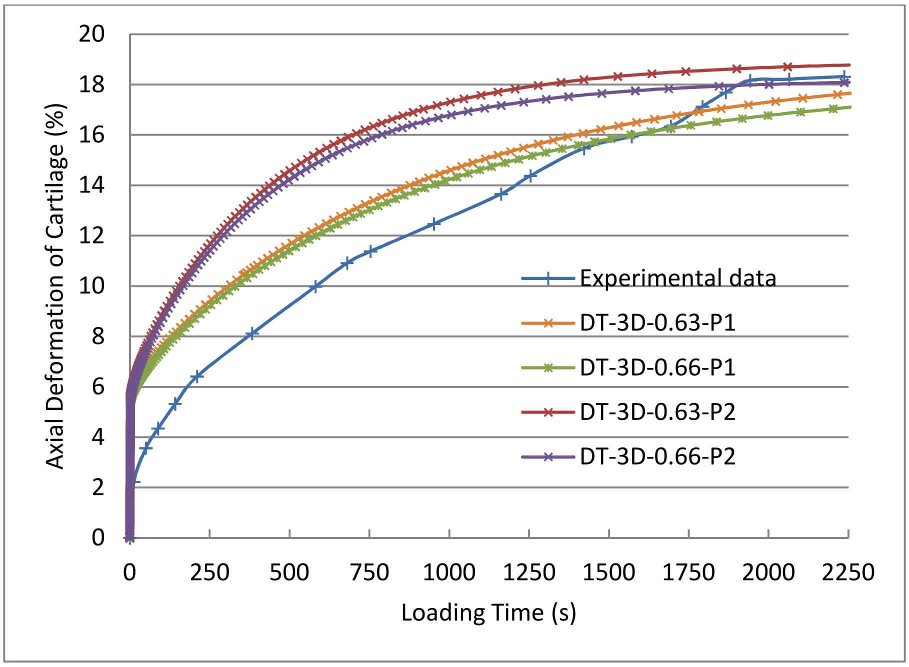

Figure 5.31 Comparison of axial deformation of cartilage in experiment and modelling with different Young's modulus and permeability of the nonfibrillar matrix (t = 2250s).

In contrast to the modelling results in Figure 5.30, the lower value of permeability reduced the axial displacement of cartilage surface in the four models in Figure 5.31 at the corresponding time. This made the two modelling curves fit the experimental data better at the long period before the equilibrium stage of creep test (Figure 5.31).

5.6 Discussion

The numerical results from the 3D fibril reinforced models in this chapter (Section 5.5) modeled the functional role of collagen fibril in unconfined compression of articular cartilage: the high tensile stiffness of collagen acts in a similar way as the rigid side-wall of a confining chamber, resisting lateral expansion of the tissue and pressurizing the interstitial fluid considerably to produce the pore pressure higher than that in the Isotropic model (Soltz and Ateshian, 2000).

5.6.1 The effect of fibril reinforcement

5.6.1.1 The effect on pore pressure and fluid load support on the cartilage surface

When the collagen fibrils were implemented by “UMAT”, the vertical Young’s modulus in the DT-MRI-3D model was defined lower (0.52 MPa of non-fibrillar Young’s modulus) than in the Isotropic-3D model (1.13 MPa). This made the top layer of the tissue deform larger along the vertical direction in the DT-MRI-3D model (Figures 5.23-5.25) and the interstitial fluid in the top cartilage layer was pressurized more severely at the ramp loading stage, compared to the Isotropic-3D model.

Meanwhile, the combined Young’s modulus in the radial direction (3 MPa of fibrillar tensile modulus plus 0.52 MPa of non-fibrillar Young’s modulus) which was much greater than that in the Isotropic-3D model (1.13 MPa) at the beginning of simulation. As the fibrillar modulus was strain-dependent in the DT-MRI-3D model, it increased as the cartilage was expanded while the ramp load applied. The higher tensile modulus produced the higher values of stress along the two midlines (S_{11} in Figure 5.27(a) except few lower points and S_{22} in Figure 5.27(b)) and distributing on the whole cartilage surface (Figure 5.28 and 5.29), leading to the lower deformation of the top cartilage layer along the two radial direction of global X- and Y-axis in the DT-MRI-3D model than in the Isotropic-3D model (Figure 5.22). The pressurization of the interstitial fluid in the top cartilage layer was greatly enhanced by the lower radial deformation. So the highest pore pressure (Figure 5.12 and 5.15) and fluid load support (Figure 5.13) was produced in the DT-MRI-3D model in contrast to the other two models.

As all of the collagen fibrils were aligned along the global X-axis and the fibrillar Young's modulus was constant but not strain-dependent as that in the DT-MRI-3D model, the cartilage in the Uniform-3D model was not reinforced to the similar extent as in the DT-MRI-3D model in the direction of global Y-axis (Figure 5.29 (b) and (c)). This led to the greatly lower radial deformation of the top cartilage layer in the direction of global X-axis (Figure 5.22(a)), and the slightly higher deformation along the global Y-axis (Figure 5.22(b)) compared to the Isotropic-3D model. But the vertical deformation of the top cartilage layer was higher in the Uniform-3D model than in the Isotropic-3D model particularly at regions near the surface edge (Figure 5.24-5.25) due to the lower vertical Young's modulus compared to that in the Isotropic-3D model. All these factors caused by fibril implementation combined together, and produced the relatively higher pore pressure (Figure 5.12 and 5.15) and fluid load support (Figure 5.13) in the Uniform-3D model than in the Isotropic-3D model.

5.6.1.2 The effect on pore pressure and fluid velocity inside the whole cartilage

As the vertical deformation of the cartilage surface centre was set up to be the same in all of the 3D models in Section 5.3, the radial deformation of the whole cartilage became the main factor to affect the pressurization of the interstitial fluid inside the tissue.

For the DT-MRI-3D model, the radial deformation was slightly higher in the direction of global X-axis (Figure 5.22(a)) but apparently lower along the global Y-axis (Figure 5.22(b)) than the Isotropic-3D model. This made the pore pressure distribute completely different inside the whole cartilage in the two models: the pore pressure with high values only arose around the centre of cartilage bottom in the Isotropic-3D model ((a) in Figure 5.16 and 5.17); but in the DT-MRI-3D model, it emerged from the middle zone to the surface of cartilage ((c) in Figure 5.16 and 5.17) due to the reinforcement of the collage fibril in the top two layers of cartilage.

The Uniform-3D model had the greatly lower radial deformation of the whole cartilage in the direction of global X-axis although decreasing from top to bottom (Figure 5.22(a)), compared to the Isotropic-3D model. This reinforcement caused by the collagen fibril produced the second and third highest pore pressure occupying the majority of the volume of cartilage in the Uniform-3D model, particularly in the cross-section along the global Y-axis ((b) in Figure 5.16 and 5.17).

Inside the cartilage, the differences of pore pressure at the various parts of cartilage made the interstitial fluid flow from the parts with higher pore pressure to the other parts where pore pressure was lower. So the different distribution of pore pressure determined the magnitude and direction of the fluid velocity in the three models. In the Isotropic-3D model, the regular distribution of pore pressure with the high value in the central area of cartilage ((a) in Figure 5.16 and 5.17) made the fluid flow outward while the highest fluid velocity emerged along the bottom edge of cartilage parallel to the global Y-axis ((a) in Figures 5.19 - 5.21). The widely distributing high pore pressure in the Uniform-3D model ((b) in Figure 5.16 and 5.17) produced the largest magnitude of fluid velocity on the vertical cartilage surface in the global Y-Z plane ((b) in Figure 5.18 and 5.21), but it also caused the lowest fluid velocity in the central volume of cartilage due to the small differences of pore pressure in this region. As for the DT-MRI-3D model, the irregular distribution of pore pressure ((c) in Figure 5.16 and 5.17) led to the disordered fluid flow throughout the whole cartilage ((c) in Figure 5.19 - 5.21).

5.6.2 The influence of the realistic fibril orientation

Compared to the uniformly reinforced model, the implementation of the realistic fibril orientation in the 3D fibril-reinforced model increased the value of peak pore pressure by 15% while the peak contact pressure was 4.3% lower, making the peak value of fluid load support increase from 80.4% to 96.7% (Figure 5.18). While the higher peak pore pressure decreased the load supported by the solid phase of the cartilage, the lower value of peak contact pressure would directly reduce the effective coefficient of friction and protect the cartilage. These results were extremely different from those in the 2D fibril-reinforced model with realistic fibril orientation - the higher peak pore pressure (Figures 4.9) was always accompanied by the higher peak contact pressure (Figures 4.8) which would affect the function of the fluid load support on protecting the cartilage. The reason leading to this difference might be the slightly larger deformation of the first cartilage layer in the DT-MRI-3D model (Figure 5.23) - the oblique fibrils in this layer made the tissue not reinforced as stiff as in the Uniform-3D model; but the first layer deformed less in the 2D DT-MRI based model (Figures 4.13).

Another important finding of the 3D fibril-reinforced model implementing realistic fibril orientation was the load could be further increased to 5.4 N which would match the 0.2 MPa pressure applied in the experiment of unconfined compression (Section 5.4), and the cartilage was able to achieve the equilibrium after one hour’s creep (Figure 5.26). This made it feasible to validate the model with the experimental data (Section 5.3) and overcame the limitation of the 3D fibril-reinforced model.

5.6.2.1 The influence on the stress along the global X-axis (S11)

The values of stress along Midline-X (S_{11}) fluctuated severely on cartilage surface in the DT-MRI-3D model, while the curves of the other two models varied smoothly (Figure 5.27(a)). The fluctuation were caused by the implementation of the realistic fibril orientation derived from the DT-MRI data: The lower values within fluctuating curve were corresponding to the apparently large angles between the collagen fibril (principal eigenvectors) and the cartilage surface (parallel to the X-Y plane) in the first layer of the DT-MRI pixel grids (Figure 2.2), which were greater than 10° (Figure 2.3 and 2.4). For example, the lowest value was corresponding to the greatest angle which was nearly 78.3°.

In contrast to the severe fluctuation of S_{11}, the curve of the stress along Midline-Y (S_{22}) was relatively flat. This was due to the same fibril orientation implemented in the eight elements along Midline-Y.

5.6.2.2 The influence on the distribution of contact pressure on cartilage surface

Contact pressure was only calculated on the integration points of the reduced hexahedral element. So it distributed discontinuously on the surface of cartilage in all of the three 3D models (Figure 5.14). Similar as the variation of S_{11}, the curve of contact pressure along Midline-X in the DT-

MRI-3D model fluctuated frequently (Figure 5.11(a)). The fluctuation was also produced by the different fibril orientation implemented in the 74 elements along Midline-X.

Implementing the same fibril orientation in the eight elements, the curve of contact pressure along Midline-Y in the DT-MRI-3D model was nearly coincide with that of the Uniform-3D model without the influence of the fibril (Figure 5.11 (b)).

5.6.3 Limitation of the DT-MRI-3D model

The aspect ratio along global Y-axis of the 3D elements was set to be 8:74 in order to save the time of computing. This led to the irregular distribution of pore pressure along global Y-axis on the bottom of cartilage in the uniformly reinforced and the fibril-reinforced models, without apparent influence to the isotropic model (Figure 5.16). However, it did not affect the pore pressure and fluid load support on the cartilage surface (Figure 5.12-13 and 5.15).

As introduced in Section 5.2.6, only one fibril orientation was implemented to the eight elements which were defined as an element set in the DT-MRI-3D model. This was due to the limitation of the DT-MRI data: only one cross-section with 2mm thickness of the cartilage sample was scanned and no information related to the orientation could be derived for the fibrils in the remaining region of the sample. This problem may be solved by scanning the parallel slices of the sample at different time, with a smaller thickness such as 0.8mm used in Pierce et al. (2010). With the more detailed data on fibril orientation, the DT-MRI-3D model would be more realistic.

In the validation of the DT-MRI-3D model (Section 5.4), the cuboids geometry of the cartilage sample was a factor to affect the reliability of curve-fitting the experimental data. As mentioned in Section 5.2, the cartilage region except the MRI scanning slice did not have related data to define the orientation of the collagen fibril when a cylinder with the exact dimension of the sample was used. The method used in the current DT-MRI-3D model - the element set definition in “DISTRIBUTION” (Section 5.2 and 5.3) is feasible to solve this problem, given the periphery region of the cartilage cylinder could be omitted to be implemented with fibril orientation.

Chapter 6 Overall Discussion and Conclusions

6.1 Fibril Reinforced Finite Element Modelling of Articular Cartilage

Natural articular cartilage is known to be an excellent bearing material with a very low friction coefficient and wear rate. Theoretical and experimental studies have demonstrated that the interstitial fluid of cartilage is pressurised considerably under loading, potentially supporting the applied load and leading to the low friction coefficient (Forster et al., 1996 and 1999). The low friction leads to a low shearing stress and potentially reduces wear. The proportion of the total load supported by fluid pressurisation in articular cartilage, called the fluid load support, is therefore an important parameter in biotribology and determined as the main aspect of cartilage behaviour to be investigated in the current study.

Experimental studies can provide fundamental information on cartilage biomechanics. However, they are unable to measure a number of biomechanical parameters within the tissue particularly the fluid pressure and flow. So it is necessary to use simulation-based numerical methods, such as finite element analysis to investigate these variables and interpret the biomechanical and biophysical basis of the experimental results. With the validation of the availability of validated commercial finite element codes (Wu et al., 1998), the application of such computational models to predict cartilage behaviour including biotribology and fluid load support has become more achievable widespread (Ateshian, 2009).

6.1.1 Material models of cartilage

As understanding of the structure and behaviour of articular cartilage has improved over recent years, the material models used in the finite element analysis of cartilage have also been improving. The earliest single-phase constitutive models only considered the solid phase of the tissue. This simplification led to the limited capabilities to describe the time-dependent response which is mainly caused by the interstitial fluid flow in compressed cartilage (Kazemi et al., 2013). Hence the single-phase models could not investigate the role played by the pressurisation of interstitial fluid in tribology of the joint.

Accounting for the effects of fluid pressurisation, both solid and fluid phases were considered in the second generation of constitutive models - the biphasic or the poroelastic models. However, the interstitial fluid pressure approached the compressive stress when the cartilage was under high strain-rate compression (Brown et al., 1986 and Miller, 1998) and the peak fluid load support was measured to be 99% in some cartilage specimens (Park et al., 2003). Neither poroelastic nor biphasic isotropic models had enough capabilities to predicted this peak value of fluid load support in cartilage (Kazemi et al., 2013). The transversely isotropic poroelastic or biphasic models could predict the high value of fluid load support (Solt et al., 2013), but had the limitation of not simulating the tension-compression nonlinearity of cartilage (Bursac et al. 1999).

The fibril-reinforced models were considered as the third generation of the constitutive models for cartilage, which successfully accounted for the high pressurization of interstitial fluid in the tissue and overcame the limitation of the transversely isotropic poroelastic or biphasic models (Li et al., 1999 and Soulhat et al., 1999). In the fibril-reinforced models, articular cartilage was considered as an isotropic porous matrix saturated in water, reinforced by a fibrillar network (Section 3.2; Figure 1.12). The porous matrix was nonfibrillar, representing the solid matrix excluding the collagen fibrils. The nonfibrillar matrix was modeled as a continuous linearly elastic material with the Young's modulus and Poisson's ratio. The collagen fibrils were simulated separately with nonlinearly elastic or viscoelastic properties in different models. The stress of the fibril-reinforced material is given by the sum of the porous matrix and the fibrillar network.

Compared to the second generation of constitutive cartilage models without fibril reinforcement, the fibril-reinforced model could not only predict the high fluid pressure in the cartilage under fast compressions (while the fibrillar nonlinearity was included) but also overcome the limitation of simulating the tension-compression nonlinearity of cartilage in the transversely isotropic models (Li et al., 2003). So the fibril-reinforced model was chosen to achieve the objectives of the current study, with the most widely used continuum element (Table 1.6) to simulate the collagen fibril.

6.1.2 Realistic orientation of collagen fibril

Various patterns have been used to define collagen fibril orientation in fibril-reinforced models, but most of them were idealized (Wilson et al. 2004 and Gupta et al. 2009) or simplified (Li et al. 2009). In contrast, the DT-MRI method (Meder et al., 2006 and Pierce et al. 2010) was the most realistic. In this thesis, the angles between principal eigenvectors of the diffusion tensors captured from the patellofemoral grooves cartilage (derived by Dr Robin

Damion, School of Physics, University of Leeds) and the planes parallel to the cartilage surface were analysed in Chapter 2. The distribution of collagen fibril is consistent with literature particularly the results of Visser et al. (2008) which was also derived from DT-MRI data (Figure 1.20a). This provided extra confidence that the principal eigenvectors of the DT-MRI data provided a reasonable representation of the collagen fibril orientation.

6.1.3 The 2D axisymmetric fibril-reinforced model

The methodology to implement the nonlinearly viscoelastic properties and orientation of collagen fibril was first applied to the 2D axisymmetric fibril-reinforced model in Chapter 4. The material parameters used in this model were selected from Li et al. (2009) which were derived by manually curve-fitting the experimental data (Li et al. 2003). The comparison of the preliminary results between the fibril-reinforced models and the Isotropic model in Chapter 4 clearly showed the function of the fibril reinforcement - the high tensile stiffness of collagen fibril acted as the rigid side-wall of a confining chamber resisting lateral expansion of the tissue, and enhanced the pressurization of interstitial fluid considerably to produce the pore pressure higher than that in the Isotropic model (Soltz and Ateshian, 2000).

The addition of fibril-reinforcement in the 2D model increased the peak fluid load support to around 90% from less than 60% in the Isotropic model (Figure 4.10), regardless of whether that reinforcement was idealised or DT-MRI-based. This represented a decrease of the load supported by the solid phase of the cartilage leading to the reduction in solid-to-solid contact, which explains the low effective time dependent coefficient of friction found experimentally (McCutchen, 1962; Forster and Fisher, 1996; Ateshian et al., 1998; Forster and Fisher, 1999; Krishnan et al., 2004). The frictional shear stresses were also reduced in turn by the high fluid load support. The reductions of contact and shear stresses combined together to protect the natural cartilages from wear and led to their long term survivorship (Pawaskar, 2010).

6.1.4 The 3D fibril-reinforced model

The two dimensional fibril-reinforced implementing collagen fibril orientation derived from DT-MRI data could only support a low load (0.2N) and were unable to achieve the equilibrium after one hour’s creep (Figure 4.18) accompanying the slowly decreasing fluid load support (Figure 4.11). This made it difficult to validate the fibril-reinforced model with the cartilage thickness recorded from the high load experiment. So the 3D fibril-reinforced models were set up in Chapter 5 in order to overcome the limitation of the axisymmetric fibril-reinforced models.

In the 3D model implementing DT-MRI data based fibril orientation, the time of data preparation and computing increased enormously compared to the 2D models. However, the applied concentrated load was increased to 1.1N with the more impressive results in contrast to the 2D fibril-reinforced model.

Compared to the uniformly reinforced model, the implementation of the realistic fibril orientation in the DT-MRI-3D model increase the value of peak pore pressure by 15% while the peak contact pressure was 4.3% lower, making the peak value of fluid load support increase from 80.4% to 96.7% (Figure 5.18). While the higher peak pore pressure decreased the load supported by the solid phase of the cartilage, the lower value of peak contact pressure would directly reduce the effective coefficient of friction and protect the cartilage. These results were extremely different from those in the 2D fibril-reinforced model with realistic fibril orientation - the higher peak pore pressure (Figures 4.9) was always accompanied by the higher peak contact pressure (Figures 4.8) which would affect the function of the fluid load support on protecting the cartilage. The reason leading to this difference might be the slightly larger vertical deformation of the first cartilage layer in the DT-MRI-3D model (Figure 5.23) - the oblique fibrils in this layer reduced the stiffness compared to the Uniform-3D model. However, the first layer deformed less in the 2D DT-MRI based model (Figures 4.13).

Another important finding of the 3D fibril-reinforced model implementing realistic fibril orientation was that the load could be further increased to 5.4 N, which matched the 0.2 MPa pressure applied in the experiment of unconfined compression (Section 5.4), and the 3D model was able to achieve the equilibrium after one hour’s creep (Figure 5.26) making it feasible to validate the model with the experimental data (Section 5.3).

The 3D model was validated by using the modelling result on cartilage deformation to curve-fit the normalized experimental record of cartilage thickness. The main factors that influenced the curve of vertical deformation of cartilage in the 3D fibril-reinforced model were the *Young*’s modulus of the nonfibrillar matrix E_m and the permeability k. Through manually adjusting the value of these two parameters, the curve of the 3D model with $E_m = 0.66$ MPa and $k = 3.0 \times 10\text{-}15\ \mathrm{m}^4/(\mathrm{N{\cdot}s})$ successfully achieved the same equilibrium value as the experimental data with apparent deviation existing from the start stage until the equilibrium of experiment (Figure 5.30). The deviation could be reduced apparently by decreasing the permeability to k =

1.0 × 10-15 m^4/(N·s), although this made those two modelling curves unable to achieve equilibrium in the experiment time (Figure 5.31). Actually, the modelling results could curve-fit the experimental data best by adjusting more parameters in the meantime (Lei et al., 2007). The procedure of Lei et al. (2007) could estimate six parameters of the fibril-reinforced poroelastic cartilage model in Li et al. (1999) and could be adapted to other models under different experimental configuration. This would transfer the validation of the 3D fibril-reinforced model to the problem of extracting material parameters from the experimental data. However, the problem of material parameter estimation was beyond the scope of the thesis and might be the focus of work in the future.

6.1.5 Limitations

There were several limitations in the 3D fibril-reinforced model. The aspect ratio along global Y-axis of the 3D elements was set to be 8:74 in order to save the time of computing. This led to the irregular distribution of pore pressure on the bottom of cartilage in the uniformly reinforced and the fibril-reinforced models, without apparent influence to the isotropic model (Figure 5.16). However, it did not affect the pore pressure and fluid load support on the cartilage surface (Figure 5.12-13 and 5.15).

As only one cross-section with 2mm thickness of the cartilage sample was scanned, no information related to the orientation were derived for the fibrils in the remaining region of the sample. The one same fibril orientation was implemented to the eight elements which were defined as an element set in the DT-MRI-3D model and made the model less realistic. This problem may be solved by scanning several parallel slices of cartilage at different time, with a less thickness such as 0.8 mm in Pierce et al. (2010) using a cuboids sample. The increased slices of fibril orientation may also help to solve the previous problem related to the aspect ratio: the mesh density along global Y-axis can be increased with equal or less number of elements defined in the same element set. Furthermore, to use cuboids cartilage sample in the MRI scanning and compression test could solve the validation problem in Section 5.4 where different kinds of geometry were used in experiment and modelling.

For the validation of the 3D fibril-reinforced model, the experimental data itself may be a factor to affect the curve-fitting - the method used to record the thickness of the cartilage might underestimate the cartilage thickness although the deformations were approximately correct (according to Dr Robin Damion who performed the experiment).

In spite of these limitations, the implementation of “UMAT” (Dr L. P. Li, University of Calgary) and “ORIENTATION” including “Distribution” made it possible to investigate fluid load support in the 2D and 3D models reinforced by collagen fibril, with strain dependent Young’s modulus and realistic fibril orientation derived from DT-MRI data. The fibril reinforcement enhanced the pressurization of the interstitial fluid and produced higher fluid load support on the cartilage surface to protect the tissue from degradation by reducing solid-to-solid contact.

6.2 The Conclusions

The major conclusions of this work were:

1) The peak value of fluid load support in both 2D and 3D fibril-reinforced models was increased to greater than 80% from around 60% compared to the isotropic models, due to the reinforcement by collagen fibril, regardless of whether that reinforcement was idealized or derived from the DT-MRI data.

2) The 3D fibril-reinforced model implementing DT-MRI data did have the capability to support the high load applied in the experiment. The more important finding was that the cartilage could achieve equilibrium, hence this model was validated by curve-fitting the experimental record of cartilage thickness.

3) The implementation of the realistic fibril orientation derived from DT-MRI data in the 3D fibril-reinforced model increase the value of peak pore pressure by 15% compared to the uniformly reinforced model while the peak contact pressure was 4.3% lower, making the peak value of fluid load support increase from 80.4% to 96.7%.

4) The rationality to define the principal eigenvector as orientation of the corresponding primary collagen fibril in the fibril-reinforced models was verified by the positive results in 1), 2) and 3).

5) The feasibility and reliability of the methodologies to implement the DT-MRI data to the fibril-reinforced models was both confirmed in the process of validating the 3D model in 3).

6.3 Further Work

The main predictions of this study were the fluid load support on cartilage surface and the distribution of the pore pressure and fluid flow throughout the tissue. The reinforcement of collagen fibrils has been proved to enhance the pressurization of the interstitial fluid and produced high pore pressure within the cartilage, leading to the high fluid load support on the surface to protect the cartilage against friction and wear.

The methodologies and models proposed in this study may be adapted to investigate other experimental configurations such as indentation and confined compression. The user subroutine “UMAT” in ABAQUS (Dr L. P. Li, University of Calgary) had been successfully implemented to set up the whole joint model (Gu and Li, 2010). The “ORIENTATION” needs much more detailed DT-MRI information to define the orientation of collagen fibrils throughout the whole natural cartilages. The high resolution MRI scanning is difficult to perform on the whole joint and this might be the reason that Gu and Li, (2010) used the split-line pattern rather than the DT-MRI method to derive the fibril orientation of natural cartilages.

The material parameters and their values used in the fibril-reinforced models were selected from Li et al. (2009) which were derived by manually curve-fitting the experimental data (Li et al. 2003). So the value of each single parameter can be automatically optimized by the procedure of Lei et al. (2007) to make the modelling result curve-fit the experimental data best.

The cuboids form of cartilage sample should be used as Pierce et al. (2010), instead of the cylinder one to make the geometry in the models same as that in the experiment. If possible, the cartilage sample would be scanned on parallel slices of at different time to provide more information to define the orientation of collagen fibrils throughout the sample and make the fibril-reinforced models more realistic.

List of References

Adam C., Eckstein F., Milz S., Putz R., 1998. The distribution of cartilage thickness within the joints of the lower limb of elderly individuals. J Anat 193:203–214.

Akizuki S, Mow VC, Muller F, Pita JC, Howell DS, Manicourt DH., 1986. Tensile properties of human knee joint cartilage. I. Influence of ionic conditions, weight bearing, and fibrillation on the tensile modulus. J Orthop Res 4(4):379–392.

Al Ali D., Graichen H., Faber S., Englmeier K.H., Reiser M., Eckstein F., 2002. Quantitative cartilage imaging of the human hind foot: precision and inter-subject variability. J Orthop Res 20: 249-256.

Almeida, E. S., Spilker, R. L.,1997.Mixed and penalty finite element models for the nonlinear behavior of biphasic soft tissues in finite deformation: part I alternate formulations. Comput. Methods Biomech. Biomed. Eng.1, 25–46.

Armstrong, C.G., Lai, W.M., Mow, V.C., 1984. An analysis of the unconfined compression of articular cartilage. J. Biomech. Eng. 106, 165–173.

Ateshian, G.A., Lai,W.M., Zhu,W.B., Mow, V.C., 1994. An asymptotic solution for the contact of two biphasic cartilage layers. J. Biomech. 27, 1347–1360.

Ateshian, G.A., Wang, H., 1995. A theoretical solution for the frictionless rolling contact of cylindrical biphasic articular cartilage layers. J. Biomech. 28, 1341–1355.

Ateshian, G.A., 1997. A theoretical formulation for boundary friction in articular cartilage. J. Biomech. Eng. 119, 81–86.

Ateshian, G.A.,Wang, H., Lai,W.M., 1998. The role of interstitial fluid pressurization and surface porosities on the boundary friction of articular cartilage. J. Tribol. 120, 241–248.

Ateshian, G.A., Mow, V.C., 2005. Lubrication and wear of diarthrodial joints. In: Mow, V.C., Huiskes, R. (Eds.), Basic Orthopaedic Biomechanics & Mechano- Biology. Lippincott Williams & Wilkins, Philadelphia, PA; London.

Ateshian, G.A., 2009. The role of interstitial fluid pressurization in articular cartilage lubrication. J. Biomech. 42, 1163-1176.

Atkinson P, Haut RC., 1995. Subfracture insult to the human cadaver patellofemoral joint produces occult injury. J Orthop Res 13:936–44.

Bader DL, Kempson GE, Egan J, Gilbey W, Barrett AJ., 1992. The effects of selective matrix degradation on the short-term compressive properties of adult human articular cartilage. Biochim Biophys Acta 1116(2):147–54.

Bear, Jacob, 1972. Dynamics of Fluids in Porous Media, Dover. — ISBN 0-486-65675-6.

Biot, M.A., 1941. General theory of three-dimensional consolidation. Journal of Applied Physics 12, 155-164.

Buckwalter JA, Hunziker EB, Rosenberg LC, Coutts R, Adams M, Eyre D., 1991. Articular cartilage: composition and structure. In: Wo SI, Buckwalter JA, editors. Injury and repair of musculoskeletal soft tissues. 2nd ed. Park Ridge: American Academy of Orthopaedic Surgeons, 405–25.

Bursac, P. M., Obitz, T. W., Eisenberg, S. R., and Stamenovic, D., 1999. ‘‘Confined and Unconfined Stress Relaxation of Cartilage: Appropriateness of a Transversely Isotropic Analysis,’’ J. Biomech., 32, 1125–1130.

Callaghan P. Principles of Nuclear Magnetic Resonance Microscopy. Oxford: Clarendon Press 1991.

Charnley, J., 1960. The lubrication of animal joints in relation to surgical reconstruction by arthroplasty. Ann. Rheum. Dis. 19, 10–19.

Chegini, S., Ferguson, S.J., 2010. Time and depth dependent poisson’s ratio of cartilage explained by an inhomogeneous orthotropic fiber embedded biphasic model. Journal of Biomechanics, doi: 10. 1016/j. jbiomech. 2010. 03. 006

Chen, A.C., Bae, W.C., Schinagl, R.M., Sah, R.L., 2001. Depth- and strain-dependent mechanical and electromechanical properties of full-thickness bovine articular cartilage in confined compression. J. Biomech. 34, 1–12.

Cicuttini F, Forbes A, Morris K, Darling S, Bailey M, Stuckey S, 1999. Gender differences in knee cartilage volume as measured by magnetic resonance imaging. Osteoarthritis Cartilage 7, 265-271.

Cicuttini F, Forbes A, Asbeutah A, Morris K, Stuckey S, 2000. Comparison and reproducibility of fast and conventional spoiled gradient-echo magnetic resonance sequences in the determination of knee cartilage volume. J Orthop Res; 18, 580-584.

Clark JM., 1991. Variation of collagen fiber alignment in a joint surface: a scanning electron microscope study of the tibial plateau in dog, rabbit, and man. J Orthop Res 9: 246–57.

Clarke IC., 1971. Articular cartilage: a review and scanning electron microscope study. 1. The interterritorial fibrillar architecture. J Bone Joint Surg Br 53:732–50.

Cohen, B., Gardner, T.R., Ateshian, G.A., 1993. The influence of transverse isotropy on cartilage indentation behavior: A study of the human humeral head. In: Transactions Orthopaedic Research Society. Orthopaedic Research Society, Chicago, IL: 185.

Cohen, B., Lai, M.W., Mow, V.C., 1998. A transversely isotropic biphasic model for unconfined compression of growth plate and chondroepophysis. Journal of Biomechanical Engineering 120 (4): 491-496.

Cohen ZA, McCarthy DM, Kwak SD, Legrand P, Fogarasi F, Ciaccio EJ, 1999. Knee cartilage topography, thickness, and contact areas from MRI: in-vitro calibration and in-vivo measurements. Osteoarthritis Cartilage 7: 95-109

Cremer MA, Rosloniec EF, Kang AH., 1998. The cartilage collagens: a review of their structure, organization, and role in the pathogenesis of experimental arthritis in animals and in human rheumatic disease. J Mol Med 76:275–88.

DiSilvestro M.R., Zhu Q., Wong M., Jurvelin JS, Suh JK., 2001. Biphasic poroviscoelastic simulation of the unconfined compression of articular cartilage. I. Simultaneous prediction of reaction force and lateral displacement. J Biomech Eng 123(2):191–7.

Dowson, D., Wright,V., Longfield, M.D., 1969. Human joint lubrication. Biomed. Eng. 4,160–165.

Dowson D., 1990. Biotribology of natural and replacement synovial joints. In: Mow VC, Ratcliffe A, Woo SLY, editors. Biomechanics of diarthroidal joints. New York: Springer–Verlag; 305–45.

Eckstein F., Lemberger B., Gratzke C., Hudelmaier M., Glaser C., Englmeier K.H., Reiser M., 2005. In vivo cartilage deformation after different types of activity and its dependence on physical training status. Annals of the Rheumatic Diseases 64 (2): 291–295.

Eckstein F, Sittek H, Schulte E, Kiefer B, Reiser M, Putz R. The potential of magnetic resonance imaging (MRI) for quantifying articular cartilage thickness - a methodological study. Clin Biomech 1995;10: 434-40.

Ethier CR, Simmons CA, 2007. Introductory biomechanics: from cells to organisms. Cambridge, UK: Cambridge University Press.

Eyre DR, Apones S, Wu JJ, Ericksson LH, Walsh KA., 1987. Collagen type IX: evidence for covalent linkages to type II collagen in cartilage. FEBS Lett 220:337–341.

Eyre DR., 1991. The collagens of articular cartilage. Sem Arthritis Rheum 21:2–11.

Federico, S., La Rosa, G., Herzog, W. and Wu, J.Z. , 2004. Effect of fluid boundary conditions on joint contact mechanics and applications to the modeling of osteoarthritic joints. Journal of Biomechanical Engineering. 126(2): 220-225.

Federico S., Grillo A., Rosa G.L., Giaquinta G., Herzog W., 2005. A transversely isotropic, transversely homogeneous microstructure-statistical model of articular cartilage. J Biomech 38: 2008 - 2018.

Forster, H., Fisher, J., 1996. The influence of loading time and lubricant on the friction of articular cartilage. Proc. Inst. Mech. Eng. [H] 210, 109–119.

Forster, H., Fisher, J., 1999. The influence of continuous sliding and subsequent surface wear on the friction of articular cartilage. Proc. Inst. Mech. Eng. [H] 213, 329–345

Frank, E.H., Grodzinsky, A.J., 1987. Cartilage electromechanics II — a continuum model of cartilage electrokinetics and correlation with experiments. Journal of Biomechanics 20 (6), 629–639.

Fung Y.C., 1993. Biomechanics: Mechanical Properties of Living Tissues, 2nd edition. Springer-Verlag, New York.

Fermor, H.L., McLure, S. W.D., Taylor, S.D., Russell, S.L., Williams, S., Fisher, J. and Ingham, E., 2013. Biological biochemical and biomechanical characterisation of articular cartilage from the porcine, bovine and ovine hip. Biomedicine engineering and material. In process.

Garcia JJ, Aliero NJ, Haut RC., 1998. An approach for stress analysis of transversely isotropic biphasic cartilage under impact load. J Biomech Eng 120:608–13.

Greene GW., Zappone B, So¨derman O, Topgaard D, Rata G, Hongbo Z, Israelachvili JN, 2010. Anisotropic dynamic changes in the pore network structure, fluid diffusion and fluid flow in articular cartilage under compression. Biomaterials 31: 3117-3128.

Gu K.B., Li L.P., 2011. A human knee joint model considering fluid pressure and fiber orientation in cartilages and menisci. Med Eng Phys 33:497–503.

Gu WY, Lai WM, Mow VC., 1993; Transport of fluid and ions through a porous-permeable charged-hydrated tissue, and streaming potential data on normal bovine articular cartilage. J Biomech 26:709–23.

Gu WY, Lai WM, Mow VC., 1998. A mixture theory for chargedhydrated soft tissues containing multi-electrolytes: passive transport and swelling behaviors. J Biomech Eng 120:169–80.

Guide for verification and validation in computational solid dynamics, 2006 (American Society of Mechanical Engineers, New York).

Gupta S., Lin J., Ashby P., Pruitt L.,2009. A fiber reinforced poroelastic model of nanoindentation of porcine costal cartilage: A combined experimental and finite element approach. J Mech. Beh. Biomed. Mater. 2: 326-338.

Hasler EM, Herzog W, Wu JZ, Muller W, Wyss U., 1999. Articular cartilage biomechanics: theoretical models, material properties, and biosynthesis response. Clin Rev Biomech Eng 27:415–88.

Hayes WC, Bodine AJ., 1978. Flow-independent viscoelastic properties of articular cartilage matrix. J Biomech 11(8–9):407– 19.

Higginson GR, Litchfield MR, Snaith J, 1976. Load–displacement – time characteristics of articular cartilage. Int J Mech Sci 18:481–486

Hunter W., 1743. Of the Structure and Disease of Articulating Cartilage, Phi, Trans. Roy., Vol. 42, 514.

Holmes M.H. and Mow V.C., 1990. The nonlinear characteristics of soft gels and hydrated connective tissues in ultra-filtration. J Biomech 23: 1145 - 1156.

Hunziker EB, Michel M, Studer D., 1997. Ultrastructure of adult human cartilage matrix after cryotechnical processing. Microsc Res Technol 37:271–84.

Huyghe J.M., Janssen J.D. 1997. Quadriphasic mechanics of swelling incompressible porous media. Int. J. Eng. Sci. 35, 793–802.

Huyghe JM, Janssen CF, Van Donkelaar CC, Lanir Y., 2002. Measuring principles of frictional coefficients in cartilaginous tissues and its substitutes. Biorheology. 39, 47–53.

Jay, G.D., Tantravahi, U., Britt, D.E., Barrach, H.J., Cha, C.J., 2001. Homology of lubricin and superficial zone protein (SZP): products of megakaryocyte stimulating factor (MSF) gene expression by human synovial fibroblasts and articular chondrocytes localized to chromosome 1q25. J. Orthop. Res. 19, 677–687.

Julkunen P, Kiviranta P, Wilson W, Jurvelin JS, Korhonen RK, 2007. Characterization of articular cartilage by combining microscopic analysis with a fibril-reinforced finite-element model. J Biomech 40:1862–1870.

Julkunen, P., R. K. Korhonen, W. Herzog, and J. S. Jurvelin., 2008a. Uncertainties in indentation testing of articular cartilage: a fibril-reinforced poroviscoelastic study. Med. Eng. Phys. 30:506–515.

Julkunen P, Korhonen RK, Nissi MJ, Jurvelin JS, 2008b. Mechanical characterization of articular cartilage by combining magnetic resonance imaging and finite-element analysis: a potential functional imaging technique. Phys Med Biol 53: 2425–2438.

Julkunen p., Jurvelin J.S., Isaksson H., 2010. Contribution of tissue composition and structure to mechanical response of articular cartilage under different loading geometries and strain rates. Biomech Model Mechanobiol 9: 237-245.

Junqueira LC, Carneiro J., 1983. Basic histology. 4th ed. Los Altos: Lange Medical; 129.

Kaab, M. J.; Gwynn, I. A. P.; Notzli, H. P., 1998: Collagen fibre arrangement in the tibial plateau articular cartilage of man and other mammalian species. Journal Of Anatomy. 1: 23-34, Y 193: 23-34.

Katta J., Pawaskar S.S., Jin, Z., Ingham E., Fisher J., 2007. Effect of load variation on the friction properties of articular cartilage. Proc. Instn Mech Engrs 221 Part J: J. Engineering Tribology 175 – 181.

Katta, J., Jin, Z., Ingham, E., Fisher, J., 2008. Biotribology of articular cartilage — a review of the recent advances. Med. Eng. Phys. 30, 1349–1363.

Kazemi M., Dabiri Y., and Li L. P., 2013. Recent Advances in Computational Mechanics of the Human Knee Joint. Computational and Mathematical Methods in Medicinehttp://dx.doi.org/10.1155/2013/718423.

Kiviranta P, Rieppo J, Korhonen RK, Julkunen P, Töyräs J, Jurvelin JS, 2006. Collagen network primarily controls poisson’s ratio of bovine articular cartilage in compression. J Orthop Res 24:690– 699

Korhonen, R.K., Laasanen, M.S., Toyras, J., Lappalainen, R., Helminen, H.J., Jurvelin, J.S., 2003. Fibril reinforced poroelastic model predicts specifically mechanical behavior of normal, proteoglycan depleted and collagen degraded articular cartilage. J Biomech 36: 1373–1379.

Krishnan, R., Caligaris, M., Mauck, R.L., Hung, C.T., Costa, K.D., Ateshian, G.A., 2004a. Removal of the superficial zone of bovine articular cartilage does not increase its frictional coefficient. Osteoarthritis Cartilage 12, 947–955.

Krishnan, R., Kopacz, M., Ateshian, G.A., 2004. Experimental verification of the role of interstitial fluid pressurization in cartilage lubrication. J. Orthop. Res. 22, 565–570.

Krishnan, R., Mariner, E.N., Ateshian, G.A., 2005. Effect of dynamic loading on the frictional response of bovine articular cartilage. J. Biomech. 38, 1665–1673.

Larry W Moreland, 2003. Intra-articular hyaluronan (hyaluronic acid) and hylans for the treatment of osteoarthritis: mechanisms of action. Arthritis Res 5(2): 54–67.

L. P. Rasanen, M. E. Mononen, M. T. Nieminen, E. Lammentausta, J. S. Jurvelin, and R. K. Korhonen, 2012. Implementation of subject-specific collagen architecture of cartilage into a 2D computational model of a knee joint—data from the Osteoarthritis Initiative (OAI),” Journal of Orthopaedic Research, vol. 31, no. 1, 10–22.

Lai WM., Mow VC., Roth V., 1981. Effects of nonlinear strain-dependent permeability and rate of compression on the stress behavior of articular cartilage. J Biomech Eng; 103: 61–66.

Le Bihan D, Mangin J-F, Poupon C, Clark CA, Pappata S, Molko N, et al. 2001. Diffusion tensor imaging: concepts and applications. J Magn Reson Imaging. 13:534-46.

Lei F. and Szeri A.Z., 2007. Inverse analysis of constitutive models: Biological soft tisues. J Biomech 40: 936 - 940.

Lewis, P.R., McCutchen, C.W., 1959. Experimental evidence for weeping lubrication in mammalian joints. Nature 184, 1285.

Li, L.P., Soulhat J., Buschmann M.D., Shirazi-Adl A., 1999. Nonlinear analysis of cartilage in unconfined ramp compression using a fibril reinforced poroelastic model. Clin. Biomech. 14(9), 673–682.

Li, L.P., Buschmann MD, Shirazi-Adl A., 2000. A fibril reinforced nonhomogeneous poroelastic model for articular cartilage: inhomogeneous response in unconfined compression. J Biomech. 33(12), 1533–1541.

Li, L.P., Buschmann MD, Shirazi-Adl A., 2001. The asymmetry of transient response in compression versus release for cartilage in unconfined compression. J. Biomech. Eng. 123, 519–522.

Li, L.P., Shirazi-Adl A, Buschmann MD., 2002. Alterations in mechanical behaviour of articular cartilage due to changes in depth varying material properties—a nonhomogeneous poroelastic model study. Comput. Meth. Biomech. Biomed. Eng. 5(1), 45–52.

Li, L.P., Buschmann MD, Shirazi-Adl A., 2003. Strain-rate dependent stiffness of articular cartilage in unconfined compression. J. Biomech Eng.125(2), 161–168.

Li L.P., Herzog W., 2004. The role of viscoelasticity of collagen fibers in articular cartilage: theory and numerical formulation. Biorheology 41:181–194.

Li L.P., J. T. M. Cheung, Herzog W., 2009. Three-dimensional fibril-reinforced finite element model of articular cartilage. Medical & Biological Engineering & Computing 47(6): 607-615.

Macirowski, T., Tepic, S., Mann, R.W., 1994. Cartilage stresses in the human hip joint. J. Biomech. Eng. 116, 10–18.

Mak A.F., 1986. The apparent viscoelastic behavior of articular cartilage — the contributions from the intrinsic matrix viscoelasticity and interstitial fluid flows. J Biomech Eng 108(2):123–30.

Mak A.F, Lai WM, Mow VC., 1987. Biphasic indentation of articular cartilage. I. Theoretical analysis. J Biomech 20(7):703–14.

Mak A.F., 1986. The apparent viscoelastic behavior of articular cartilage — the contributions from the intrinsic matrix viscoelasticity and interstitial fluid flows. J Biomech Eng 108(2):123–30.

Maroudas A., 1968. Physicochemical properties of cartilage in the light of ion-exchange theory. Biophys J 8:575–595

Maroudas A., 1975. Biophysical chemistry of cartilaginous tissues with special reference to solute and fluid transport. Biorheology 12:233–48.

Maroudas A., 1976. Balance between swelling pressure and collagen tension in normal and degenerate cartilage. Nature 260, 808–809.

Maroudas A., 1979. Physicochemical properties of articular cartilage. In: Freeman MAR, editor. Adult articular cartilage. 2nd ed. Kent, UK: Pitman Med.; 215–323.

McCutchen, C.W., 1962. The frictional properties of animal joints. Wear 5, 1–17.

McCutchen, C.W., 1966. Boundary lubrication by synovial fluid: demonstration and possible osmotic explanation. Fed. Proc. 25, 1061.

McCutchen, C.W., 1983. Joint lubrication. Bull. Hosp. Jt. Dis. Orthop. Inst. 43, 118–129.

McGibbon CA, Bencardino J, Yeh ED, Palmer WE, 2003. Accuracy of cartilage and subchondral bone spatial thickness distribution from MRI. J Magn Reson Imag 17:703-15.

Meder R, de Visser SK, Bowden JC, Bostrom T, Pope JM. Diffusion tensor imaging of articular cartilage as a measure of tissue microstructure. Osteoarthritis Cartilage 2006;14:875-81.

Mente PL, Lewis JL., 1994. Elastic modulus of calcified cartilage is an order of magnitude less than that of subchondral bone. J Orthop Res 12:637–47.

Michal Kozanek, Ali Hosseini, Fang Liu, Samuel K.Van de Velde, Thomas J. Gill, Harry E, Rubash, Guoan Li, 2009. Tibiofemoral kinematics and condylar motion during the stance phase of gait. J. Biomech. 42(12): 1877-1884.

Mononen M.E., Julkunen P., Töyräs J., Jurvelin J.S., Kiviranta I., Korhonen R.K. 2010. Alterations in structure and properties of collagen network of osteoarthritic and repaired cartilage modify knee joint stresses. Biomech Model Mechanobiol DOI 10.1007/s10237-010-0239-1.

Morgan FR., 1960. Mechanical properties of collagen and leather fibres. Am Leather Chem Assoc J., 55(1): 23–24.

Mow, V.C., Kuei, S.C., Lai, W.M., Armstrong, C.G., 1980. Biphasic creep and stress relaxation of articular cartilage: theory and experiment. ASME Journal of Biomechanical Engineering 102: 73-84.

Mow VC, Holmes MH, Lai WM., 1984. Fluid transport and mechanical properties of articular cartilage: a review. J Biomech 17(5):377–94.

Mow VC, Proctor CS, Kelly MA., 1989. Biomechanics of articular cartilage. In: Nordin M, Frankel VH, editors. Basic biomechanics of the mucoskeletal system. 2nd ed. Philadelphia, PA: Lea and Febiger; 31–57.

Mow VC, Zhu W, Ratclife A., 1991. Structure and function of articular cartilage and meniscus. In: Mow VC, Hayes WC, editors. Basic orthopaedic biomechanics. New York: Raven Press; 143–198.

Mow VC, Ratcliffe A, Poole AR., 1992. Cartilage and diarthrodial joints as paradigms for hierarchical materials and structures. Biomaterials 13:67–97.

Mow, V.C., Ratcliffe, A., 1997. Structure and function of articular cartilage and meniscus. In: Mow, V.C., Hayes, W.C. (Eds.), Basic Orthopaedic Biomechanics. Lippincott-Raven, Philadelphia p. xiii, 514.

Mow VC, Guo XE., 2002. Mechano-electrochemical properties of articular cartilage: their inhomogeneities and anisotropies. Annu Rev Biomed Eng 4:175–209.

Oloyede, A., Broom, N.D., 1994. The generalized consolidation of articular cartilage: an investigation of its near-physiological response to static load. Connective Tissue Research 31 (1), 75–86.

Oloyede, A., Broom, N.D., 1991. Is classical consolidation theory applicable to articular cartilage deformation? Clin. Biomech. (Bristol, Avon) 6, 206–212.

Oegema Jr TR, Carpenter RJ, Hofmeister F, Thompson Jr RC., 1997. The interaction of the zone of calcified cartilage and subchondral bone in osteoarthritis. Microsc Res Technol 37:324–32.

Park, S., Krishnan, R., Nicoll, S.B., Ateshian, G.A., 2003. Cartilage interstitial fluid load support in unconfined compression. J. Biomech. 36, 1785–1796.

Pawaskar SS, Fisher J, Jin Z. 2010. Robust and general method for determining surface fluid flow boundary conditions in articular cartilage contact mechanics modeling. Journal of Biomechanical Engineering 132(3), 1- 8.

Pierce, D. M., Ricken T., and G. A. Holzapfel., 2012. Modeling Sample/Patient-Specific Structural and Diffusional Response of Cartilage Employing DT-MRI. Int. J. Numer. Meth. Biomed. Engng. 2012; 00:1–15.

Pierce D. M., Trobin W.,RAYA J. G., Tratting S., Bischof H., Glaser C., and Holzapfel G. A., 2010. DT-MRI based computation of collagen fiber deformation in human articular cartilage: A feasibility study. Annuals of Biomedical Engineering. 38 (7): 2447-2463.

Puso M.A. and Weiss J.A., 1998. Finite element implementation of anisotropic quasi-linear viscoelasticity using a discrete spectrum approximation, *ASME J. Biomechanical Eng.* **120**, 62–70.

Quinn TM, Kocian P, Meister JJ., 2000. Static compression is associated with decreased diffusivity of dextrans in cartilage explants. Arch. Biochem. Biophys. 384(2), 327–34.

Quinn, TM, Morel V. , 2007 Microstructural modeling of collagen network mechanics and interactions with the proteoglycan gel in articular cartilage. Biomech. Model. Mechanobiol. 6:73–82.

Quiñonez, A.F., Summers, J.L., Fisher, J., Jin, Z.M., 2010. An analytical solution for the radial and tangential displacements on a thin hemispherical layer of articular cartilage. Biomech. Model. Mechanobiol. Volume 10, Issue 3, 283-293.

Radin, E.L., Swann, D.A., Weisser, P.A., 1970. Separation of a hyaluronate-free lubricating fraction from synovial fluid. Nature 228, 377–378.

Reynaud B, Quinn TM, 2006. Anisotropic hydraulic permeability in compressed articular cartilage. J Biomech 39:131–137

Roth V, Mow VC., 1980. The intrinsic tensile behavior of the matrix of bovine articular cartilage and its variation with age. J Bone Joint Surg Am 62:1102–17.

Sainath Shrikant Pawaskar, 2006. Contact Mechanics Modelling of Articular Cartilage and Applications. Master thesis, University of leeds.

Sainath Shrikant Pawaskar, 2010. PhD thesis, University of leeds.

Sanjeevi R, Somanathan N, Ramaswamy D., 1982. A viscoelastic model for collagen fibres. J Biomech 15:181–3.

Schmidt, T.A., Gastelum, N.S., Nguyen, Q.T., Schumacher, B.L., Sah, R.L., 2007. Boundary lubrication of articular cartilage: role of synovial fluid constituents. Arthritis Rheum. 56, 882–891.

Setton LA, Zhu WB, Mow VC, 1993. The biphasic poroviscoelastic behavior of articular cartilage: role of the surface zone in governing the compressive behavior. J Biomech 26:581–592

Shirazi R., Shirazi-Adl A., 2005. Analysis of articular cartilage as a composite using nonlinear membrane elements for collagen fibrils. Medical Engineering & Physics 27: 827–835.

Shirazi R., Shirazi-Adl A., 2008. Deep Vertical Collagen Fibrils Play a Significant Role in Mechanics of Articular Cartilage. JOURNAL OF ORTHOPAEDIC RESEARCH 23: 608-615.

Silyn-Roberts H, Broom ND., 1990. Fracture behaviour of cartilage-on-bone in response to repeated impact loading. Connect Tiss Res 24:143–56.

Simon, B.R., 1992. Multiphasic poroelastic finite element models for soft tissue structures. Applied Mechanics Reviews 45: 191-218.

Soltz, M.A., Ateshian, G.A., 1998. Experimental verification and theoretical prediction of cartilage interstitial fluid pressurization at an impermeable contact interface in confined compression. J. Biomech. 31: 927–934.

Soltz, M.A., Ateshian, G.A., 2000a. Interstitial fluid pressurization during confined compression cyclical loading of articular cartilage. Ann. Biomed. Eng. 28: 150–159.

Soltz, M.A., Ateshian, G.A., 2000b. A conewise linear elasticity mixture model for the analysis of tension–compression nonlinearity in articular cartilage. J. Biomech. Eng. 122, 576–586.

Soltz, M.A., Basalo, I.M., Ateshian, G.A., 2003. Hydrostatic pressurization and depletion of trapped lubricant pool during creep contact of a rippled indenter against a biphasic articular cartilage layer. J. Biomech. Eng. 125: 585–593.

Soulhat J, Buschmann MD, Shirazi-Adl A. 1999. A fibril-network reinforced biphasic model of cartilage in unconfined compression. J. Biomech Eng. 121(3): 340–347.

Spilker, R.L., Suh, J.K., 1990. Formulation and evaluation of a finite element model for the biphasic model of hydrated soft tissues. Comput. Struct. 35: 425–439.

Spilker, R.L., Suh, J.K. and Mow, V.C., 1992. A finite-element analysis of the indentation stress-relaxation response of linear biphasic articular-cartilage. Journal of Biomechanical Engineering-Transactions of the ASME, 114(2): p. 191-201.

Stewart,T.D. , Hall, R.M. , 2006. Basic biomechanics of human joints: Hips, knees and the spine. Current Orthopaedics, 20(1) 23-31.

Stockwell RA., 1979. Biology of cartilage cells. Cambridge: Cambridge University Press.

Suh, J. K., Spilker, R.L., Holmes, M.H., 1991. A penalty finite element analysis for nonlinear mechanics of biphasic hydrated soft tissue under large deformation. Int. J. Numer. Methods Eng. 32: 1411–1439.

Suh, J. K., DiSilvestro, M. R., 1997, ‘‘Biphasic Poroviscoelastic Theory of Articular Cartilage: Experimental Validation Through Unconfined Compression,’’ Proc. ASME Summer Bioengineering Conference, Vol. 35: 31–32.

Suh, J. K., Bai, S., 1997, ‘‘Biphasic Poroviscoelastic Behavior of Articular Cartilage in Creep Indentation Test,’’ Proc. 43rd Annual Meeting of the Orthopaedic Research Society, Vol. 22: 823.

Suh J.K., Bai S., 1998. Finite element formulation of biphasic poroviscoelastic model for articular cartilage. J Biomech Eng 120(2): 195–201.

Swann, D.A., Radin, E.L., 1972. The molecular basis of articular lubrication. I. Purification and properties of a lubricating fraction from bovine synovial fluid. J. Biol. Chem. 247, 8069–8073.

Taylor Z. A. and Miller K., 2006. Constitutive modeling of cartilaginous tissues: a review. Journal of Biomechanics, vol. 22, no. 3, pp. 212–229.

Thomas M.Q., Ernst B.H. and Hans-Jorg H., 2005. Variation of cell and matrix morphologies in articular cartilage among locations in the adult human knee. OsteoArthritis and Cartilage 13, 672-678.

Urban JPG, Maroudas A, Bayliss MT, Dillon J., 1979. Swelling pressures of PG’s at the concentrations found in cartilagenous tissues. Biorheology 16:447–464.

Visser S.K., Crawford R.W., Pope J.M., 2008. Structural adaptations in compressed articular cartilage measured by diffusion tensor imaging. Osteoarthritis Cartilage. 16, 83-89.

Visser SK, Bowden JC, Wentrup-Bryne E, Rintoul L, Bostrom T, Pope JM, Momot KI. Anisotropy of collagen fibre alignment in bovine cartilage: comparison of polarised light microscopy and spatially resolved diffusion-tensor measurements. Osteoarthritis Cartilage 2008 (b); 16:689-697.

Viidik, A., 1968. A Rheological Model for Uncalcified Parallel-Fibered Collagenous Tissues. J. Biomech., 1: 3–11.

Walker, P.S., Dowson, D., Longfield, M.D., Wright, V., 1968. ‘‘Boosted lubrication’’ in synovial joints by fluid entrapment and enrichment. Ann. Rheum. Dis. 27: 512–520.

Wang CC, Hung CT, Mow VC., 2001. An analysis of the effects of depth-dependent aggregate modulus on articular cartilage stress-relaxation behavior in compression. J Biomech 34(1):75–84.

Warner, M.D. Finite element biphasic modelling of articular cartilage: an investigation into crystal induced damage. Ph D Thesis. 2000, University of Bath. 177.

Warner, M.D., Taylor, W.R., et al., 2001a. Finite element biphasic indentation of cartilage: A comparison of experimental indenter and physiological contact geometries. Proceedings of the Institution of Mechanical Engineers Part H-J Eng. Med. 215 (H5), 48-496.

Warner, M.D., Taylor,W.R., et al., 2001b. A method for determining contact between a non-porous surface and articular cartilage in a biphasic FE model. In: Middleton, J., Jones, M.L., Pande, G. (Eds.), Computer Methods in Biomechanics and Bioengineering - 3. Gordon and Breach Science Publishers, pp. 207.212.

Wayne, J.S., Woo, S.L., Kwan, M.K., 1991. Application of the u-p finite element method to the study of articular cartilage. J. Biomech. Eng. 113: 397–403.

Wilson W., van Donkelaar CC., van Rietbergen C., Ito K., Huiskes R.,2004. Stresses in the local collagen network of articular cartilage: a poroviscoelastic fibril-reinforced finite element study. J. Biomech. 37(3): 357–366.

Wilson W., van Donkelaar CC., van Rietbergen R., Huiskes R., 2005a. A fibril-reinforced poroviscoelastic swelling model for articular cartilage. J Biomech. 38, Issue 6: 1195-1204.

Wilson W., van Donkelaar CC., van Rietbergen R., Huiskes R., 2005b. The role of computational models in the search for the mechanical behavior and damage mechanisms of articular cartilage. Medical Engineering & Physics, 27: 810-826.

Wilson W, Huyghe JM, van Donkelaar CC, 2006. A composition-based cartilage model for the assessment of compositional changes during cartilage damage and adaptation. Osteoarthritis Cartilage 14: 554–560.

Wilson W, Huyghe JM, van Donkelaar CC, 2007. Depth-dependent compressive equilibrium properties of articular cartilage. Biomech Model Mechanobiol 6: 43–53.

Wong M, Wuethrich P, Eggli P, Hunziker EB., 1996, Zone-specific cell biosynthesis activity in mature bovine articular cartilage: a new method using confocal microscopic stereology and quantitative autoradiography. J Orthop Res 14: 424–432.

Wong M, Wuethrich P, Buschmann MD, Eggli P, Hunziker EB., 1997. Chondrocyte biosynthesis correlates with local tissue strain in statically compressed adult articular cartilage. J Orthop Res 15:189–96.

Wu, J. Z., Herzog, W., Epstein, M., 1998. Evaluation of the finite element software ABAQUS for biomechanical modelling of biphasic tissues. J. Biomech. 31: 165–169.

Appendix A List of Publications

Conference Abstract:

1) An, Shuqiang; Jones Alison; Damion Robin; Fisher John and Jin Zhongmin. Realistic Fibril Distribution Basing on DT-MRI Data Enhances Pressurization of Interstitial Fluid in 2D Fibril-Reinforced Cartilage Model. Podium presentation. Paper No. 0396, Session 66. Annual Meeting of the Orthopaedic Research Society, 2013, San Antonio, Texas.

Appendix B Derivation of the Contribution of Fibillar Matrix

According to Section 3.2.2, the fibrillar stress in the iterative step (*t* + ***Δt***) was calculated as:

$$\sigma_x^{\mathrm{f}}(t+\Delta t) = \sigma_x^{\mathrm{f}}(0) + \int_0^{t+\Delta t} G_x(t+\Delta t-\tau) E_x^{\mathrm{f}}(\varepsilon_x)\dot{\varepsilon}_x \, d\tau \qquad (\mathrm{B.1})$$

Splitting the integration followed by a series of equivalent conversion, formula (B.1) was rewritten as:

$$\sigma_x^{\mathrm{f}}(t+\Delta t) = \sigma_x^{\mathrm{f}}(0) + \int_0^t G_x(t+\Delta t-\tau)E_x^{\mathrm{f}}(\varepsilon_x)\dot{\varepsilon}_x\, d\tau$$

$$+ \int_t^{t+\Delta t} G_x(t+\Delta t-\tau)E_x^{\mathrm{f}}(\varepsilon_x)\dot{\varepsilon}_x\, d\tau$$

$$= [\sigma_x^{\mathrm{f}}(0) + \int_0^t G_x(t-\tau)\, E_x^{\mathrm{f}}(\varepsilon_x)\dot{\varepsilon}_x\, d\tau]$$

$$- \int_0^t G_x(t-\tau)\, E_x^{\mathrm{f}}(\varepsilon_x)\dot{\varepsilon}_x\, d\tau + \int_0^t G_x(t+\Delta t-\tau)E_x^{\mathrm{f}}(\varepsilon_x)\dot{\varepsilon}_x\, d\tau$$

$$+ \int_t^{t+\Delta t} G_x(t+\Delta t-\tau)E_x^{\mathrm{f}}(\varepsilon_x)\dot{\varepsilon}_x\, d\tau$$

$$= \sigma_x^{\mathrm{f}}(t) + \int_0^t [G_x(t+\Delta t-\tau) - G_x(t-\tau)]\, E_x^{\mathrm{f}}(\varepsilon_x)\dot{\varepsilon}_x\, d\tau$$

$$+ \int_t^{t+\Delta t} G_x(t+\Delta t-\tau)E_x^{\mathrm{f}}(\varepsilon_x)\dot{\varepsilon}_x\, d\tau$$

$$\approx \sigma_x^{\mathrm{f}}(t) + \int_0^t [G_x(t+\Delta t-\tau) - G_x(t-\tau)]\, E_x^{\mathrm{f}}(\varepsilon_x)\dot{\varepsilon}_x\, d\tau$$

$$+ G_x(\Delta t)E_x^{\mathrm{f}}(\varepsilon_x)\dot{\varepsilon}_x\, \Delta t \qquad (\mathrm{B}.2)$$

where $G_x(\Delta t)E_x^{\mathrm{f}}(\varepsilon_x)\dot{\varepsilon}_x\, \Delta t$ is the approximation of the last item in the step forward i.e. $\int_t^{t+\Delta t} G_x(t+\Delta t-\tau)E_x^{\mathrm{f}}(\varepsilon_x)\dot{\varepsilon}_x\, d\tau$.

In equation (B.2), $\dot{\varepsilon}_x\, \Delta t$ could be replaced by $\Delta\varepsilon$ according to the definition of $\dot{\varepsilon}_x$. So,

$$\begin{aligned}\Delta\sigma_x^{\mathrm{f}} &= \sigma_x^{\mathrm{f}}(t+\mathit{\Delta}t) - \sigma_x^{\mathrm{f}}(t) \\ &\approx G_x(\mathit{\Delta}t)E_x^{\mathrm{f}}(\varepsilon_x)\,\mathit{\Delta}\varepsilon \\ &\quad + \int_0^t [G_x(t+\mathit{\Delta}t-\tau) - G_x(t-\tau)]\,E_x^{\mathrm{f}}(\varepsilon_x)\dot{\varepsilon}_x\,d\tau\end{aligned}$$

Meanwhile, the integration

$$\int_0^t [G_x(t+\mathit{\Delta}t-\tau) - G_x(t-\tau)]\,E_x^{\mathrm{f}}(\varepsilon_x)\dot{\varepsilon}_x\,d\tau$$

was determined in the previous iterative step (Li et al., 2009) i.e. was treated as a constant in the current iterative step. Hence, the contribution of the fibrillar matrix to the Jacobian was derived as:

$$\partial\Delta\sigma_x^{\mathrm{f}}/\partial\Delta\varepsilon_x^{\mathrm{f}} \approx G_x(\mathit{\Delta}t)E_x^{\mathrm{f}}(\varepsilon_x)$$